GFZ

Helmholtz-Zentrum

POTSDAM

S. Fischer

Mineralogical-geochemical effects during geological storage of CO$_2$ – Experimental investigations and geochemical modeling

Scientific Technical Report STR13/13

HELMHOLTZ
| GEMEINSCHAFT

Mineralogical-geochemical effects during geological storage of CO₂ – Experimental investigations and geochemical modeling

vorgelegt von
Diplom-Geologe
Sebastian Fischer
aus Berlin

von der Fakultät VI – Planen Bauen Umwelt
der Technischen Universität Berlin
zur Erlangung des akademischen Grades

Doktor der Naturwissenschaften
– Dr. rer. nat. –

genehmigte Dissertation

Promotionsausschuss:

Vorsitzender: Prof. Horsfield
Gutachter: Prof. Franz
Gutachter: Prof. Gaupp (Universität Jena)
Gutachter: Dr. habil. Liebscher (GFZ Potsdam)

Tag der wissenschaftlichen Aussprache: 24. Oktober 2013

Berlin 2013

D 83

Abstract

In order to analyze mineralogical-geochemical changes occurring in whole rock reservoir samples (Stuttgart Formation) from the Ketzin pilot CO_2 storage site, Brandenburg/Germany as well as to investigate single fluid-mineral reactions laboratory experiments and geochemical modeling were performed. The whole rock core samples of the Stuttgart Formation were exposed to synthetic brine and pure CO_2 at experimental P-T conditions and run durations of 5.5 MPa/40 °C/40 months for sandstone and 7.5 MPa/40 °C/6 months for siltstone, respectively. Mineralogical changes in both sets of experiments are generally minor making it difficult to differentiate the natural variability of the whole rock samples from CO_2-induced alterations. Results of sandstone experiments suggest dissolution of analcime, anhydrite, the anorthite component of plagioclase, chlorite + biotite, hematite and K-feldspar. Dissolution of anhydrite, the anorthite component of plagioclase and K-feldspar is also observed in siltstone experiments.

During equilibrium simulations best matching models were ranked based on a mathematical-statistical dispersion relation. The best matching model comprises a mineral combination of the albite component of plagioclase, anhydrite, dolomite, hematite, and illite. The equilibrium modeling showed that it is difficult to match K^+, Fe^{2+} and SO_4^{2-} brine concentrations simultaneously. The best matching subsets of the equilibrium models were finally run including kinetic rate laws. These kinetic simulations reveal that experimentally determined brine data was well matched, but reactions involving K^+ and Fe^{2+} were not completely covered. Generally larger mismatches for dissolved Al^{3+} and Si^{4+} in all the completed simulations are most likely related to the sampling strategy and respective inaccuracies in the measured concentrations of dissolved Al^{3+} and Si^{4+}. The kinetic simulation suppressing mineral precipitation yields best matches with experimental observations. The modeling shows acceptably well matches with measured brine ion concentrations, and the modeling results identified primary minerals as well as key chemical processes. It was also shown that the modeling approach is not capable of completely covering complex natural systems.

Experiments on mineral separates were conducted with 2 M NaCl brine and pure CO_2 using siderite, illite and labradorite samples. Experimental P-T conditions were 20 (30) MPa and 80 °C; run durations were one (siderite), two (illite) and three weeks (labradorite), respectively. Based on the acquired set of mineralogical-geochemical data the distinct experiments show: (i) dissolution of ankerite and stable siderite, which is therefore interpreted to be a potential CO_2 trapping phase, (ii) preferred dissolution of the Ca-smectite component out of the illite-smectite mixed-layer mineral and (iii) dissolution of labradorite, respectively.

No mineral precipitates (e.g. carbonate phases) were detected in any of the conducted laboratory experiments, and only one single kinetic simulation predicts the formation of minute amounts of dolomite.

Based on the data acquired during this dissertation the mineralogical-geochemical effects of CO_2 are minor, and the (chemical) integrity of the Ketzin reservoir system is not significantly affected by injected CO_2.

Eidesstattliche Erklärung

Hiermit erkläre ich, Sebastian Fischer, geboren am 02. August 1980 in Berlin, die vorgelegte Dissertation mit dem Titel „Mineralogical-geochemical effects during geological storage of CO_2 – Experimental investigations and geochemical modeling" eigenständig verfasst und angefertigt zu haben. Alle Zitate sind entsprechend gekennzeichnet und die verwendeten Quellen sind im Quellenverzeichnis aufgelistet. Die Arbeit ist weder ganz noch zum Teil einer anderen Stelle im Rahmen eines Prüfungsverfahrens vorgelegt worden und unter Einhaltung der Regeln guter wissenschaftlicher Praxis entstanden.

Potsdam, 28.11.11

Ort, Datum, Sebastian Fischer

Table of Contents

1. INTRODUCTION

Global warming and climate change are regarded to be directly linked to increasing concentrations of atmospheric CO_2. An increasing global population demands more primary energy supplied at cheap costs and reliable performance. Hydrocarbon commodities, especially lignite and hard coal, fulfill these requirements and respective reserves will last for many more decades to come. Coal-fired power plants are the major source of CO_2 emissions. By capturing CO_2 from these large point sources and storing it underground the process chain of carbon dioxide capture and storage (CCS) prevents CO_2 emission to reach the atmosphere and is thus expected to play a pivotal role in mitigating climate change.

The geological storage of CO_2 into saline aquifers is the subject of this cumulative dissertation with the main focus being on the experimental study of geochemical reactions between injected CO_2, formation brine and reservoir rock, on the one hand, and the analysis and quantification of single CO_2-brine-mineral reactions, on the other. Once CO_2 is injected into subsurface reservoirs, multiple, partially physical, but mainly chemical trapping mechanisms prevent CO_2 from reaching the surface again. Detailed knowledge of the location, the time and the processes controlling CO_2-related geochemical reactions is important not only to better understand the behavior of injected CO_2 within the storage system, but also in terms of assessing storage viability and long-term safety.

In this work, laboratory experiments and numerical geochemical modeling were performed and combined in order to analyze (i) CO_2-brine-rock interactions, (ii) single fluid-mineral reactions, and (iii) the effects of injected CO_2 on the chemical integrity of the reservoir system. For laboratory experiments, original rock core material from the Ketzin pilot CO_2 storage site in Brandenburg (Germany) as well as individual powder separates of rock-forming minerals were used. Geochemical modeling was done complementary to the experiments on reservoir rock samples in order to reproduce the experimentally determined brine data with numerical simulations and to identify key chemical processes and most reactive minerals.

Following a general introduction, subsequent chapters are based on individual publications. The first two chapters (Chapters 2 and 3) report results of long-term CO_2-exposure experiments on reservoir rock samples. In Chapter 4 data of a first modeling approach, in which the measured brine data of the sandstone experiments is tried to be reproduced, is discussed. The complete data set of the long-term experiments on reservoir rocks including a more comprehensive geochemical modeling approach as well as results from experiments on cap-rock-like siltstone samples are conclusively discussed in Chapter 5. Results of experiments using mineral powder separates are presented in Chapters 6 and 7. The closing synopsis (Chapter 8) specifies the major results as determined from the experiments and modeling, and discusses their impact in terms of relevance and scientific benefit in order to finally conclude the dissertation and give an outlook.

1.1 General background

1.1.1 *Primary energy production and fossil fuels consumption*

Modern society and wealth function on the basis of fossil energy resources (e.g. IEA, 2012a). Hydrocarbons, such as lignite, hard coal, crude oil and natural gas are carbon-based fuels that provide approximately 80% of today's primary energy in Germany (AGEB, 2011) and worldwide (Fig. 1A; IEA, 2012b). Global population is expected to grow and reach nine billion people by 2050 (United Nations, 2011) and because more people consume more energy (Kaya, 1995), the global energy demand is anticipated to grow by more than one-third until 2035 (IEA, 2012a; Fig. 1C).
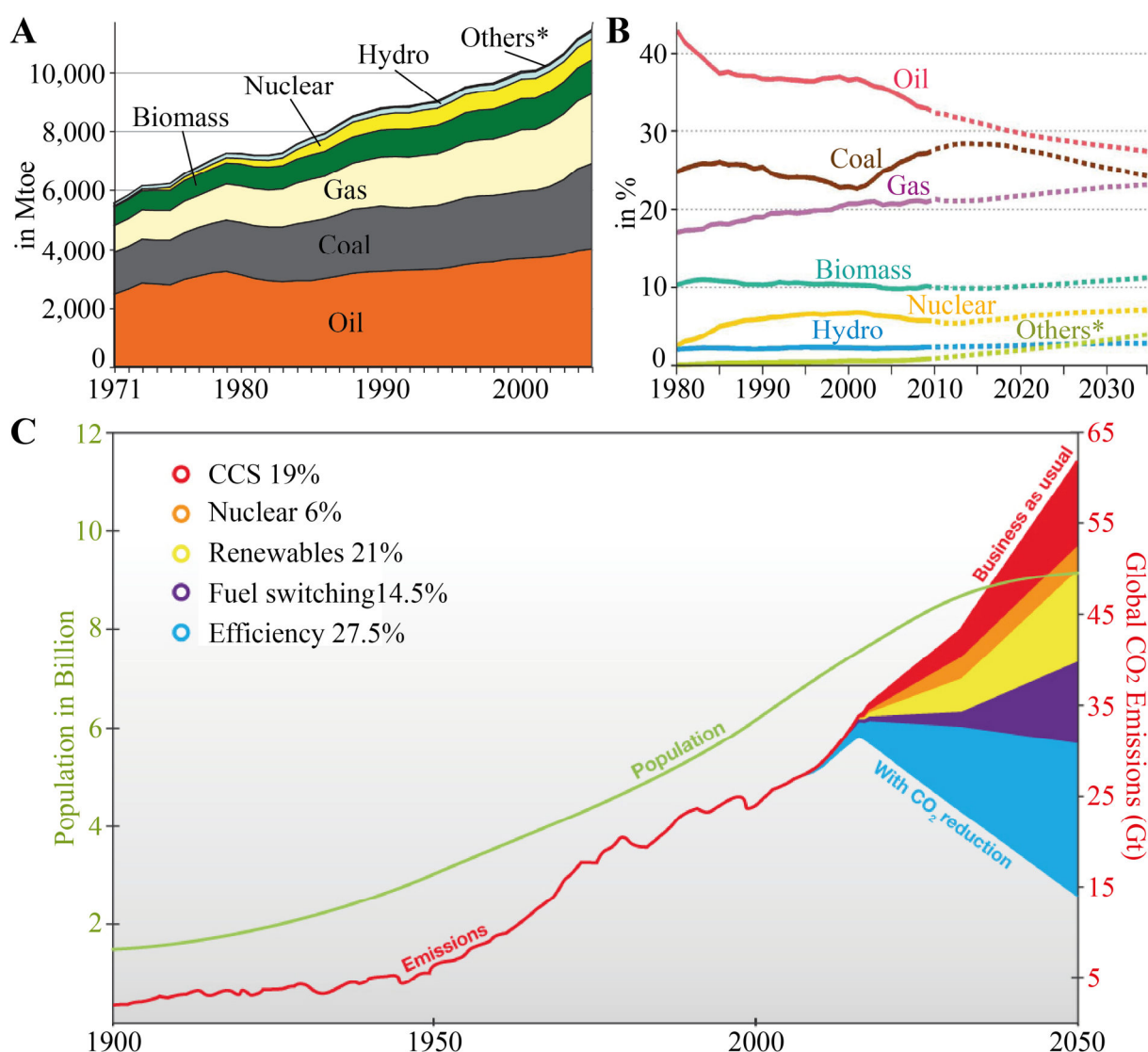

Fig. 1 – A: Global energy consumption by fuel type (modified after IPCC, 2007); B: Shares and projections of global primary energy sources (modified after IEA, 2011); C: Record and trends for global population and global CO_2 emissions (modified after CO_2CRC). * = Others include geothermal, solar, wind, heat, etc.; Mtoe = Million ton of oil equivalent.

By far the largest single source of CO_2 emissions derives from the oxidation of carbon during fossil fuels combustion in power stations, refineries and industrial facilities (IPCC, 2005). In 2010, almost half (43%) of the global CO_2 emissions were produced from coal-fired power plants (IEA, 2012c), and it is very likely that these power stations will still generate about half of the global energy demand and respective CO_2 emissions in 2050 (IPCC, 2005).

1.1.2 *Carbon dioxide, global warming and climate change*

Besides water vapor, CO_2 is the most prominent and quantitatively the largest greenhouse gas (Kiehl and Trenberth, 1997). Greenhouse gases absorb and re-radiate thermal infrared radiation emitted from the Earth's surface back downward to the Earth. Heat is thus held within the surface-troposphere system to cause the greenhouse effect (IPCC, 2007). The natural greenhouse effect is enhanced through increased atmospheric concentrations of CO_2, which amplify radiative forcing by approximately 60% (IPCC, 2001b). Compared with pre-industrialized levels of 280 ppmv in the 18th century, today's atmospheric CO_2 concentrations of about 380 ppmv are significantly enriched with the most prominent contributor to the so-called anthropogenic greenhouse effect being the conventional use of fossil fuels (Karl and Trenberth, 2003). Assuming that fossil fuels will play the major role in supplying energy to future societies, forecasts for a business as usual scenario predict continuing increases in atmospheric CO_2 concentrations to values above 450 ppmv within the next decades (IPCC, 2007).

1.1.3 *Strategies to reduce CO_2 emissions*

Climate disruptions such as desertification, sea level rise, modification of precipitation patterns and more frequent weather-related disasters affect millions of people around the world. Consequently, society and economy have to react to it and find adaptation strategies to reduce natural and human system vulnerability, and therefore CO_2 emissions have to be drastically reduced. It is inevitable that fossil-fueled power stations get cleaner, energy efficiencies are improved and sustainable alternatives are developed enabling the switch to less carbon-intensive and non-fossil fuel based power generation. The use of renewable energy resources, which, e.g., account for about 11% of the total primary energy production of Germany in 2011 (AGEB, 2011) and is generally expected to grow strongly within the near future, will at best account for about one-third of the total global energy production by 2035 (IEA, 2012a). At present, nuclear energy is not considered as an option in many countries anymore after the 2011 Fukushima Daiichi accident. Due to their plentiful continued availability, affordable low cost of supply and ease of use, fossil fuels are still considered an important factor enabling economic growth. Lignite as well as hard coal, e.g., will both be sufficiently available for more than a century (BGR, 2009). For the way to clean(er) energy production, technologies bridging the gap from today until the existing energy infrastructure is replaced with non-fossil fuel based power generation in the future are at hand already. One of those technologies is carbon dioxide capture and storage (CCS).

### 1.1.4 *Carbon dioxide capture and storage (CCS)*

Within the manifold portfolio of measures designed to counteract increasing atmospheric temperatures and climate change, carbon dioxide capture and storage (CCS) is regarded a prominent candidate to mitigate CO_2 emissions to the atmosphere with large reduction potentials (e.g. Gunter et al., 1993; Bachu et al., 1994; Holloway, 1997). The CCS technology is a process chain that involves separation and capture of CO_2 from large point sources, its transport to suitable storage sites and subsequent secure and permanent storage away from the atmosphere (IPCC, 2005). In this work, capture and transport are not further discussed and the focus is on the geological storage of CO_2.

A variety of geological settings (e.g. depleted oil/gas formations, deep saline aquifers, unmineable coal seams, basalts) and other options (e.g. ocean storage, mineral carbonation) potentially viable for storing CO_2 exist. Because most parts in this manuscript are directly related to the Ketzin pilot CO_2 storage site at which CO_2 is injected into a saline aquifer, the main focus in the following will be on CO_2 storage in saline aquifers. Out of the potential geological storage options saline aquifers are most prolific in terms of capacity and widespread distribution (Gunter et al., 1993). Saline aquifers are porous and permeable rock formations that are saturated with high-salinity waters (i.e. brines), bound by seals (i.e. cap rocks), occur in siliciclastic (sandstone) or carbonate formations and hold large brine quantities that are unsuitable for agricultural use or human consumption. In this study, the focus is on saline aquifers occurring in sandstone formations, because the target reservoir at the Ketzin pilot CO_2 storage site is the siliciclastic Stuttgart Formation. In general, siliciclastic reservoirs are preferable over carbonate reservoirs due to having higher potentials of pH buffering, CO_2 solubility and net carbonate precipitation (Gunter et al., 1997; Rochelle et al., 2004).

Injected CO_2 has a lower density compared to that of brines under ambient reservoir conditions (Angus et al., 1973) whereby buoyancy forces tendentially drive CO_2 upward. Various physical and chemical trapping mechanisms gradually immobilize and retain CO_2 from reaching the surface again for millennial timescales.

Initially most relevant trapping mechanisms are associated with stratigraphic and structural features (Fig. 2). **Stratigraphic trapping** occurs when well-sealed, low permeability cap rock formations overlaying the storage reservoir impede the upward migration of CO_2. Cap rocks are mainly clayey, shaly or salty lithologies. Cap rock formations that are tectonically folded, e.g., through stress-strain regimes or gravity (in the case of salt tectonics), may form **structural traps** such as dome-like anticlines. Key aspects determining hydraulic-mechanical seal integrity are CO_2-brine-rock reactions – which is thematized in the cap-rock-like siltstone experiments of Chapter 4 – as well as physical rock strength. **Solubility trapping** is a chemical mechanism, which refers to the fraction of CO_2 that dissolves into formation brine. The solubility of CO_2 in brine is primarily a function of brine salinity, ambient pressure and temperature (Parry et al., 2007), but also depends on flow regime and the available contact area between CO_2 and unsaturated formation brine (Lindeberg and Wessel-Berg, 1997; Rochelle et al., 2004). The process of **hydrodynamic trapping** may occur in open systems in case CO_2-charged fluids slowly migrate with the local groundwater flow regime over long distances (Bachu et al., 1994).
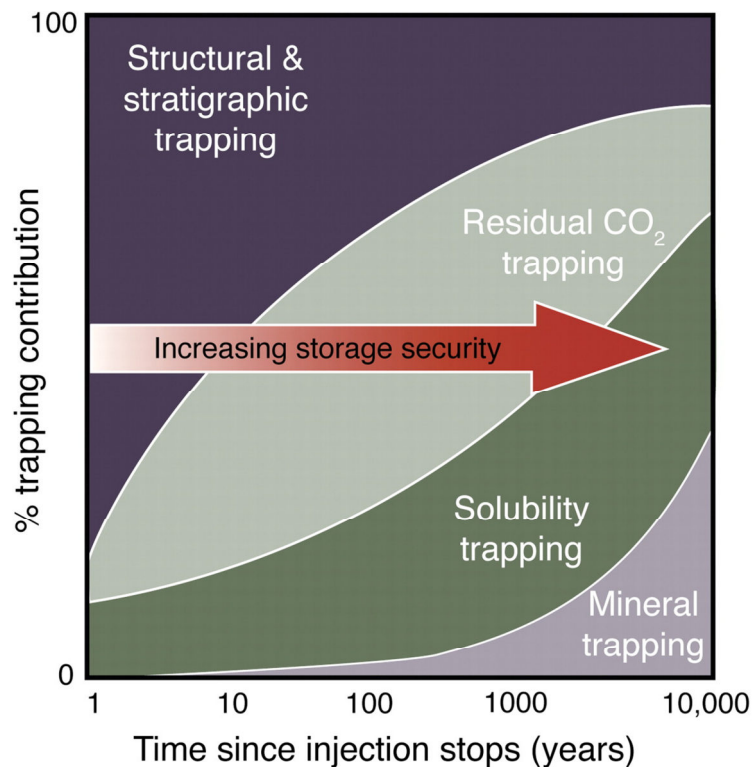
Fig. 2 – Generalized illustration of the percental contribution of the most prominent physical and chemical trapping mechanisms in relation to storage security over time (IPCC, 2005).

Capillary forces retain CO_2 in the pore spaces to provide **residual CO_2 trapping** (Obdam et al., 2003; Kumar et al., 2005). When CO_2-brine-rock interactions form immobile solid carbonate minerals that are stable for geological time periods (Gunter et al., 1993), **mineral trapping** is achieved. The formation of carbonate phases was generally analyzed during the described laboratory and modeling experiments, respectively, but is especially thematized in Chapter 5. Despite the fact that the process of mineral trapping is kinetically slow potentially taking hundreds to thousands of years (e.g. Bachu et al., 1994), it is the most permanent form of storing CO_2 underground. As apparent in Figure 3 the contribution of the different trapping mechanisms will change with time. While structural and stratigraphic trapping are of major importance initially, respective processes are successively eclipsed by residual and solubility trapping. The contribution of carbonate formation and mineral trapping becomes progressively more important after several hundred years so that storage security will hence increase with time.

1.1.5 *The importance of mineralogical-geochemical reactions during geological CO_2 storage*

By injecting CO_2 into the deeper subsurface the reservoir is brought out of (a reasonably conceivable) thermodynamic-chemical equilibrium. Subsequently, the storage system tends to re-equilibrate and various complexly coupled geochemical reactions are triggered. Initially, the addition of CO_2 to brine leads to an increased amount of dissolved CO_2, which then reacts with water molecules to form

carbonic acid (reaction sequence [1]). Due to the dissociation of carbonic acid, bicarbonate ions are formed, and further dissociation of bicarbonate ions ultimately leads to the formation of carbonate ions. This reaction sequence can be written as follows:

$$CO_{2(g)} \leftrightarrow CO_{2(aq)} + H_2O_{(aq)} \leftrightarrow H_2CO_{3(aq)} \leftrightarrow HCO_3^-{}_{(aq)} + H^+{}_{(aq)} \leftrightarrow CO_3^{2-}{}_{(aq)} + 2H^+{}_{(aq)} \quad [1]$$
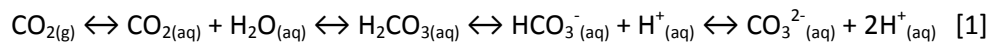
Brine pH is lowered through the genesis of $H^+{}_{(aq)}$ ions during the latter two reaction steps. The very last reaction step is restricted to alkaline environments. pH can be buffered through acid attack reactions of CO_2 with reservoir and cap rocks. It strongly depends on the mineralogical composition of the respective rock, which and to what extend these reactions occur. In case aluminosilicate minerals, such as feldspars, are present, divalent metal cations like Ca^{2+}, Mg^{2+}, Fe^{2+} and Mn^{2+} can, amongst others, be released from the rock. Reaction [2] of dissolving anorthite and subsequent formation of kaolinite is exemplary for CO_2-induced (i.e. H^+-generated) feldspar alteration:

$$CaAl_2Si_2O_8 + 2H^+{}_{(aq)} + H_2O_{(aq)} \leftrightarrow Ca^{2+}{}_{(aq)} + Al_2Si_2O_5(OH)_4 \quad [2]$$
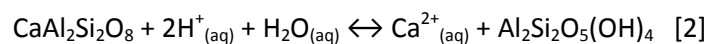
The more such pH-buffering reactions occur, the more the reaction sequence [1] inclines to the right and the more CO_2 can dissolve into the brine (Rochelle et al., 2004). The maximum concentration of dissolved CO_2 thus determines the reactivity of the reservoir system (Gaus, 2010). But due to the relatively slow kinetics of CO_2-brine-aluminosilicate reactions under ambient deep-aquifer P-T conditions (Palandri and Kharaka, 2004) re-equilibration of the reservoir takes some time. When free $Ca^{2+}{}_{(aq)}$ and $HCO_3^-{}_{(aq)}$ are present CO_2 may be immobilized through calcite precipitation:

$$Ca^{2+}{}_{(aq)} + HCO_3^-{}_{(aq)} \leftrightarrow CaCO_3 + H^+{}_{(aq)} \quad [3]$$
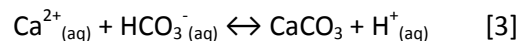
Reaction [3] forms the theoretical basis of CO_2 sequestration, but is notably most effective in alkaline environments (i.e. at high pH values; see above). As a summary of reactions [1] to [3] reaction [4] can be formulated as follows:

$$CaAl_2Si_2O_8 + 2H_2O_{(aq)} + CO_{2(aq)} \leftrightarrow CaCO_3 + Al_2Si_2O_5(OH)_4 \quad [4]$$
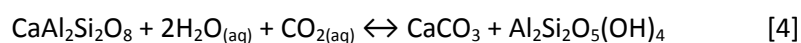
The nature, the timing, the location, the magnitude and the processes controlling respective reactions with reservoir and cap rocks can have substantial beneficial or deleterious consequences. Of primary concern is their impact on the petrophysical properties porosity and permeability. These are closely linked with injectivity, storage capacity, sealing efficiency, long-term integrity, CO_2 movement, containment, and monitoring of the reservoir system (Rochelle et al., 2004). For example, it is well known that, by clogging pore throats and/or filling open cleavages, precipitation of microscopic amounts of secondary minerals may cause a substantial reduction in permeability (Gaus, 2010), which could furthermore cause an increase in reservoir pressure due to reduced injectivity. Consequently, a better understanding of the behavior and the ability to predict the long-term fate of CO_2 within a subsurface reservoir system is of major importance and one of the key issues for safe and permanent CO_2 storage.

1.2 How can CO_2-brine-rock reactions be investigated?

Detailed mineralogical-geochemical knowledge of the behavior of CO_2 in subsurface formations can be gained from observations of natural CO_2 analogues (e.g. Pearce et al., 1996; Watson et al., 2004; Gilfillan et al., 2009), and through performing field scale tests (e.g. Assayag et al., 2009; Kharaka et al., 2010; Fagerlund et al., 2013), laboratory (e.g. Gunther et al., 1997; Kaszuba et al., 2005; Wigand et al., 2008) as well as numerical modeling experiments (e.g. Czernichowski-Lauriol et al., 1996; Gaus et al., 2005; De Lucia et al., 2012) on reservoir and cap rocks. Despite intensive research on CO_2-related brine-rock interactions during the last years, identified mineral reactions in natural analogue systems and laboratory experiments, and those predicted by geochemical modeling generally match fairly well (Rochelle et al., 2004), but discrepancies concerning direction, rate and magnitude of these reactions still exist.

Observations from **natural CO_2 analogues** provide information on CO_2-brine-rock interactions that occur during geologic timescales. But these observations are difficult to interpret uniquely and are of rather qualitative nature as they result from a complex suite of reaction paths and changing boundary conditions that often cannot be completely reconstructed (Gaus, 2010). Also **field scale tests** are useful to study in-situ CO_2-brine-rock reactions based on changes in fluid chemistry, isotopic and gas compositions in the timescale of days to weeks. To overcome the problem of the often only available gas and fluid samples and hence indirect data for CO_2-brine-rock reactions, **laboratory experiments** using solid sample materials are realistic approaches that mimic natural environments. These offer the possibility to directly determine the correlation between observed mineral/rock alteration, solution chemistry, gas composition and petrophysical parameters. Limits are set through the dimension/magnitude and the timescale of often only months to years at the longest. Due to the large lithological and physicochemical variability of (potential) storage systems as determined by and depending on the prevailing P-T conditions, site-specific rock as well as brine compositions (e.g. Czernichowski-Lauriol et al., 2006), the compilation of detailed reaction patterns that would be generally valid for a wide range of storage environments is hampered. Consequently, CO_2-exposure experiments have to be performed for each individual storage system and original rock material has to be investigated. For the Ketzin CO_2 storage site respective laboratory experiments using rock core samples of the Stuttgart Formation, synthetic reservoir brines, in situ P-T conditions and pure CO_2 are described in Chapters 2, 3 and 5.

Owing to the general scarce availability of natural rock samples from (potential) subsurface reservoirs experimentalists often use powdered separates of rock-forming minerals as rock equivalents. Monomineralic separates can be used to characterize single fluid-mineral reactions and to determine kinetic reaction rates. Respective laboratory experiments on mineral separates of siderite, illite and labradorite, that were reacted in (comparatively simple) CO_2-H_2O-NaCl systems at relevant storage P-T conditions, are described in Chapters 6 and 7.

In order to approximately represent complex natural rock compositions different mineral powders may be mixed. On the downside, respective mineral powders have larger reactive surface areas and are unconsolidated with deviating mineral surface accessibilities compared to natural rocks.

Reaction rates, especially for aluminosilicates, are slow under ambient reservoir temperatures (and pressures) and are therefore difficult to determine in laboratory experiments. Laboratory

experiments exceeding six months are generally scarce in the scientific literature. To overcome the problem of slow reaction kinetics, experiments have to either be performed at elevated temperatures (and pressures), in the presence of a flow regime, by using larger reactive surface areas, and/or considerably prolonged run durations; or by the use of other indirect techniques.

Numerical geochemical models are based on experimentally acquired thermodynamic parameters that are compiled in respective databases and can be used to fully assess complex chemical reaction paths, to identify key geochemical reactions as well as their potential effects over millennial timescales. For the long-term CO_2-exposure experiments performed on Ketzin reservoir sandstone the ability of geochemical models to reproduce experimentally observed data by matching measured brine concentrations was tested. This work is described in Chapters 4 and 5.

Modeling approaches are subject to uncertainties at various levels. These uncertainties arise from the complex mineralogy of reservoir and cap rocks, on the one hand, and inbuilt numerical simplifications, on the other. Reservoir and cap rocks often comprise up to ten or more individual and solid solution mineral phases, which cannot be introduced into numerical models as such, so that only most reactive minerals, and those for which kinetic rate parameters exist, can be implemented. Also the occurrence or absence of mineral coatings, which strongly affect mineral reactivities, are difficult to determine and hardly possible to implement into model simulations. Further numerical simplifications and associated assumptions include the use of indirect data input techniques, the selection of the underlying database, reactive surface area determination, applied kinetic rate laws, ion activity models for high salinity environments and the definition of precipitation surfaces (Czernichowski-Lauriol et al., 2006; Gaus, 2010).

1.3 Chapter outline

As part of this dissertation long-term CO_2-exposure experiments were performed on original rock core samples from the Ketzin pilot CO_2 storage site. The Ketzin site is located about 25 km west of Berlin in the federal state of Brandenburg/Germany and represents Europe's first and longest operating on-shore CO_2 storage facility (Martens et al., 2012; 2013). Laboratory experiments were started directly after drilling was completed in summer 2007. Seven core sections of the target reservoir sector from observation well Ktzi 202 were available for sample extraction. Samples were characterized using mineralogical-geochemical methods and results were compared with those determined from CO_2-treated samples. The experiments were performed at in situ P-T conditions of the Ketzin reservoir in order to assess the effects of CO_2 exposure on reservoir rocks, to better understand the reservoir behavior and to finally be able to better predict the long-term behavior of CO_2 within the Ketzin reservoir. The Ketzin reservoir is situated at approximately 620 m depth and has concomitant low ambient P-T conditions compared to other CO_2 storage sites. Through this unique setting and by using original Ketzin rock core samples, the obtained experimental results provide data and direct observations of site-specific CO_2-brine-rock reactions and add to the existing database.

Chapter 2 "CO_2-brine-rock interaction – First results of long-term exposure experiments at in situ P-T conditions of the Ketzin CO_2 reservoir" presents data of sandstone experiments (Fischer et al., 2010). The focus is on the initial characterization of the reservoir rock and results from the first sampling campaign carried out after 15 months of CO_2 exposure. The data indicate alteration of plagioclase with preferred dissolution of the anorthite component, dissolution of K-feldspar and anhydrite, and stabilization or precipitation of the albite component of plagioclase.

In Chapter 3 "Petrophysical and petrochemical effects of long-term CO_2-exposure experiments on brine-saturated reservoir sandstone", results from additional mineralogical-geochemical and petrophysical data obtained from samples taken after 21 months of CO_2 exposure are reported (Fischer et al., 2011). Despite the fact that no additional evidence of albite precipitation was detected, the mineralogical-geochemical trends described in Chapter 1 are generally confirmed. In addition, the data set suggests intensified dissolution of the anorthite component of plagioclase and slightly increased porosities with a shift to larger pore sizes over time.

Chapter 4 "Kinetic modeling of laboratory CO_2-exposure experiments performed on whole rock reservoir samples" discusses results that were obtained during geochemical modeling (Fischer et al., submitted(A)). This first modeling approach was conducted complementary to the laboratory sandstone experiments. Different kinetic models were set up and run in order to match experimental observations and directly validate theoretical models against measured data, on the one hand, and to evaluate the effect of precipitation for minerals that were supersaturated in equilibrium models, on the other. The best match with experimental brine data was obtained by the model completely suppressing mineral precipitation. Despite the fact that key mineral phases and fundamental chemical processes were identified under respective assumptions and simplifications, distinct models are not capable to completely reproduce the complex geochemical system of the sandstone experiments and not all possible contingencies are covered.

Chapter 5 "Reactivity of sandstone and siltstone samples from the Ketzin pilot CO_2 storage site – Laboratory experiments and reactive geochemical modeling" deals with mineralogical-geochemical results of the terminated sandstone experiments and compares respective observations with results obtained from numerical simulations (Fischer et al., 2013a). Additionally, the paper includes results from cap-rock-like siltstone experiments. Taken together both whole rock experiments reveal that dissolution of the anorthite component of plagioclase, K-feldspar and anhydrite and stabilization of the albite component of plagioclase comprise the main effects during CO_2 exposure. No secondary mineral precipitation was detected. For the second geochemical modeling approach, more structured and more comprehensive models were set up including, e.g., an extensive set of equilibrium models representing all possible combinations of the identified minerals as well as kaolinite precipitation. Equilibrium models show a fairly good match with experimentally measured brine data. Main discrepancies are associated with reactions involving Fe^{2+} and Al^{3+}. Also kinetic models that were set up based on best matching equilibrium models reveal fairly good matches with experimentally determined brine data, on the one hand, but also that reactions involving K^+ and Fe^{2+} are not completely covered.

In the last two chapters results from experiments on powdered mineral separates are presented. By using mineral separates together with 2 M NaCl brine and pure CO_2 comparatively simple chemical systems were considered in order to be able to investigate single fluid-mineral reactions.

In Chapter 6 "Does injected CO_2 affect (chemical) reservoir system integrity? – A comprehensive experimental approach", experiments on powdered siderite separates are evaluated and discussed together with results from the sandstone and siltstone experiments (Fischer et al., submitted(B)). Baseline XRD data showed that the siderite separate is composed of siderite, ankerite and quartz. In three repeat experiments – two at 20 MPa and one at 30 MPa – it is shown that the influence of pressure on mineral solubility is rather negligible in the considered pressure range, and that siderite is more stable compared to ankerite.

Chapter 7 "Mineral solubilities in CO_2-saturated NaCl brine systems" comprises results of complementary experiments on monomineralic illite and labradorite powder separates (Fischer et al., 2013b). Baseline XRD data reveals that the illite separate is composed of illite, Ca-smectite, orthoclase and quartz, whereas the labradorite separate is pure labradorite. During respective experiments the Ca-smectite component is dissolved out of the illite-smectite mixed-layer mineral, and labradorite shows slightly dissolution during CO_2 exposure, respectively.

2. Publication I:

"CO_2-brine-rock interaction – First results of long-term exposure experiments at in situ P-T conditions of the Ketzin CO_2 reservoir"

CO$_2$–brine–rock interaction — First results of long-term exposure experiments at in situ P–T conditions of the Ketzin CO$_2$ reservoir

Sebastian Fischer [a,b,*], Axel Liebscher [a], Maren Wandrey [a], the CO$_2$SINK Group

[a] Helmholtz Centre Potsdam, GFZ German Research Centre for Geosciences, Centre for CO$_2$ Storage, Telegrafenberg, D-14473 Potsdam, Germany
[b] Technical University of Berlin, Section Mineralogy and Petrology, Ackerstraße 76, D-13355 Berlin, Germany

ARTICLE INFO

ABSTRACT

Sandstone samples of the Stuttgart Formation at Ketzin have been experimentally treated with CO$_2$ and synthetic reservoir brine in high-quality steel autoclaves at simulated in situ P–T conditions (5.5 MPa, 40 °C). In order to observe mineralogical changes induced by CO$_2$, untreated samples are compared to CO$_2$-treated ones. Most samples show an analogous petrography of mainly quartz and plagioclase. Heterogeneities are related to minor mineral phases, such as K-feldspar, hematite, muscovite, biotite, illite, chlorite and opaque phase(s). These are attributed to the variability of the fluvial reservoir sandstone. The samples are weakly consolidated. Analcime, dolomite and anhydrite are only found as cement phases. During the experiments dissolution of anhydrite and plagioclase is observed. SEM micrographs of CO$_2$-treated samples show corrosion textures on mineral surfaces of intermediate plagioclase, as well as precipitation of euhedral albite crystals. Overall, the data indicate preferred dissolution of calcium-rich plagioclase, K-feldspar and anhydrite and stabilization or precipitation of albite.

1. Introduction

Capture and subsequent geological storage of CO$_2$ is a key strategy within the portfolio of actions to reduce CO$_2$ emissions to the atmosphere. Deep saline aquifers are the most promising geological storage options on the regional to global scale based on their estimated storage capacities and their widespread distribution. For these deep saline aquifer systems, initial physico-chemical equilibrium between saline formation fluid and reservoir rock can be reasonably assumed. However, the injection of CO$_2$ into these saline aquifer systems disturbs this initial equilibrium and will trigger chemical interactions between injected CO$_2$, saline formation fluid and reservoir rock. These interactions include dissolution of certain minerals and precipitation of others and not only change the chemical, but also the physical properties of the reservoir system. The chemical interactions may lead to mobilization of certain, eventually harmful or toxic, elements while the changes in physical properties influence injectivity, storage capacity, as well as long-term safety and stability of the reservoir. Precise knowledge of the CO$_2$-induced interactions between injected CO$_2$, saline formation fluid and

reservoir rocks and of the resulting changes in chemical and physical properties of the reservoir system is therefore a prerequisite for any secure operation of a storage site. Unfortunately, due to the general lack of core samples from reservoir systems after onset of CO$_2$ injection, any information on CO$_2$-induced interactions at real storage sites are, at least up to now, indirect and mostly based on gas or fluid samples recovered from observation wells (e.g., Assayag et al., 2009). Experimental studies at simulated reservoir pressure and temperature conditions are an important and elegant way to overcome this problem. Such studies either focus on individual minerals (e.g., Daval et al., 2009; Hangx and Spiers, 2009) or on real reservoir rock samples (e.g., Kaszuba et al., 2003, 2005; Wigand et al., 2008). Kaszuba et al. (2003) studied CO$_2$–brine–arkose interactions during 139 days exposure experiments at 20 MPa and 200 °C. In these experiments, etch textures indicate dissolution of microcline, biotite and quartz. In addition, smectite and magnesite precipitated. In another experimental study at 20 MPa/200 °C and 77 days run duration, Kaszuba et al. (2005) observed dissolution of biotite and shale and concomitantly increasing concentrations of magnesium, iron and manganese in the brine. In these experiments, analcime crystallized during the run and lowered the sodium concentration of the brine. In batch CO$_2$-exposure experiments on Bunter Sandstone at 30 MPa/60 °C and 63 days run duration, Wigand et al. (2008) discovered dissolution of dolomite cement and etch textures on K-feldspar and albite; montmorillonite precipitated in cleavages of albite crystals. Given the vast mineralogical, chemical

* Corresponding author at: Helmholtz Centre Potsdam, GFZ German Research Centre for Geosciences, Centre for CO$_2$ Storage, Telegrafenberg, D-14473 Potsdam, Germany. Tel.: +49 331 288 28 37.
E-mail address: fischer@gfz-potsdam.de (S. Fischer).

and physical diversity of the different saline aquifer systems that may serve as potential storage sites, the number of experimental studies is, however, relatively small and the existing data base is insufficient to yield a conclusive picture of CO_2-induced interactions between injected CO_2, saline formation fluid and reservoir rocks for any specific storage site. This is especially true if one considers the low pressure and temperature conditions and therefore potentially sluggish reaction kinetics of the experiments in combination with the comparably short run durations. Further experimental studies that cover additional physico-chemical conditions (e.g., pressure, temperature, lithology, brine composition), refer to specific geological environments at individual storage sites, and address the problem of potential sluggish reaction kinetics by prolongated run durations are therefore urgently needed.

In order to add further data to the existing data base and to specifically address the CO_2-induced interactions at the pilot storage site at Ketzin, Brandenburg (Germany), we here present first results from long-term (15 months) CO_2-exposure experiments on core samples from the Ketzin reservoir rocks. The integrative strategy of these experiments was to jointly study the mineralogical, chemical, petrophysical as well as microbiological changes of the Ketzin reservoir rocks as induced by CO_2 on an identical set of samples. The petrophysical results are presented by Zemke et al. (2010), and the microbiological results in Wandrey et al. (accepted). In this contribution we focus on the observed mineralogical and chemical changes. We will show that although the mineralogical changes are only minor, the data provide clear evidence for preferred dissolution of certain minerals, e.g., plagioclase, with concomitant mobilization of calcium in the saline fluid.

1.1. The Ketzin pilot site

The pilot storage site at Ketzin, Brandenburg (Germany) is situated in the Northeast German Basin about 40 km west of Berlin. It is located on the south-eastern flank of the gently dipping Roskow-Ketzin double anticline, which formed above a west–east elongated salt pillow. A detailed description of the local geology is given in Förster et al. (accepted) and Norden et al. (2010). The Ketzin locality is the first European on-shore CO_2 storage site in a saline aquifer. In summer 2007, one injection well (Ktzi 201) and two observation wells (Ktzi 200 and 202) had been drilled to depths of 750–800 m. The wells are about 50 and 110 m away from each other and are arranged in a triangular shape (Schilling et al., 2009). Since June 2008, food-grade CO_2 with a purity of > 99.9 vol% is injected into sandstone horizons of the Upper Triassic (Middle Keuper) Stuttgart Formation on the south-eastern flank of the anticline. At Ketzin, the Stuttgart Formation has an average thickness of 75–80 m, while the main reservoir horizon is only 9–20 m thick (Norden et al., 2010). The Stuttgart Formation was deposited in a fluvial system, in which the sandstone horizons represent river channel deposits. This depositional environment causes a high lateral and vertical heterogeneity between, but also within, the individual sandstone horizons (Förster et al., accepted). The sandstones are typically fine-grained with a general modal composition of 35–39% quartz, $\sim20\%$ feldspar, 13–18% illite, $\sim5\%$ analcime, up to 10% anhydrite, plus minor but variable amounts of mica, dolomite, hematite, pyrite, chlorite; their porosity varies between 5% and $> 35\%$, and their permeability is between 0.02 and > 5000 mD (Norden et al., 2010). The reservoir horizon is located at 625–650 m depth, and the initial reservoir conditions were $\sim33\,°C/6.2$ MPa, which increased to $\sim33\,°C/7.5$ MPa during ongoing injection of CO_2. The actual reservoir conditions correspond to a CO_2 density of

~0.3 g/cm^3 (Span and Wagner, 1996), which is notably less than the CO_2 density of ~0.8 g/cm^3 targeted for future industrial-scale storage sites.

2. Materials and methods

2.1. Sample description

The studied core samples were recovered from observation well Ktzi 202. The coring was performed through the uppermost 18 m of the Stuttgart Formation to a maximum depth of 635.0 m (Norden et al., 2010). Five core sections, each 1 m in length, have been sampled from depths between 627.7 (B2-2) and 634.6 m (B4-2) (Fig. 1a, Table 1). Of these five core sections, a total of 14 individual samples (intact core pieces between 10 and 15 cm in length and 5 cm in diameter, but also cm-sized broken fragments; Fig. 1a) were selected for the present study and split into two subsets; subset 1 (untreated) was used to describe the initial mineralogy of core sections prior to the CO_2-experiments, and subset 2 (CO_2-treated) was used for the long-term experiments. Wherever possible, attention was paid to ensure that for each core section the different samples for subsets 1 and 2 were taken in close proximity to each other to minimize any initial heterogeneity between the samples and to allow for comparison between the two subsets. Nevertheless, certain heterogeneity between the different samples is apparent in hand specimen (Fig. 1a). Most samples are finely laminated on mm- to cm-scale. This lamination predominantly appears as alternating red-brown and dark-brown colors and is due to different grain sizes (more sandy versus more silty) next to slightly distinct modal quantities of especially clay minerals. Some samples exhibit a fine cross-bedding. Overall, the samples are only weakly consolidated and show a patchy distribution of cement, visible as uneven spread mm-sized brighter parts.

2.2. Experimental procedure

For 15 months, the samples of subset 2 were stored together with synthetic reservoir brine and pure CO_2 in high-quality steel pressure vessels that were placed in a heating cabinet at simulated reservoir conditions of 5.5 MPa and 40 °C. The synthetic reservoir brine had an initial composition of 172.8 g/l NaCl, 8.0 g/l $MgCl_2 \cdot 6H_2O$, 4.8 g/l $CaCl_2 \cdot 2H_2O$, and 0.6 g/l KCl according to data on the original Ketzin formation fluid available at the start of the experiments (Förster et al., 2006). Subsequent studies on the original Ketzin formation fluid showed that the synthetic brine unfortunately contains only about 81% of the total dissolved solids (TDS) of the original formation fluid and lacks any sulphate (Wandrey et al., 2010). Therefore, some mineral reactions are expected, which may not be related to the presence of CO_2.

2.3. Analytical techniques and methods

After the samples were taken out of the autoclaves they have been washed several times with pure H_2O and cautiously dried in a compartment drier at 45 °C. The samples were embedded in blue colored epoxy resin to enforce stability for sawing and thin section preparation. Thin sections are oriented perpendicular to the bedding planes and were prepared at the Section of Mineralogy at the Technical University of Berlin (TUB). A Leitz polarizing microscope was used for thin section analyses and to take micrographs. The grain size of each sample was measured on the average long-axes of 50 grains per sample using a software tool kit. Roundness and sorting were determined by standard charts for comparison (Pettijohn et al., 1987).

Powder specimens for X-ray diffraction analyses (XRD) with Rietveld refinement were obtained from each sample to determine the modal mineralogy. These powders were first homogenized in an agate mortar for a few minutes and then evenly spread on a circular foil. The XRD measurements were carried out at the TUB on a Phillips PW1050 with a Seifert Iso-Dedyeflex generator (40 kV, 20 mA) and a fixed divergence slit, as well as on a Phillips PW1050 with a Phillips PW1729 generator (40 kV, 30 mA) and an automatic divergence slit. Powder X-ray diffractograms were recorded between 5° and 80° 2-Theta with CuKα cross $(\alpha_{1,2})=1.5419$ Å. The detector step size was set to 0.02 with 2 s/step. Electron Microprobe (EMP) analyses was performed on a Cameca SX 100 at the GFZ. Accelerating voltage was 15 kV, beam current was 20 nA. The beam diameter was 5 μm for mica, 20 μm for carbonate, and 10 μm for feldspar and all other minerals. Scanning electron microscopy (SEM) was done on a Zeiss ultra 55 plus at the GFZ. The SEM operated at 20 kV and 15 nA and is equipped with an energy dispersive X-ray system (EDS). Analyses were done on small sample pieces. Backscattered electron (BSE) images were taken on polished thin sections also used for EMP measurements.
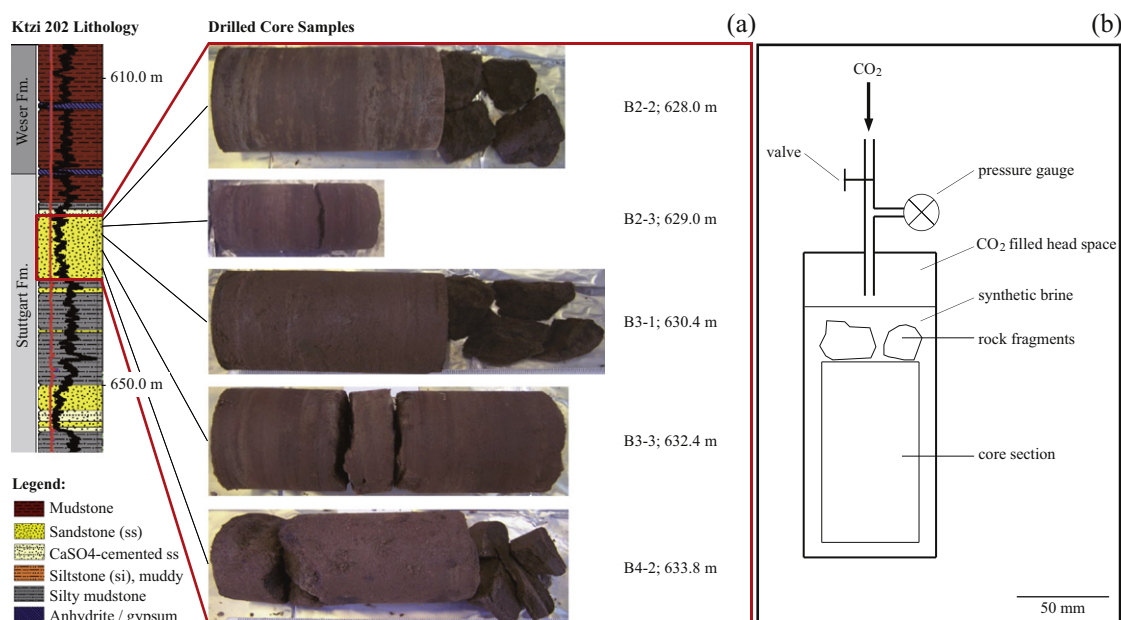
Fig. 1. (a) Profile of the Stuttgart Formation in observation well Ktzi 202, modified after Förster et al. (accepted). Shown is the depth interval of the saline aquifer sandstone next to the positions of the different samples. Photographs of the samples (cores and rock fragments) visualizing their internal heterogeneities. (b) Schematic sketch of the experimental setup. Not shown is the heating cabinet, which controls the temperature.

Table 1
Summary of the studied samples and their basic mineralogy determined by thin section, XRD and EMP analyses.

Sample		B2-2		B2-3		B3-1		B3-3		B4-2	
Depth (m)		627.7–628.7		628.7–629.6		629.6–630.6		631.6–632.6		633.6–634.6	
Number of individual samples		2		3		3		3		3	
CO_2 set		Untreated	$CO_{2\text{-treated}}$	Untreated	$CO_{2\text{-treated}}$	Untreated	$CO_{2\text{-treated}}$	Untreated	$CO_{2\text{-treated}}$	Untreated	$CO_{2\text{-treated}}$
Number of individual samples per set		1	1	2	1	2	1	2	1	2	1
Qtz		+	+	+	+	+	+	+	+	+	+
Pl		+	+	+	+	+	+	+	+	+	+
Kfs		o	o	o	o	o	o	o	o	o	/
Ms		–	–	–	–	–	–	–	–	–	–
Bt		/	–	–[a]	/	/	–	/	–	–[a]	–
Cement	Anh	o	o	o	o	o	/	o	/	o	/
	Anl	o	o	o	o	o	o	o	o	o	/
	Dol	o	o	o	o	/	/	/	/	/	/
Accessory	Fe – phase	–	–	–	–	–[b]	–[b]	–	–	–[b]	–
	Chl	/	/	–	–	–	–	–	–	–	–
	Ill										–

Categories: $+ = > 25\%$; o = 5–25%; $- = < 5\%$; / = not present.
Note: Mineral abbreviations after Kretz (1983); Fe-phase: subsumes opaque phases, iron-oxides and iron-hydroxides; Ill only listed when clearly identified.

[a] Biotite between 68 and 88 wt% only.
[b] Hematite present as proven by XRD.

3. Results

3.1. Petrography

In thin section, the analyzed samples are mainly fine grained ($< 200 \mu m$), moderately well- to well sorted, angular to sub-angular and only partly consolidated sandstones. The principal modal mineral composition as determined by optical microscopy, XRD measurements, EMP and SEM analyses is comparable between all samples (Table 1, Figs. 2 and 3). They are mainly composed of quartz and plagioclase; K-feldspar, mica, hematite, clay minerals, opaque phase(s) and lithoclasts are present in subordinate and varying amounts. Mica is predominantly muscovite with only minor amounts of biotite. Chlorite and illite are the most important clay minerals, which are often

associated with lithoclasts. These lithoclasts are predominantly composed of either quartz and sheet silicates or comprise feldspar with quartz, opaque phase(s), chlorite and illite. These observations are in good accordance with the results by Förster et al. (accepted). The samples are weakly cemented by anhydrite, analcime, and/or dolomite. The cements form unevenly distributed, isolated, poikilitic patches (Fig. 2a, b and d). Anhydrite and analcime are present in all untreated samples. In the CO_2-treated samples, however, anhydrite was not observed in samples from core sections B3-1, B3-3 and B4-2 and analcime does not occur in samples from core section B4-2. Dolomite is only present in both untreated and CO_2-treated samples from core sections B2-2 and B2-3. With the exception of anhydrite and analcime being absent in some of the CO_2-treated samples, the mineralogical variability between samples from subset 1 is larger
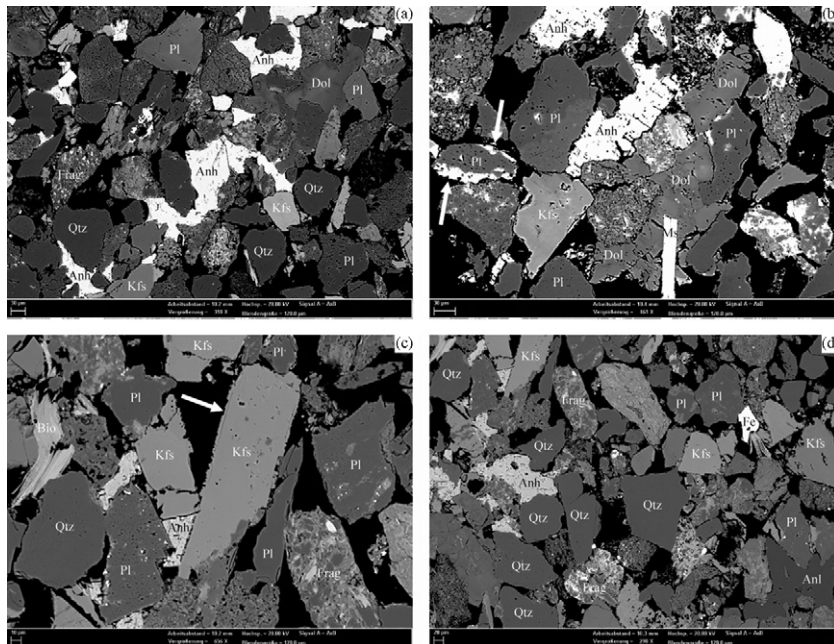
Fig. 2. BSE images of polished thin sections. Labeled are the major mineral phases; black colour represents pore space. (a) Sandstone cemented anhydrite and dolomite in the untreated sample B2-2. The arrows in (b) show marginal alteration of a plagioclase grain in the CO_2-treated sample B2-3. (c) Dissolution of K-feldspar grain (arrow). (d) Patchy pore-filling anhydrite and analcime. The latter two images (c) and (d) are taken from CO_2-treated sample B2-2. Abbreviations after Kretz (1983); Frag=rock fragments, Fe=iron-(hydr)oxide.
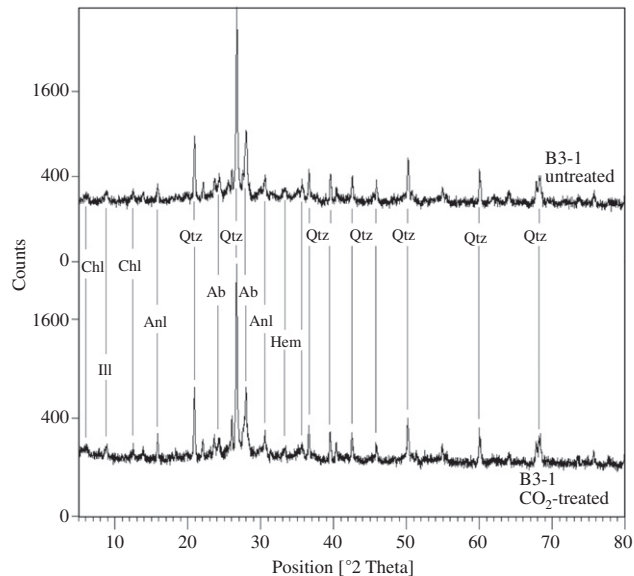
Fig. 3. Representative XRD diffractograms comparing the modal mineralogy of the twin sample B3-1. It is apparent that not only the peak positions, but also the intensities [counts] are similar for untreated (top) and CO_2-treated (bottom) measurements.

than that between untreated and CO_2-treated samples from identical core sections.

The heterogeneity and lamination of the samples observed in hand specimen is also apparent on the thin-section scale. Here, these heterogeneities are mostly caused by an uneven distribution of minor mineral phases like hematite, chlorite, illite and of the cement phases. The lamination is caused by alternation of lighter, quartz- and feldspar-dominated layers with darker, (red-) brownish to black layers, which are mainly composed of opaque phase(s) with notably less quartz, feldspars and cements. In some samples, these darker domains cover relatively large and inter-connected areas, while in others they occur in only scattered and elongated zones. In close vicinity to the dark layers, mineral grains with thin rims (coatings) are more frequent. These coatings were already described as iron(-titanium)-(hydr)oxides by Förster et al. (accepted); own EMP analyses suggest mostly hematite. According to the measurements by Zemke et al. (2010), the initial porosity of the samples varies between 20% and 30%.

3.2. Mineral surfaces

Mineral surfaces of quartz are generally clean and smooth without any signs of alteration (Fig. 4a). Micas show platy morphology with the typical basal cleavage and, like quartz, lack any signs of alteration (Fig. 4b). Anhydrite typically shows good cleavages in three directions. Despite the fact that anhydrite was not found in the CO_2-treated samples from three core sections (see above), which suggest dissolution of anhydrite, individual anhydrite crystals do not show any clear evidence of dissolution (Fig. 4c). Only plagioclase crystals show unambiguous evidence of alteration and dissolution. Plagioclase grains typically show either surfaces with crystallographically oriented etch textures (Fig. 4d) or lamellar dissolution features resulting in a lumpy and irregular surface morphology (Fig. 4e). Comparable dissolution textures are occasionally found in K-feldspar grains. However, here these textures are not that distinct. At times, pure albite grains may show absolutely clean and fresh euhedral crystal habit (Fig. 4f). These albite grains are, however, only found in the CO_2-treated samples and may have precipitated during the experiments.

3.3. Mineral composition

3.3.1. Feldspar

The feldspar composition before and after the experiments are shown in Fig. 5, and representative feldspar analyses are given in Tables 2a and 2b. No major compositional changes during the
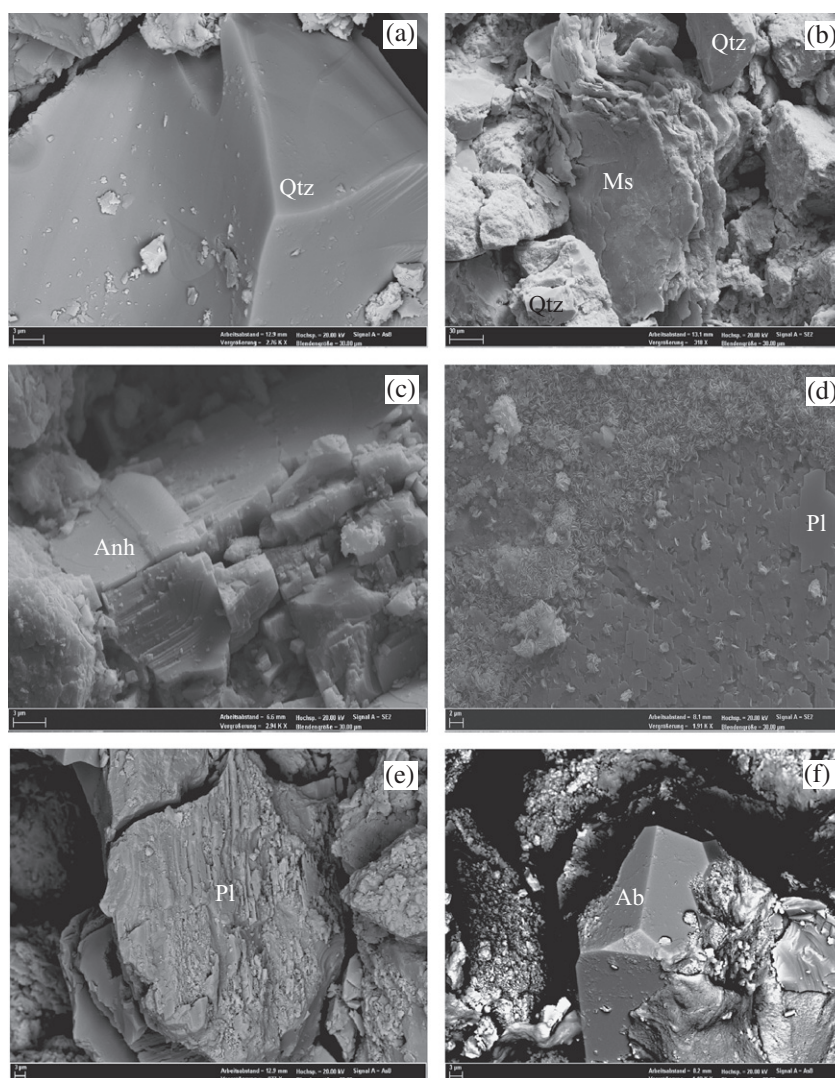
Fig. 4. SEM images taken on freshly broken fragments displaying the characteristic appearance of quartz (a) and (b), muscovite (b), and anhydrite (c). Corrosion textures on surfaces and edges of plagioclase grains are apparent in (d) and (e). (f) Euhedral albite crystal.

experiments are obvious. Plagioclase measurements show clusters with two different compositions: intermediate compositions have Ab_{40} to Ab_{80} with $Or_{<10}$, while albite rich compositions have $Ab_{>95}$. Maximum calcium contents in plagioclase are An_{59} in untreated and An_{55} in CO_2-treated samples. K-feldspar from untreated and CO_2-treated samples consistently ranges from Or_{70} to Or_{98}. Only very few measurements plot at intermediate alkali feldspar composition or in the compositional field of true ternary feldspars. These may reflect inaccuracies or measurements of mixed mineral phases. Despite the overall consistency of the feldspar composition before and after the experiments, the plagioclase composition indicates changes. Much more sodium-rich to pure albite grains have been measured in CO_2-treated samples compared to the untreated ones. Even more, pure albite ($Ab_{>99}$) was only found in the CO_2-treated samples. In combination with the petrographical observations (see above), this also indicates precipitation of pure albite during the experiments.

3.3.2. Sheet silicates

Representative analyses of sheet silicates are given in Table 3a. As for feldspar, no major changes in chemical composition during the experiments are obvious. White mica is predominantly muscovite; only one analysis showed paragonite. Octahedral aluminum in muscovite ranges from 1.43 to 1.92 cation per

formula unit (pfu), other octahedral cations are 0.04–0.39 iron pfu, 0.04–0.38 magnesium pfu and 0.01–0.17 titanium pfu. Potassium contents on the XII-fold coordinated A-site range from 0.46 to 0.96 pfu, and sodium concentrations are between 0.02 and 0.42 pfu. Dark mica is biotite of the phlogopite–annite solid solution series. Octahedral iron content ranges from 0.88 to 1.56 pfu, while magnesium is 0.70–1.34 pfu. Titanium contents are between 0.09 and 0.25 pfu and octahedral aluminum is 0.04–0.56 pfu. In biotite, the XII-fold coordinated A-site is exclusively occupied by potassium (0.58–0.96 pfu); A-site vacancies, i.e. a talc component, reach a maximum of 0.40 pfu. Biotite analyses from untreated samples of core sections B2-2 and B3-1 yield very low totals of <90 wt% oxides (not shown in Table 3) and may indicate notable chloritization of biotite in these samples. EMP analyses of chlorite indicate compositions of the chlinochlore–chamosite solid solution series.

3.3.3. Cement phases

All three cement phases anhydrite, analcime and dolomite consistently show stoichiometrical compositions before and after the experiments and provide no hints for any chemical alteration. Anhydrite forms relatively coarse (poikilitic) grains (Fig. 2a–d), but a chemical zoning, with respect to calcium and strontium as described by Förster et al. (accepted), was not observed. Analcime

has near end-member composition and forms smaller crystals that appear to be very homogenous and optically clear (Fig. 2d). Dolomite cement occurs as isolated, blocky patches (Fig. 2a and b) and has a very uniform composition of calcium and magnesium both approximately accounting for 0.50 pfu. Only traces of iron and manganese were detectable. These little concentrations are likely to be the reason for the shaded appearance observable in the BSE images of Fig. 2a and b.

4. Discussion

The presented data only show minor mineralogical changes during the experiments. The variability between comparable samples before and after the experiments is lower than the overall
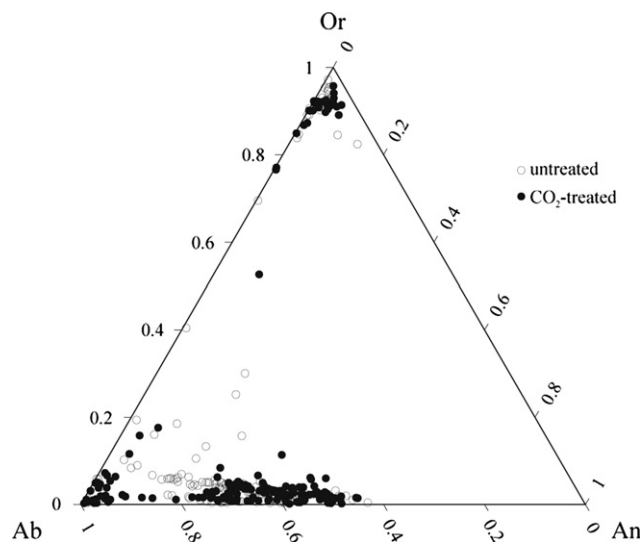
Fig. 5. EMP data displaying the feldspar chemistry of untreated (open circles) and CO_2-treated samples (filled circle). While no changes are indicated for K-feldspars, much more albite minerals occur in the CO_2-treated samples.

variability of the studied samples and no significant changes in mineralogy were observed. Nevertheless, several lines of evidence indicate chemical interactions between CO_2, brine and sandstone samples during the experiments. The presence of anhydrite in all untreated samples, but its absence in CO_2-treated samples from core sections B3-1, B3-3 and B4-2 is at least indicative of anhydrite dissolution. The distinct corrosion and etch textures on plagioclase surfaces, and also on K-feldspar surfaces clearly indicate preferred dissolution of these minerals. On the other hand, euhedral albite grains occurring in CO_2-treated samples suggest precipitation of albite, most likely in expense of plagioclase, during the experiments. Dissolution of certain minerals is consistent with results from porosity measurements on the same samples (Zemke et al., 2010). These measurements generally indicate a slight increase in porosity during the experiments and also imply dissolution processes. Preferred dissolution of anhydrite and of the anorthite component of plagioclase should also increase the calcium and sulfate concentrations in the brine, as long as no other calcium- and/or sulphate-bearing minerals precipitate. Again, this is consistent with first data on the composition of the synthetic brine. After 15 months, the calcium and sulfate (but also potassium and magnesium) concentrations in the brine have notably increased (Wandrey et al., accepted). As the initial concentrations of calcium and sulfate in the synthetic brine were below those of the Ketzin formation fluid (see above), one may argue that this increase in concentration simply reflects the evolution of the synthetic brine to its potential equilibrium composition, without any influence of CO_2. However, the measured concentrations of calcium, potassium and magnesium in the brine after the experiments are notably higher than those of the original Ketzin formation fluid. Accordingly, these cannot only be explained by the above mentioned attainment of equilibrium without any influence of CO_2. Overall, the data presented in this paper in combination with those given by Wandrey et al. (accepted, 2010), as well as Zemke et al. (2010) clearly indicate that the addition of CO_2 triggered preferred dissolution of the anorthite component of plagioclase, dissolution of K-feldspar and anhydrite and precipitation of pure albite.

Table 2a
Representative K-feldspar compositions determined by EMP analyses.

	B2-2		B2-3		B3-1		B3-3		B4-2	
	Untreated	**CO_2-treated**	**Untreated**	**CO_2-treated**	**Untreated**	**CO_2-treated**	**Untreated**	**CO_2-treated**	**Untreated**	**CO_2-treated**
SiO_2	65.73	64.55	65.38	64.25	65.13	64.25	64.90	65.30	64.25	65.21
Al_2O_3	17.23	18.66	18.48	18.84	18.64	18.49	18.48	18.51	18.66	18.57
MgO	0.07	0.00	0.00	0.01	0.02	0.00	0.00	0.01	0.00	0.01
FeO	0.45	0.04	0.00	0.07	0.12	0.39	0.11	0.12	0.18	0.03
CaO	0.72	0.00	0.00	0.00	0.02	0.00	0.02	0.00	0.00	0.00
BaO	0.36	0.18	0.21	1.22	0.05	0.31	0.55	0.22	0.22	0.14
Na_2O	0.76	0.76	1.05	0.57	0.34	0.77	0.54	0.85	0.53	1.21
K_2O	14.35	15.85	15.49	15.42	16.27	15.58	15.72	15.75	16.20	15.31
Σ	99.66	100.04	100.62	100.37	100.59	99.80	100.32	100.75	100.04	100.47
Normalized to 8 oxygen										
Si	3.04	2.98	3.00	2.98	2.99	2.98	3.00	3.00	2.98	2.99
Al	0.94	1.02	1.00	1.03	1.01	1.01	1.01	1.00	1.02	1.00
Σ	3.98	4.00	4.00	4.01	4.00	3.99	4.01	4.00	4.00	3.99
K	0.85	0.93	0.91	0.91	0.95	0.92	0.93	0.92	0.96	0.90
Ca	0.04	0.00	0.00	0.00	0.00	0.00	0.00	0.00	0.00	0.00
Na	0.07	0.07	0.09	0.05	0.03	0.07	0.05	0.08	0.05	0.11
Ba	0.01	0.00	0.00	0.02	0.00	0.01	0.01	0.00	0.00	0.00
Mg	0.00	0.00	0.00	0.00	0.00	0.00	0.00	0.00	0.00	0.00
Fe	0.02	0.00	0.00	0.00	0.00	0.02	0.00	0.00	0.01	0.00
Σ	0.98	1.01	1.00	0.99	0.99	1.01	0.99	1.01	1.02	1.01
x_{kfs}	0.88	0.93	0.90	0.93	0.97	0.92	0.94	0.92	0.95	0.89
x_{an}	0.04	0.00	0.00	0.00	0.00	0.00	0.00	0.00	0.00	0.00
x_{ab}	0.07	0.07	0.09	0.05	0.03	0.07	0.05	0.08	0.05	0.11

Table 2b
Representative plagioclase compositions determined by EMP analyses.

B2-2

	Untreated		CO$_2$-treated		
SiO$_2$	62.49	67.14	57.49	60.69	65.30
Al$_2$O$_3$	23.05	20.65	27.51	24.95	22.11
MgO	0.00	0.12	0.00	0.00	0.08
FeO	0.23	0.18	0.32	0.20	0.96
CaO	4.21	1.02	8.53	6.29	0.59
BaO	0.09	0.03	0.01	0.03	0.41
Na$_2$O	9.06	11.36	6.79	8.41	10.72
K$_2$O	0.92	0.11	0.18	0.19	0.00
Σ	100.04	100.61	100.84	100.76	100.17
Normalized to 8 oxygen					
Si	2.78	2.93	2.56	2.69	2.87
Al	1.21	1.06	1.44	1.30	1.15
Σ	3.99	3.99	4.00	3.99	4.02
K	0.05	0.01	0.01	0.01	0.05
Ca	0.20	0.05	0.41	0.30	0.03
Na	0.78	0.96	0.59	0.72	0.91
Ba	0.00	0.00	0.00	0.00	0.00
Mg	0.00	0.01	0.00	0.00	0.01
Fe	0.01	0.01	0.01	0.01	0.02
Σ	1.04	1.03	1.02	1.04	1.02
x_{Kfs}	0.05	0.01	0.01	0.01	0.05
x_{an}	0.19	0.05	0.41	0.29	0.03
x_{ab}	0.76	0.95	0.58	0.70	0.92

B2-3

	Untreated		CO$_2$-treated	
SiO$_2$	60.64	67.11	67.01	56.99
Al$_2$O$_3$	24.79	20.71	20.06	27.49
MgO	0.01	0.00	0.01	0.00
FeO	0.22	0.08	0.17	0.07
CaO	6.14	0.72	0.46	9.24
BaO	0.03	0.00	0.30	0.00
Na$_2$O	8.09	11.85	11.71	6.76
K$_2$O	0.89	0.05	0.01	0.03
Σ	100.80	100.52	99.73	100.58
Normalized to 8 oxygen				
Si	2.69	2.93	2.95	2.55
Al	1.30	1.07	1.04	1.45
Σ	3.99	4.00	3.99	4.00
K	0.05	0.00	0.01	0.00
Ca	0.29	0.03	0.02	0.44
Na	0.70	1.00	1.00	0.59
Ba	0.00	0.00	0.00	0.00
Mg	0.00	0.00	0.00	0.00
Fe	0.01	0.00	0.01	0.00
Σ	1.05	1.04	1.04	1.03
x_{Kfs}	0.05	0.00	0.01	0.00
x_{an}	0.28	0.03	0.02	0.43
x_{ab}	0.67	0.96	0.97	0.57

B3-1

	Untreated		CO$_2$-treated			
SiO$_2$	63.01	66.59	59.44	63.31	67.20	55.26
Al$_2$O$_3$	23.22	20.19	25.00	24.14	19.26	27.57
MgO	0.00	0.00	0.01	0.25	0.08	0.01
FeO	0.31	0.06	0.35	0.64	0.84	0.31
CaO	4.22	0.76	6.88	0.37	0.08	9.87
BaO	0.00	0.04	0.06	0.00	0.31	0.09
Na$_2$O	9.30	11.71	7.46	8.86	11.22	5.89
K$_2$O	1.06	0.03	0.59	3.13	0.02	0.52
Σ	101.11	99.39	99.80	100.70	99.00	99.52
Normalized to 8 oxygen						
Si	2.78	2.94	2.67	2.80	2.98	2.51
Al	1.21	1.05	1.32	1.26	1.01	1.48
Σ	3.98	3.99	3.99	4.05	3.99	3.99
K	0.06	0.00	0.03	0.18	0.05	0.03
Ca	0.20	0.04	0.33	0.02	0.00	0.48
Na	0.79	1.00	0.65	0.76	0.97	0.52
Ba	0.00	0.00	0.00	0.00	0.00	0.00
Mg	0.00	0.00	0.00	0.02	0.01	0.00
Fe	0.01	0.00	0.01	0.02	0.01	0.01
Σ	1.06	1.04	1.03	0.99	1.03	1.04
x_{Kfs}	0.06	0.00	0.03	0.18	0.05	0.03
x_{an}	0.19	0.03	0.33	0.02	0.00	0.47
x_{ab}	0.75	0.96	0.64	0.80	0.95	0.50

B3-3

	Untreated		CO$_2$-treated		
SiO$_2$	63.08	63.66	55.03	59.94	54.24
Al$_2$O$_3$	22.51	21.33	28.56	24.56	28.32
MgO	0.00	0.27	0.00	0.00	0.10
FeO	0.30	1.17	0.30	0.32	0.61
CaO	3.87	0.15	10.75	5.88	11.35
BaO	0.08	0.09	0.00	0.05	0.00
Na$_2$O	9.00	10.75	5.49	8.46	5.05
K$_2$O	1.10	1.03	0.35	0.50	0.26
Σ	99.93	98.46	100.48	99.71	99.92
Normalized to 8 oxygen					
Si	2.81	2.87	2.48	2.69	2.46
Al	1.18	1.13	1.51	1.30	1.51
Σ	3.99	4.00	3.99	3.99	3.97
K	0.06	0.06	0.02	0.03	0.01
Ca	0.18	0.01	0.52	0.28	0.55
Na	0.78	0.94	0.48	0.74	0.44
Ba	0.00	0.00	0.00	0.00	0.00
Mg	0.00	0.02	0.00	0.00	0.00
Fe	0.01	0.04	0.01	0.01	0.02
Σ	1.04	1.07	1.03	1.06	1.04
x_{Kfs}	0.06	0.06	0.02	0.03	0.01
x_{an}	0.18	0.01	0.51	0.27	0.55
x_{ab}	0.76	0.93	0.47	0.70	0.44

B4-2

	Untreated		CO$_2$-treated				
SiO$_2$	62.95	68.58	67.42	58.58	60.11	65.19	60.38
Al$_2$O$_3$	23.25	19.75	19.86	26.08	24.87	21.52	24.55
MgO	0.00	0.01	0.10	0.02	0.02	0.00	0.00
FeO	0.13	0.06	0.32	0.11	0.01	0.33	0.29
CaO	4.65	0.06	0.14	7.54	6.07	2.39	6.27
BaO	0.15	0.05	0.04	0.04	0.03	0.08	0.08
Na$_2$O	8.85	12.12	12.22	7.50	8.48	10.56	7.65
K$_2$O	0.75	0.00	0.06	0.51	0.27	0.25	0.92
Σ	100.72	100.63	100.12	100.38	99.86	100.32	100.13
Normalized to 8 oxygen							
Si	2.78	2.98	2.96	2.62	2.68	2.87	2.70
Al	1.21	1.01	1.03	1.37	1.31	1.12	1.29
Σ	3.99	3.99	3.99	3.99	3.99	3.99	3.99
K	0.04	0.00	0.00	0.03	0.02	0.02	0.05
Ca	0.22	0.00	0.01	0.36	0.29	0.11	0.30
Na	0.76	1.02	1.04	0.65	0.73	0.90	0.66
Ba	0.00	0.00	0.00	0.00	0.00	0.00	0.00
Mg	0.00	0.00	0.01	0.00	0.00	0.00	0.00
Fe	0.01	0.00	0.01	0.01	0.01	0.00	0.01
Σ	1.03	1.03	1.07	1.05	1.04	1.04	1.02
x_{Kfs}	0.04	0.00	0.00	0.03	0.02	0.02	0.05
x_{an}	0.22	0.00	0.01	0.35	0.28	0.11	0.30
x_{ab}	0.74	0.99	0.99	0.62	0.71	0.87	0.65

Table 3a
Representative mica compositions as determined by EMP analyses.

	B2-2		B3-1		B3-3		B4-2	
	Untreated Ms	CO_2-treated Bio	Untreated Ms	CO_2-treated Bio	untreated Ms	CO_2-treated Ms	Untreated Ms	CO_2-treated Ms
SiO_2	48.10	34.53	46.60	42.52	48.29	46.42	44.59	47.35
Al_2O_3	30.79	13.10	30.51	17.53	30.21	34.01	35.21	31.63
MgO	2.02	8.71	1.64	12.55	1.01	0.60	0.66	1.14
FeO	2.56	23.10	4.41	14.65	4.70	2.89	2.07	3.20
TiO_2	0.42	4.11	0.80	1.75	0.53	0.60	1.05	0.19
MnO	0.04	0.28	0.00	0.18	0.03	0.02	0.01	0.03
CaO	0.09	0.04	0.00	0.14	0.07	0.04	0.01	0.07
BaO	0.27	0.56	0.15	0.19	0.12	0.35	0.09	0.09
Na_2O	0.29	0.51	0.73	0.11	0.32	1.00	0.43	0.25
K_2O	10.99	8.10	10.07	6.78	10.19	9.37	10.73	10.58
F	0.02	1.33	0.00	0.13	0.01	0.03	0.04	0.39
Cl	0.00	0.20	0.00	0.07	0.01	0.00	0.00	0.00
	95.58	94.58	94.91	96.58	95.47	95.31	94.87	94.91
Normalized to 11 oxygen								
Si	3.23	2.79	3.18	3.05	3.20	3.12	3.02	3.20
Al	0.77	1.21	0.82	0.95	0.80	0.88	0.98	0.80
Σ	4.00	4.00	4.00	4.00	4.00	4.00	4.00	4.00
Al	1.67	0.04	1.64	0.53	1.67	1.81	1.83	1.72
Mg	0.20	1.05	0.17	1.34	0.10	0.06	0.07	0.11
Fe	0.14	1.56	0.25	0.88	0.27	0.16	0.12	0.18
Ti	0.02	0.25	0.04	0.09	0.03	0.03	0.05	0.01
Mn	0.00	0.02	0.00	0.01	0.00	0.00	0.00	0.00
Σ	2.04	2.92	2.10	2.86	2.08	2.06	2.07	2.02
K	0.94	0.84	0.88	0.62	0.90	0.80	0.93	0.91
Na	0.04	0.08	0.10	0.02	0.04	0.13	0.06	0.03
Ca	0.01	0.00	0.00	0.01	0.01	0.00	0.00	0.00
Ba	0.01	0.02	0.00	0.01	0.00	0.01	0.00	0.00
Σ	1.00	0.94	0.98	0.65	0.95	0.94	0.99	0.94

Note: Mineral abbreviations after Kretz (1983).

Table 3b
Representative analcime compositions determined by EMP analyses.

	B2-2		B2-3[a]	B3-1		B3-3		B4-2[b]
	Untreated	CO_2-treated	CO_2-treated	Untreated	CO_2-treated	Untreated	CO_2-treated	Untreated
SiO_2	61.49	59.77	58.34	60.65	59.18	59.43	59.34	59.73
Al_2O_3	22.57	21.22	22.12	21.90	21.85	22.38	21.60	21.97
MgO	0.00	0.00	0.00	0.00	0.00	0.00	0.00	0.00
FeO	0.03	0.05	0.00	0.00	0.05	0.08	0.03	0.02
TiO_2	0.00	0.01	0.01	0.00	0.00	0.00	0.00	0.00
MnO	0.00	0.02	0.02	0.00	0.04	0.02	0.01	0.00
CaO	0.00	0.00	0.02	0.00	0.01	0.01	0.00	0.00
Na_2O	13.00	13.23	13.83	13.25	13.22	13.44	13.16	13.22
K_2O	0.01	0.02	0.02	0.03	0.00	0.01	0.02	0.01
Cl	0.01	0.00	0.00	0.01	0.01	0.00	0.00	0.00
SO_2	0.00	0.00	0.00	0.00	0.00	0.00	0.01	0.00
Σ	97.11	94.33	94.35	95.88	94.33	95.37	94.15	94.95
Normalized to 6 oxygen								
Si	2.10	2.11	2.07	2.10	2.09	2.08	2.10	2.09
Al	0.91	0.88	0.92	0.90	0.91	0.92	0.90	0.91
Σ	3.01	2.99	2.99	3.00	3.00	3.00	3.00	3.00
Na	0.86	0.91	0.95	0.89	0.91	0.91	0.90	0.90
K	0.00	0.00	0.00	0.00	0.00	0.00	0.00	0.00
Ca	0.00	0.00	0.00	0.00	0.00	0.00	0.00	0.00
Σ	0.86	0.91	0.95	0.89	0.91	0.91	0.90	0.90

Note: Mg, Fe, Ti, Mn, Cl and S are all < 0.005 after normalization and not listed.

[a] No EMP measurement for untreated set B2-3 available.
[b] No EMP measurement for CO_2-treated set B4-2 available.

The indicated corrosion effects are observable in SEM micrographs, in which the plagioclase crystals display heavily altered edges with holes, etched pits and lamellae. These features were not observed – at least not to that degree – in the untreated samples and thus suggest intensified alteration processes during the experiments triggered by CO_2. But as Bertier et al. (2006) also discussed, it is generally difficult to quantify alterations of alumosilicates (e.g. feldspars), when pre-experimental, diagenetic

alterations of these minerals exist. In contrast to that, fresh and unaltered euhedral albite grains in some of the CO_2-treated samples (Fig. 4f) clearly suggest equilibrium between albite and the brine-CO_2 fluid. Because the feldspar composition observed in EMP analyses shows preferred occurrence of pure albite minerals after the CO_2 treatment, it is reasonable to assume precipitation of these euhedral albite grains during the experiments. But Förster et al. (accepted) also determined albite end-member compositions as a result of diagenetic albitization of both plagioclase and K-feldspar. On the other hand, Bertier et al. (2006) likewise observed new formed albite minerals during lab-experiments. Still it is possible that the higher number of albite measurements after the experiments are owed to the natural variability of the reservoir system, possibly displaying some statistical artifacts. Independent of CO_2-exposure lab-experiments, Blum and Stillings (1995) reported that in acidic environments, feldspar weathering rates are generally higher for calcic plagioclase compared to sodic plagioclase. And also Deer et al. (1992) stated that during hydrothermal plagioclase alteration, sodic varieties are more stable than those richer in the anorthite component. This kinetic mechanism is related to the structure of albite and anorthite. While an extensive framework of linked silicate tetrahedra, which are resistant to hydrolysis relative to aluminate sites, characterize the structure of albite, in anorthite, on the contrary, silicate tetrahedra are isolated from one another by aluminate groups so that selective hydrolysis (of aluminum) completely disrupts the anorthite structure (Casey et al., 1991), respectively. Parallel to this statement, Sass et al. (1999) debated that calcium was partially replaced by sodium in feldspar reactions occurring during the interaction of rock minerals (feldspar and clay) with CO_2 and brine. Shmulovich and Graham (2008) concluded that an increase in the bulk salinity of the fluid stimulates reactions in which alkali earth cations (e.g. calcium) are substituted for alkalis (e.g. sodium).

While quartz does not show any signs of dissolution, K-feldspars also seems to be partly dissolved during the CO_2 treatment. Comparable to plagioclase but less frequent, some K-feldspar grains in CO_2-treated samples show corrosion textures (Fig. 2c). Yet it is hardly possible to differentiate diagenetic and experimental, CO_2-induced alteration processes (see above). Similar alterations of K-feldspar during CO_2-exposure experiments have also been reported by Parry et al. (2007).

Although mica minerals do not occur in large quantity, they are an important component of the reservoir and complete the understanding of the reservoir system behavior. Additionally, alterations of mica minerals could easily lead to the formation of clay minerals, such as kaolinite, illite and chlorite, which may have an impact on petrophysical properties of the reservoir. These authigenic clays could clog pore throats and fill open cleavages to reduce poroperm levels and in turn hamper the injection of CO_2. Precipitation of smectite, intergrown with magnesite on biotite has already been reported by Kaszuba et al. (2003). Shiraki and Dunn (2000) presumed that a permeability decrease due to the formation of clay minerals could be a characteristical feature of CO_2 storage in formations containing alumosilicate minerals. On the other hand, Watson et al. (2004) concluded that reservoirs rich in feldspars and labile rock fragments, which can react with CO_2 to form new solid carbonate phases, are important for a save and successful long-term storage site. (Of course an effective poroperm level has to be assured at the same time.) In the here presented study, no unambiguous evidence for such mica alterations or intensified clay mineral formation was found, although these are likely to occur. Only illitization of muscovite could be indicated by the lowered potassium and aluminum contents of muscovite during the runs. Förster et al. (accepted) did furthermore report chloritization of detrital biotite triggered by diagenetic processes in the Stuttgart Formation.

Cements are in general a very important feature of reservoir systems because of influencing hydraulical parameters like porosity, permeability, and injectivity, which are vital for a successful site operation. Hence, they need to be carefully analyzed concerning mineralogical changes, precipitation and dissolution kinetics. The discussed dissolution of anhydrite was also observed by Shiraki and Dunn (2000) during core-flooding experiments on reservoir sandstones saturated with synthetic reservoir brine and CO_2.

The increased TDS concentration in the brine due to the dissolution of plagioclase, K-feldspar and anhydrite may trigger subsequent precipitation of carbonate phases. Such carbonate formation in different sandstones during laboratory CO_2-experiments has been described by, e.g., Czernichowski-Lauriol et al. (2006), Parry et al. (2007), Ketzer et al. (2009) and Kampman et al. (2009). However, analogous reactions have not yet been observed in the studied samples of the Stuttgart Formation but might only be a matter of time.

5. Conclusions

The petrological investigations observed by thin section analysis and XRD showed no significant mineralogical or petrochemical changes after the experiments. The variability of the Stuttgart Formation, which is primarily attributed to the sandstone sedimentation in a meandering, fluvial environment generating the incised-valley deposition with shoe-string-like sandstone bodies, is higher than that between untreated and CO_2-treated samples. Accordingly, the natural variability of the reservoir hampers the comparability of samples before and after CO_2 exposure. The cement phases do show analogous mineralogy and no signs of alteration except dissolution of anhydrite. Corrosion textures on feldspar minerals (plagioclase and K-feldspar) indicate alteration processes, while euhedral albite crystals suggest stabilization or even precipitation. The increased number of pure albite grains indicates albitization alongside preferred anorthite dissolution. Based on our data, the integrity of the reservoir formation at Ketzin is not affected by CO_2.

References

Assayag, N., Matter, J., Ader, M., Goldberg, D., Agrinier, P., 2009. Water–rock interactions during a CO_2 injection field-test: implications on host rock dissolution and alteration effects. Chem. Geol. 265, 227–235.
Bertier, P., Swennen, R., Laenen, B., Lagrou, D., Dreesen, R., 2006. Experimental identification of CO_2–water–rock interactions caused by sequestration of CO_2 in Westphalian and Buntsandstein sandstones of the Campine Basin (NE Beldium). J. Geochem. Explor. 89, 10–14.

Blum, A.E., Stillings, L.L., 1995. Feldspar dissolution kinetics. Chemical Weathering Rates of Silicate Minerals, Min. Soc. Am. 31, 291–351.

Casey, W.H., Westrich, H.R., Holdren, G.R., 1991. Dissolution rates of plagioclase at $pH=2$ and 3. Am. Mineral. 76, 211–217.

Czernichowski-Lauriol, I., Rochelle, C., Gaus, I., Azaroual, M., Pearce, J., Durst, P., 2006. Geochemical interactions between CO_2, pore-water and reservoir rock. Adv. Geolog. Storage Carbon Dioxide 65, 157–174.

Daval, D., Martinez, I., Corvisier, J., Findling, N., Goffé, B., Guyot, F., 2009. Carbonation of Ca-bearing silicates, the case of wollastonite: experimental investigations and kinetic modeling. Chem. Geol. 265, 63–78.

Deer, W.A., Howie, R.A., Zussman, J., 1992. An Introduction to the Rock-Forming Minerals (2nd Edition) Prentice Hall, London.

Förster, A., Norden, B., Zinck-Jorgensen, K., Frykman, P., Kuhlenkampff, J., Spangenberg, E., Erzinger, J., Zimmer, M., Kopp, J., Borm, G., Juhlin, C., Cosma, C.-G., Hurter, S., 2006. Baseline characterization of the CO_2SINK geological storage site at Ketzin, Germany. Environ. Geosci. 13 (3), 145–161.

Förster, A., Schöner, R., Förster, H.-J., Norden, B., Blaschke, A.-W., Luckert, J., Beutler, G., Gaupp, R., Rhede, D. The Upper Triassic Stuttgart Formation (Middle Keuper) at Ketzin: the reservoir for pilot CO_2 storage in the Northeast German Basin. Mar. Pet. Geol., accepted.

Hangx, S.J.T., Spiers, C.J., 2009. Reaction of plagioclase feldspars with CO_2 under hydrothermal conditions. Chem. Geol. 265, 88–98.

Kampman, N., Bickle, M., Becker, J., Assayag, N., Chapman, H., 2009. Feldspar dissolution kinetics and Gibbs free energy dependence in a CO_2-enriched groundwater system, Green River, Utah. Earth Planet. Sci. Lett. 284, 473–488.

Kaszuba, J.P., Janecky, D.R., Snow, M.G., 2003. Carbon dioxide reaction processes in a modal brine aquifer at 200 °C and 200 bars: implications for geological sequestration of carbon. Appl. Geochem. 18, 1065–1080.

Kaszuba, J.P., Janecky, D.R., Snow, M.G., 2005. Experimental evaluation of mixed reactions between supercritical carbon dioxide and NaCl brine: relevance to the integrity of a geologic carbon repository. Chem. Geol. 217, 277–293.

Ketzer, J.M., Iglesias, R., Einloft, S., Dullius, J., Ligabue, R., de Lima, V., 2009. Water–rock–CO_2 interactions in saline aquifers aimed for carbon dioxide storage: experimental and numerical modeling studies of the Rio Bonito Formation (Permian), southern Brazil. Appl. Geochem. 24 (5), 760–767.

Kretz, R., 1983. Symbols for rock-forming minerals. Am. Mineral. 68, 277–279.

Norden, B., Förster, A., Vu-Hoang, D., Marcelis, F., Springer, N., Le Nir, I., 2010. Lithological and petrophysical core-log interpretation in the CO_2SINK, the European CO_2 onshore research storage and verification project. SPE Reserv. Evaluat. Eng. 13 (2), 179–192.

Parry, W.T., Forster, C.B., Evans, J.P., Bowen, B.B., Chan, M.A., 2007. Geochemistry of CO_2 sequestration in the Jurassic Navajo Sandstone, Colorado Plateau, Utah. Environ. Geosci. 14 (2), 91–109.

Pettijohn, F.J., Potter, P.E., Siever, R., 1987. Sand and Sandstones. Springer, New York.

Sass, B.M., Gupta, N., Ickes, J.A., Engelhard, M.H., Baer, D.R., Bergman, P., Byrer, C., 1999. Interaction of rock minerals with carbon dioxide and brine: a hydrothermal investigation. In: Conference Proceedings CD, First National Conference on Carbon Sequestration, Washington, DC.

Schilling, F., Borm, G., Würdemann, H., Möller, F., Kühn, M., the CO_2SINK Group, 2009. Status report on the first European on-shore CO_2 storage site at Ketzin (Germany). Energy Procedia 1 (1), 2029–2035.

Shiraki, R., Dunn, T.L., 2000. Experimental study on water–rock interactions during CO_2 flooding in the Tensleep Formation, Wyoming, USA. Appl. Geochem. 15, 265–279.

Shmulovich, K.I., Graham, C., 2008. Plagioclase-aqueous solution equilibrium: concentration dependence. Petrology 16 (2), 177–192.

Span, R., Wagner, W., 1996. A new equation for carbon dioxide covering the fluid region from the triple-point temperature to 1100 K at pressures up to 800 MPa. J. Phys. Chem. 25 (6), 1509–1596.

Wandrey, M., Fischer, S., Zemke, K., Liebscher, A., Scherf, A.-K., Vieth, A., Zettlitzer, M., Würdemann, H. Monitoring petrophysical, mineralogical, geochemical and microbiological effects of CO_2 exposure — results of long-term experiments under in situ condition. GHGT 10, Amsterdam, accepted.

Wandrey, M., Morozova, D., Zettlitzer, M., Würdemann, H., and the CO_2SINK Group, 2010. Assessing drilling mud and technical fluid contamination in rock core and brine samples intended for microbiological monitoring at the CO_2 storage site in Ketzin using fluorescent dye tracers. Int. J. Greenhouse Gas Control, doi:10.1016/j.ijggc.2010.05.012.

Watson, M.N., Zwingmann, N., Lemon, N., 2004. The ladbroke grove-katnook carbon dioxide natural laboratory: a recent CO_2 accumulation in a lithic sandstone reservoir. Energy 29 (9–10), 1457–1466.

Wigand, M., Carey, J.W., Schütt, H., Spangenberg, E., Erzinger, J., 2008. Geochemical Effects of CO_2 sequestration in sandstones under simulated in situ conditions of deep saline aquifers. Appl. Geochem. 23, 2735–2745.

Zemke, K., Liebscher, A., Wandrey, M., the CO_2SINK Group, 2010. Petrophysical analysis to investigate the effects of carbon dioxide storage in a subsurface saline aquifer at Ketzin, Germany (CO_2SINK). Int. J. Greenhouse Gas Control, doi:10.1016/j.ijggc.2010.04.008.

3. Publication II:

"Petrophysical and petrochemical effects of long-term CO₂-exposure experiments on brine-saturated reservoir sandstone"

ELSEVIER

GHGT-10

Petrophysical and petrochemical effects of long-term CO_2-exposure experiments on brine-saturated reservoir sandstone

Sebastian Fischer[a,b,*]1, Kornelia Zemke[a], Axel Liebscher[a], Maren Wandrey[a], and the CO_2SINK Group

[a]*Helmholtz Centre Potsdam, GFZ German Research Centre for Geosciences, Centre for CO₂ Storage, Telegrafenberg, 14473 Potsdam, Germany*
[b]*Technical University of Berlin, Faculty VI, Section Mineralogy and Petrology, Ackerstraße 76, 13355 Berlin, Germany*

Abstract

Sandstone samples of the Stuttgart Formation at Ketzin have been experimentally treated with CO_2 and synthetic reservoir brine in high-quality steel autoclaves at simulated in situ P-T conditions of 5.5 MPa and 40 °C. In order to observe mineralogical changes induced by CO_2, untreated samples are compared to CO_2-treated ones. Samples show a comparable petrography of mainly quartz and plagioclase. Heterogeneities are related to minor mineral phases, such as K-feldspar, hematite, muscovite, biotite, illite, chlorite, and opaque phase(s). This variability of the Stuttgart Formation is primarily attributed to the sandstone sedimentation in a meandering, fluvial environment. The samples are weakly consolidated. Analcime, anhydrite and dolomite are only found as cement phases. SEM micrographs of CO_2-treated samples show corrosion textures on mineral surfaces of anorthitic plagioclase and K-feldspar, as well as euhedral albite crystals. Overall, the data indicate preferred dissolution of calcium-rich plagioclase, K-feldspar and anhydrite, and stabilization or precipitation of albite. The petrophysical properties of the sandstone samples also show slight changes. Nuclear magnetic resonance (NMR) and mercury injection measurements indicate a slightly increased porosity and a shift to larger pore sizes; both suggesting dissolution processes.

Keywords: CO_2-brine-rock interaction; Long-term experiments; In situ P-T conditions of Ketzin reservoir; Saline aquifer; Stuttgart Formation

1. Introduction

Carbon capture and storage (CCS) is a key strategy to reduce anthropogenic CO_2 emissions to the atmosphere. For a successful implementation of the CCS technology, the geological storage of CO_2 in a permanent and safe way is of major importance. The injection of CO_2 into a reservoir will disturb its physico-chemical equilibrium, which is then controlled by acid-generating reactions [1] as CO_2 will dissolve into the brine to form carbonic acid. Subsequent CO_2-brine-rock interactions include the dissolution of certain minerals and the precipitation of others and will not only affect the chemical, but also the physical properties of the reservoir. At least up to now, information on CO_2-induced interactions within the reservoir is indirect and mostly based on gas or fluid samples recovered from

---

*Corresponding author. Tel.: +49-331-288-2837; fax: +49-331-288-1529.
E-mail address: fischer@gfz-potsdam.de (S. Fischer).

observation wells (e.g., [2]). Laboratory experiments at simulated reservoir P-T conditions are an elegant way to overcome the problem of indirect data. Such studies either focus on individual minerals (e.g., [3]) or on whole rock samples (e.g. [4]). In batch CO_2-exposure experiments on Bunter Sandstone at 30 MPa / 60 °C and 63 days run duration, [4] discovered dissolution of dolomite cement and etch textures on K-feldspar and albite; montmorillonite precipitated in cleavages of albite crystals. Due to the vast mineralogical, chemical and physical diversity of the different reservoir formations that may serve as a potential repository and the highly coupled and interacting processes therein, one major result of the so far realized laboratory experiments is that each individual reservoir system has to be investigated separately, and general conclusions are mostly imprecise. In order to add further data to the existing data base and to specifically address the CO_2-induced interactions at the pilot storage site at Ketzin, Brandenburg (Germany) we here present first results of long-term CO_2-exposure experiments on core samples from the Ketzin reservoir rocks (Stuttgart Formation). At the pilot site of Ketzin one injection well (Ktzi 201) and two observation wells (Ktzi 200 and 202) had been drilled into the reservoir to depths between 750 and 800 m. The wells are about 50 and 110 m away from each other and are arranged in a triangular shape [5]. The integrative strategy of the experiments performed on the Ketzin reservoir samples recovered from these wells was to jointly study the mineralogical, chemical, petrophysical as well as microbiological changes of the reservoir rocks as induced by CO_2 on an identical set of samples. The microbiological results are presented in [6] and [7]. In this contribution we focus on the observed mineralogical and petrophysical changes.

2. Materials & Methods

2.1 Sample Description

The studied core samples were recovered from observation well Ktzi 202. Five core sections have been sampled from depths between 627.7 (B2-2) and 634.6 m (B4-2) (Fig. 1). Of these five core sections, a total of 21 individual samples (intact core pieces between 10 to 15 cm in length and 5 cm in diameter, but also cm-sized broken fragments) were split into subsets; subset 1 (untreated) was used to describe the initial mineralogy of the core sections, subset 2 and subset 3 (15 and 21 months of CO_2-treatment, respectively) were recovered from the long-term experiments. Attention was paid to ensure that for each core section the samples for subset 1, 2 and 3 were taken in close proximity to each other to minimize any initial heterogeneity between the samples. Nevertheless, a certain variability between the different samples is apparent in hand specimen (Fig. 1). Most samples are finely laminated on mm- to cm-scale. This lamination predominantly appears as alternating red-brown and dark-brown colors related to different grain sizes (more sandy versus more silty) next to slightly distinct modal quantities of especially clay minerals. Some samples exhibit a fine cross-bedding. Overall, the samples are only weakly consolidated.

2.2 Experimental Procedure

For 15 (21) months the samples of subset 2 (3) were stored together with synthetic reservoir brine and pure CO_2 in high-quality steel pressure vessels at simulated reservoir conditions of 5.5 MPa and 40 °C. The synthetic reservoir brine had an initial composition of 172.8 g/l NaCl, 8.0 g/l $MgCl_2*6H_2O$, 4.8 g/l $CaCl_2*2H_2O$, and 0.6 g/l KCl according to data on the original Ketzin formation fluid available at the start of the experiments [8]. Subsequent studies on the original Ketzin formation fluid showed that the synthetic brine only contains about 81 % of the total dissolved solids (TDS) of the original formation fluid and lacks any sulphate [7]. Therefore, some mineral reactions are expected, which may not be related to CO_2 exclusively.

2.3 Analytical Techniques

After the samples were taken out of the autoclaves they have been washed several times with deionized water and cautiously dried in a compartment drier at 45 °C. A Leitz polarizing microscope was used for thin section analyses and to take micrographs. The grain size of each sample was measured on the average long-axes of 50 grains per sample. X-ray diffraction (XRD) analysis with Rietveld refinement was carried out on Phillips PW1050

diffractometers using Cu-Kα cross radiation. Samples were scanned from 5 to 80 ° 2-Theta with the detector step size set to 0.02 and a rate of 2 sec/step. Electron microprobe (EMP) analyses were performed on a Cameca SX 100. Acceleration voltage was set to15 kV, beam current to 20 nA. A Zeiss ultra 55 plus was used for scanning electron microscopy (SEM). The SEM operated at 20 kV and 15 nA and was equipped with an energy dispersive X-ray system (EDS). Analyses were done on broken sample pieces as well as on polished and gold-coated thin sections to take back-scattered electron (BSE) images. A 2000 WS Porosimeter equipped with a Marco Pore Unit was used to measure mercury injection curves analysed on vacuum-dried samples of approximately 10 g. The injection curves were used to determine the cumulative pore volume, pore throat distribution, bulk density, internal surface area and the mean pore radius. The nuclear magnetic resonance (NMR) relaxation time distributions of the transverse (spin-spin) T_2 relaxation were measured on a Maran Ultra Resonance Instrument with 7 MHz for cores of up to 40 mm in diameter. Simple Carr-Purcell-Meiboom-Gill attenuations of 100 % water-saturated core samples were recorded. For spherical pores the relaxation time of a water-wetted pore is proportional to the pore size via surface relaxivity (50 μm/s used for sandstones [9]) and reflects a distribution of volume to surface of the pores.
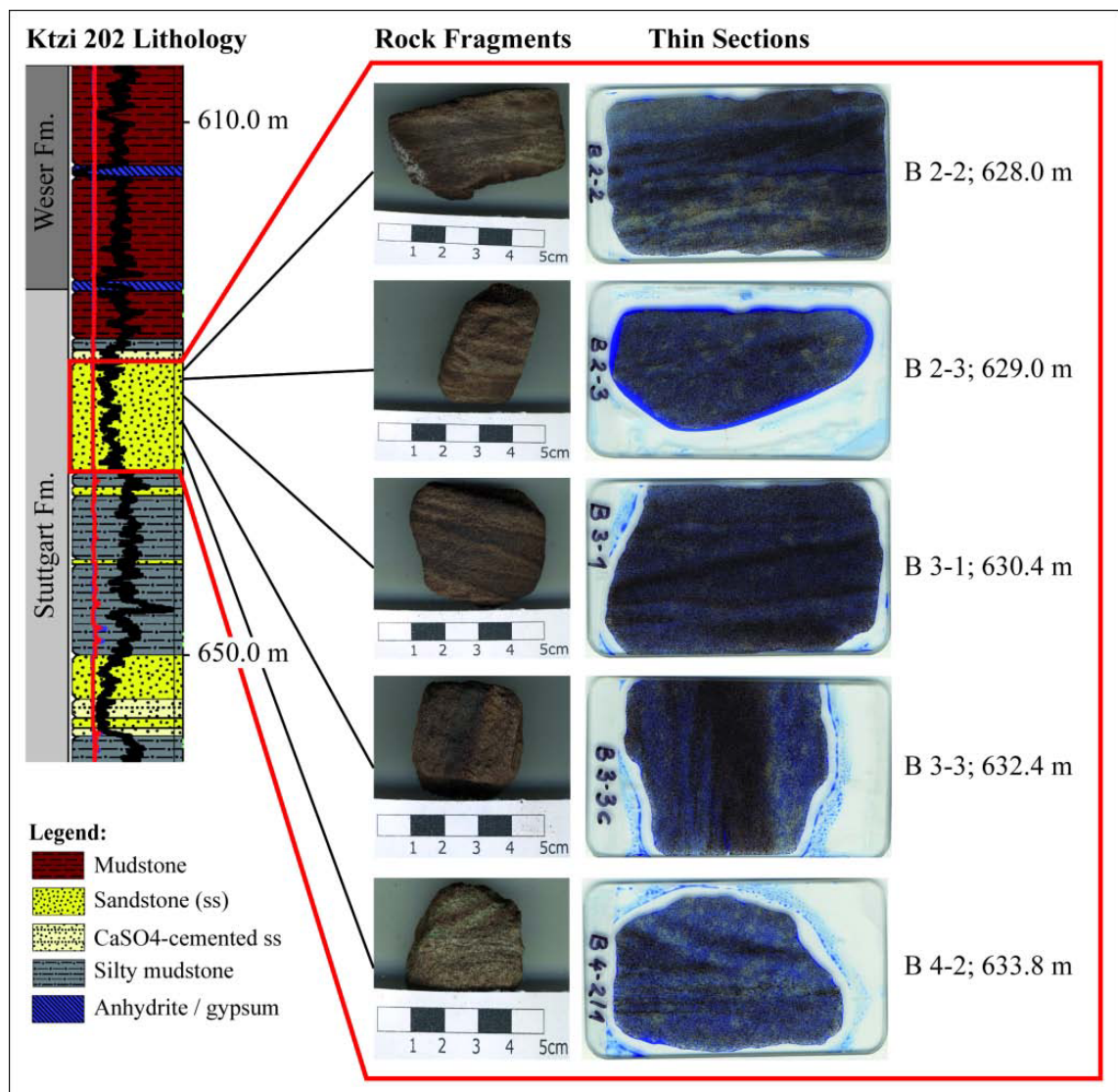

Figure 1 – Profile of the Stuttgart Formation in observation well Ktzi 202, modified after [10]. Shown is the depth interval of the saline aquifer sandstone (ss) next to the positions of the samples. Photographs of the different samples visualize internal heterogeneities on hand-specimen- and thin-section-scale. Blue color on the thin section images is caused by epoxy resin.

3. Results

3.1 Petrography

In thin section, the analyzed samples are mainly fine grained, moderately well- to well sorted, angular to subangular and only partly consolidated sandstones. The principal modal mineral composition as determined by optical microscopy, XRD, EMP and SEM analyses is comparable for all samples. Quartz and plagioclase are the major components, while K-feldspar, mica, clay minerals, hematite, opaque phase(s), and lithoclasts are present subordinately. Mica is predominantly muscovite with only minor amounts of biotite. Chlorite and illite are the most important clay minerals. The lithoclasts are predominantly composed of either quartz and sheet silicates or comprise feldspar with quartz, opaque phase(s), chlorite, and illite. These observations are in good accordance with the results of [10]. The samples are weakly cemented by anhydrite, analcime, and occasionally dolomite. The cements form unevenly distributed, isolated, poikilitic patches (Fig. 2D+E). Anhydrite and analcime are present in all untreated samples. In subset 2, however, anhydrite was not observed in core sections B3-1, B3-3 and B4-2. Analcime does not occur in core section B4-2. Dolomite is only present in both subsets from the uppermost core sections B2-2 and B2-3. Preliminary XRD refinements show that the mineralogical variability between samples of subset 1 is larger than that between untreated and CO_2-treated samples from identical core sections. Consequently, it is reasonable to compare both sets for CO_2-related mineralogical changes.

Heterogeneities are caused by an uneven distribution of minor mineral phases, such as hematite, chlorite, illite, and cement phases. Laminations are related to an alternation of lighter, cement phase-dominated layers to darker, (red-)brownish to black layers, which are mainly composed of opaque phase(s) with notably less cements phases. In close vicinity to the dark layers, mineral grains with thin rims are more frequent. These coatings (cf. Fig. 2D) were already identified as iron(-titanium)-(hydr)oxides [10]; own EMP analyses suggest mostly hematite.
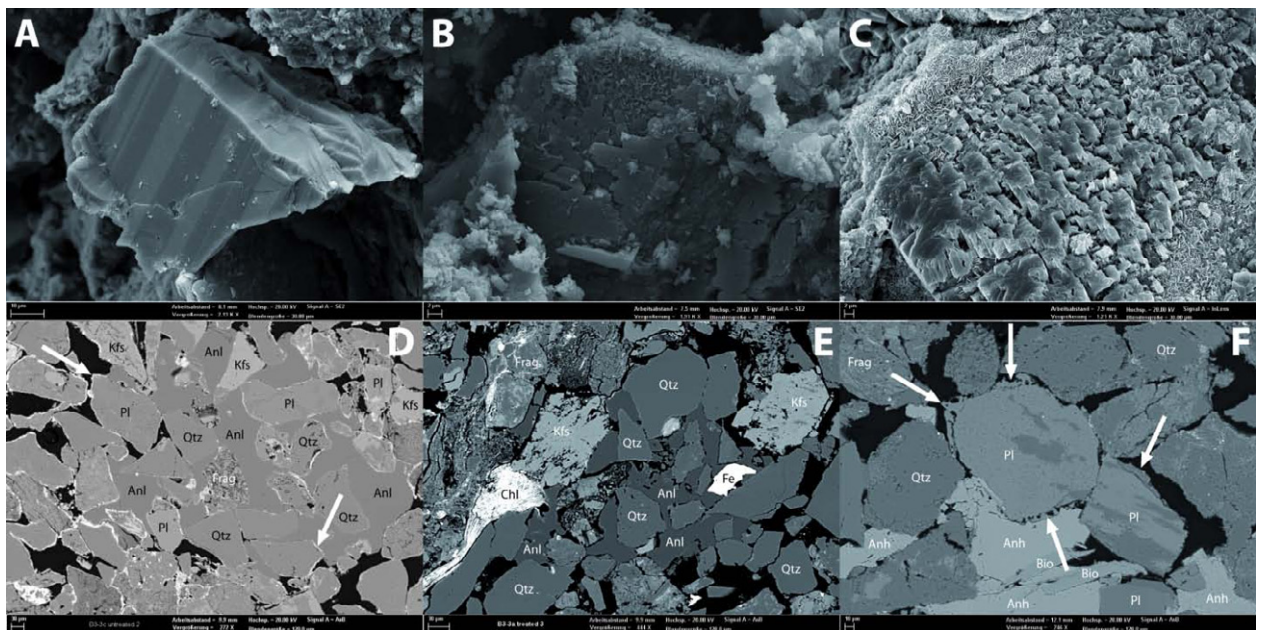

Figure 2 – SEM images of freshly broken fragments (A–C) as well as BSE images on polished thin sections (D–F). A-C represents a consecutive sequence of plagioclase crystals (A=untreated, B=15 months and C=21 months of CO_2 treatment). The nicely laminated plagioclase in A has fresh and unaltered grain surfaces. In B the plagioclase crystal shows first evidence of dissolution and is partly covered by clay minerals. C displays a heavily altered plagioclase crystal with etched pits and totally corroded surfaces.
The BSE images D–F represent a consecutive sample sequence of untreated (D), 15months (E) and 21months (F) of CO_2 treatment, respectively. Labeled are the major mineral phases; black colour represents pore space. D shows patchy occurrence of analcime cement and thin iron coatings of grains (arrows). Minerals do not show any sign of alteration or disaggregation. In E, some grains (e.g. K-feldspar) indicate alteration effects. The arrows in F point to rims around plagioclase grains, which are indicative of alteration.
Abbreviations after [11]; Frag=rock fragments / lithoclasts, Fe=iron-(hydr)oxide.

3.2 Mineral Surfaces

Mineral surfaces of quartz do not show any signs of alteration. Micas show platy morphology with the typical basal cleavage and, like quartz, lack any signs of alteration. Anhydrite typically shows good cleavages in three directions. Despite the fact that anhydrite was not found in three core sections of subset 2 (abovementioned) individual anhydrite crystals do not show any clear evidence of dissolution. Sometimes plagioclase grains do not show any sign of alteration (Fig. 2A), but more typical are surfaces with crystallographically oriented etch textures (Fig. 2B) or advanced dissolution features that result in a disintegrated and irregular surface morphology (Fig. 2C). Comparable dissolution textures are occasionally found in K-feldspar grains. At times, pure albite grains may show clean and fresh euhedral crystal habit [12]. These are only found in the CO_2-treated samples and may have precipitated during the experiments.

3.3 Mineral Compositions

For the feldspars composition no major compositional changes are apparent during the experiments. Plagioclases show two different clusters: intermediate (Ab_{40-80} with $Or_{<10}$) and albite rich compositions ($Ab_{>95}$). K-feldspar consistently ranges from Or_{70} to Or_{98} in both subsets. The very rare occurrence of intermediate alkali feldspar and true ternary feldspars may reflect inaccuracies or measurements of mixed mineral phases. Despite the overall consistency of the feldspar measurements, the plagioclase composition indicates slight changes. Compared to subset 1, much more sodium-rich and pure albite grains occur in subset 2 [12]. Even more, pure albite ($Ab_{>99}$) was only found in CO_2-treated samples. In combination with the petrographical observations (abovementioned), this indicates precipitation of pure albite during the experiments.

As for feldspar, no major compositional changes for sheet silicates between subset 1 and 2 are obvious. White mica is predominantly muscovite; only one analysis showed paragonite. Dark mica is biotite of the phlogopite-annite solid solution series, which may be titanium bearing. In biotite, the XII-fold coordinated A-site is exclusively occupied by potassium. For muscovite, potassium and aluminum contents are slightly lowered during the runs. Biotite analyses from untreated samples occasionally yield very low total oxides of <90 wt%. This might indicate chloritization of biotite. EMP analyses of chlorite show compositions of the clinochlore-chamosite solid solution series.

All three cement phases anhydrite, analcime and dolomite consistently show stoichiometrical compositions before and after the experiments and provide no hints for any chemical alteration. Analcime has near end-member composition and forms comparatively smaller crystals that appear to be very homogenous and optically clear. Dolomite cement has a very uniform composition of calcium and magnesium both approximately accounting for 0.50 pfu. Only traces of iron and manganese were detectable.

3.4 Petrophysics

For subset 1, the porosities range from 19 to 29 % (mercury injection) and from 22 to 33 % (NMR), respectively. Samples from the uppermost part of the sandstone interval are stronger cemented, while samples from the lower most parts are only poorly consolidated. Accordingly, porosities increase from the top to the basal part of the aquifer [10]. The samples have a relatively large proportion of small pores, as can be seen in the pore size distribution diagram of Figure 3. The increased porosities in combination with the inorganic fluid analysis can be transformed into a loss of solid sample material that is in the order of 1 to 2 % [13]. The results of NMR and mercury injection measurements are comparable with expected smaller porosities determined by the latter. NMR data generally indicate a bimodal pore size distribution with a general shift towards larger pores during the experiments. Because the observed porosity increase leads to higher volume values, these results are certainly related to a decrease of the specific surface area due to smaller dissolution processes. Mercury injection measurements indicate a shift towards smaller pore sizes, which may be caused by some salt precipitates on the sample surfaces that caused a plugging of pore throats. The core pieces had to be dried for mercury injection without any flushing with deionised water because of potential disintegration. Therefore, salt precipitation may have occurred during drying.
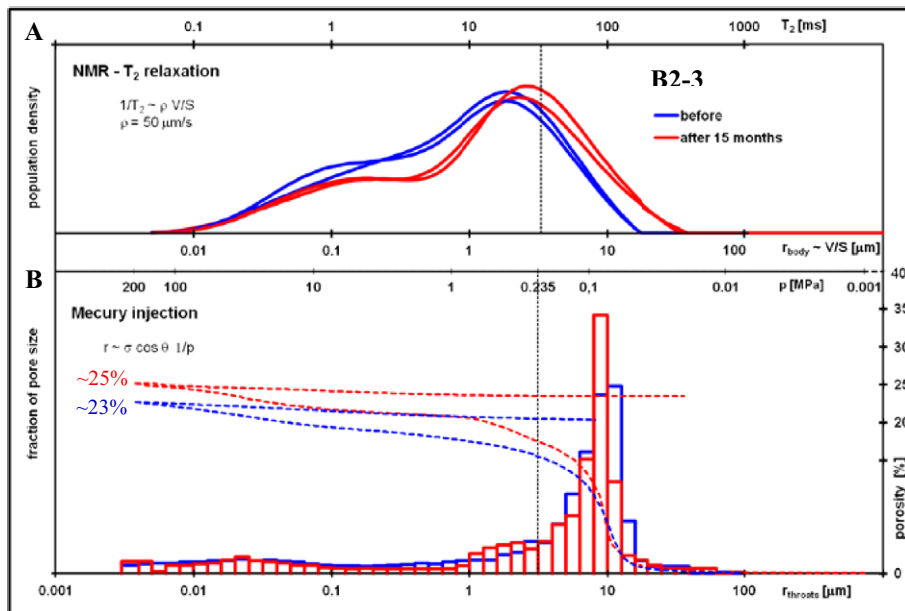
Figure 3 – NMR T$_2$ relaxation (A) and mercury injection (B) measurements exemplarily plotted for the sample B2-3 to determine the pore size distribution. It is apparent that the relaxation time and pressure curves are comparable and both displaying a shift to larger pore sizes. The hatched curves in B show the increase in porosity from ~23% to ~25% during the experiments.

4. Discussion

The applied mineralogical investigations only show minor mineralogical changes related to CO$_2$. The variability between comparable samples before and after the experiments is lower than the overall variability of the studied samples. Several lines of evidence indicate chemical interactions between CO$_2$, brine and sandstone samples. The presence of anhydrite in all samples of subset 1, but its absence in CO$_2$-treated samples from core sections B3-1, B3-3, and B4-2 is indicative of anhydrite dissolution. The distinct corrosion and etch textures on plagioclase and also on K-feldspar surfaces clearly indicate preferred dissolution of these minerals. And taking into account the sequence A-C and the alteration rims in F of Figure 2, dissolution of plagioclase seems to intensify with experimental run duration. On the other hand, euhedral albite grains occurring in CO$_2$-treated samples suggest precipitation of albite [12], most likely in expense of plagioclase. Dissolution of certain minerals is also indicated by a general increase in porosity during the experiments. First data of the synthetic brine composition reveal (amongst others) a distinct increase of calcium and sulfate concentrations [6] that is also suggesting preferred dissolution of anhydrite and of the anorthite component of plagioclase. As the initial concentrations of calcium and sulfate in the synthetic brine were below those of the Ketzin formation fluid (see above) these increased concentrations do not reflect the evolution of the synthetic brine to its potential equilibrium composition. After the experiments, the measured concentrations of, amongst others, calcium and potassium in the fluid are notably higher than those of the original Ketzin formation fluid, which cannot only be explained by the above mentioned attainment of equilibrium without any influence of CO$_2$. Overall, the here presented data in combination with those given by [6] and [7] clearly indicate that the addition of CO$_2$ triggered preferred dissolution of anorthitic plagioclase, K-feldspar as well as anhydrite, and precipitation of albite.

Corrosion effects are observable in SEM micrographs of subset 2, in which plagioclase crystals display heavily altered edges with holes, etched pits and lamellae [12]. These features were not observed – at least not to that extent – in samples of subset 1 and thus suggest intensified alteration processes during the experiments. But as [14] also discussed, it is commonly difficult to quantify alterations of alumosilicates, when pre-experimental, diagenetic alterations of these minerals exist. In contrast to that, fresh and unaltered, euhedral albite grains in some of the CO$_2$-treated samples clearly suggest equilibrium between albite and the brine-CO$_2$ fluid. In combination with the preferred occurrence of pure albite minerals after the CO$_2$-treatment, it is reasonable to assume precipitation of these euhedral albite grains during the experiments. While [14] likewise observed new formed albite minerals during lab-

experiments, [10] already determined albite end-member compositions as a result of diagenetic albitization of both plagioclase and K-feldspar. Accordingly, the higher number of albite measurements in subset 2 is possibly a statistical artifact owed to the natural variability of the reservoir system. Independent of CO_2-exposure lab-experiments, it has been reported that in acidic environments, as well as during hydrothermal plagioclase alteration, feldspar weathering rates are generally higher for calcic plagioclase compared to sodic plagioclase and sodic varieties are more stable (e.g. [15]). Additionally, an increase in the bulk salinity of the fluid stimulates reactions in which alkali earth cations (e.g. calcium) are substituted for alkalis (e.g. sodium) [15].

K-feldspars also seem to be partly dissolved during the CO_2-treatment. Comparable to plagioclase but less frequent, some K-feldspar grains in CO_2-treated samples show corrosion textures. Yet it is hardly possible to differentiate diagenetic and experimental, CO_2-induced alteration processes (abovementioned). Similar alterations of K-feldspar during CO_2-exposure experiments have also been reported by [16].

Although mica minerals do not occur in large quantity, they are an important component of the repository and complete the understanding of the reservoir system behavior. Additionally, alterations of mica minerals could straightforwardly lead to the formation of clay minerals, such as kaolinite, illite, and chlorite. By clogging pore throats these could reduce poroperm levels and in turn hamper the injection of CO_2. [17] presumed that a decrease of permeability due to the formation of clay minerals could be a characteristical feature for CO_2 storage in formations containing alumosilicates. On the other hand, reservoirs rich in feldspars and labile rock fragments, which can react with CO_2 to form new solid carbonate phases, are important for a save and successful long-term storage site. In the here presented study, no unambiguous evidence for such mica alterations or intensified clay mineral formation was found. Only illitization of muscovite could be indicated by the lowered potassium and aluminum contents in muscovite during the runs. Chloritization of biotite – that was described by [10] – might be indicated by the partially very low weight percentages of biotite measurements. Cements are in general a very important feature of reservoir systems because of influencing hydraulical parameters, e.g. injectivity. Despite the suspected dissolution of anhydrite, which was also observed by [17] during comparable core-flooding experiments, no other signs of change in the cement phases could be elaborated. In all samples cement phases are pure anhydrite, pure analcime and pure dolomite.

Porosity measurements of subset 1 agree well with petrophysical and logging data from the other Ketzin wells [18]. The samples have a relatively large proportion of small pores. The porosity increase for subset 2 is consistent with the measured elevated ion concentration. A shift of pore radii to higher values was uniformly observed in the sandstone samples and points to dissolution of minerals (such as anorthite) in response to the CO_2-exposure. Based on our data, the integrity of the reservoir formation at Ketzin is not affected by CO_2.

5. References

[1] Kaszuba, JP, Janecky, DR. Geochemical impacts of sequestering carbon dioxide in brine formations. In: Sundquist, E, McPherson, B, editors. Carbon sequestration and its role in the global carbon cycle. AGU Monograph; 2009, 183: p. 239-248.

[2] Assayag, N, Matter, J, Ader, M, Goldberg, D, and Agrinier, P. Water-rock interactions during a CO_2 injection field-test: implications on host rock dissolution and alteration effects. Chem Geol 2009; 265: 227-235.

[3] Hangx, SJT, Spiers, CJ. Reaction of plagioclase feldspars with CO_2 under hydrothermal conditions. Chem Geol 2009; 265: 88-98.

[4] Wigand, M, Carey, JW, Schütt, H, Spangenberg, E, Erzinger, J. Geochemical effects of CO_2 sequestration in sandstones under simulated in situ conditions of deep saline aquifers. Appl Geochem 2008; 23: 2735-2745.

[5] Schilling, F, Borm, G, Würdemann, H, Möller, F, Kühn, M, and the CO_2SINK Group. Status Report on the First European on-shore CO_2 Storage Site at Ketzin (Germany). Energy Procedia 2009; 1, 1: 2029-2035.

[6] Wandrey, M, Fischer, S, Zemke, K, Liebscher, A, Scherf, AK, Vieth, A, et al.. Monitoring petrophysical, mineralogical, geochemical and microbiological effects of CO_2 exposure – Results of long-term experiments under *in situ* condition. Energy Procedia 2010; this issue.

[7] Wandrey, M, Morozova, D, Zettlitzer, M, Würdemann, H, and the CO_2SINK Group. Assessing drilling mud and technical fluid contamination in reservoir rock and brine samples from the Ketzin storage site using fluorescent dye tracers. Int J Greenhouse Gas Control 2010; in press.

[8] Förster, A, Norden, B, Zinck-Jorgensen, K, Frykman, P, Kuhlenkampff, J, Spangenberg, E, et al.. Baseline characterization of the CO_2SINK geological storage site at Ketzin, Germany. Environ Geosci 2006; 13, 3: 145-161.

[9] Sliikerman, WFJ, Hofman, JP. Determination of surface relaxivity from NMR diffusion measurements. J Magn Reson 1998; 16: 541–544.

[10] Förster, A, Schöner, R, Förster, HJ, Norden, B, Blaschke, AW, Luckert, J, et al.. The Upper Triassic Stuttgart Formation (Middle Keuper) at Ketzin: The reservoir for pilot CO_2 storage in the Northeast German Basin. Mar Pet Geo 2010; doi: 10.1016/j.marpetgeo.2010.07.010.

[11] Kretz, R. Symbols for rock-forming minerals. Am Mineral 1983; 68: 277-279.

[12] Fischer, S, Liebscher, A, Wandrey, M, and the CO_2SINK Group. CO_2-brine-rock interaction – First results of long-term exposure experiments at in situ P-T conditions of the Ketzin CO_2 reservoir. Chemie der Erde / Geochemistry 2010; 70, S3: 155-164.

[13] Zemke, K, Liebscher, A, Wandrey, M, and the CO_2SINK Group. Petrophysical analysis to investigate the effects of carbon dioxide storage in a saline aquifer at Ketzin, Germany (CO_2SINK). Int J Greenhouse Gas Control 2010; doi: 10.1016/j.ijggc.2010.04.008.

[14] Bertier, P, Swennen, R, Laenen, B, Lagrou, D, Dreesen, R. Experimental identification of CO_2-water-rock interactions caused by sequestration of CO_2 in Westphalian and Buntsandstein sandstones of the Campine Basin (NE Belgium). J. Geochem Explor 2006; 89: 10-14.

[15] Deer, WA, Howie, RA, Zussman, J. An introduction to the rock-forming minerals. 2nd ed., London: Prentice Hall; 1992.

[16] Parry, WT, Forster, CB, Evans, JP, Bowen, BB, Chan, MA. Geochemistry of CO_2 sequestration in the Jurassic Navajo Sandstone, Colorado Plateau, Utah. Environ Geosci 2007; 14, 2: 91-109.

[17] Shiraki, R, Dunn, TL. Experimental study on water-rock interactions during CO_2 flooding in the Tensleep Formation, Wyoming, USA. Appl Geochem 2000; 15: 265-279.

[18] Norden, B, Förster, A, Vu-Hoang, D, Marcelis, F, Springer, N, Le Nir, I. Lithological and Petrophysical Core-Log Interpretation in CO_2SINK, the European CO_2 Onshore Research Storage and Verification Project. SPE Asia Pacific Oil and Gas Conference and Exhibition 2008.

4. Publication III:

"Kinetic modeling of laboratory CO_2-exposure experiments performed on whole rock reservoir samples"

Kinetic modeling of laboratory CO_2-exposure experiments performed on whole rock reservoir samples

Sebastian Fischer[a,b], Marco De Lucia[c], and Axel Liebscher[a]

[a]Helmholtz Centre Potsdam, GFZ German Research Centre for Geosciences, Centre for Geological Storage, Telegrafenberg, D-14473 Potsdam, Germany

[b]Berlin Institute of Technology, School VI, Department of Applied Geosciences, Chair of Mineralogy-Petrology, Ackerstraße 76, D-13355 Berlin, Germany

[c]Helmholtz Centre Potsdam, GFZ German Research Centre for Geosciences, Section 5.3 - Hydrogeology, Telegrafenberg, D-14473 Potsdam, Germany

Abstract

Mineralogical and geochemical observations from laboratory CO_2-exposure experiments on reservoir rocks are compared with predictions from geochemical modeling that were performed using PHREEQC software. The Pitzer-based Eq 3/6 thermodynamic database provided by Quintessa Ltd. was used. For kinetic modeling Lasaga-type rate equations were implemented and different models were parameterized taking kinetic rate law parameters from Palandri and Kharaka (2004). Specific reactive surface areas were calculated based on specific geometric surface areas assuming grain diameters of 20 μm and 200 μm for clay and non-clay minerals, respectively. Scaling and roughness factors were introduced to account for mineral accessibility.

Equilibrium models show albite, anhydrite, dolomite and illite as the most reactive minerals reproducing the measured brine ion concentrations within acceptable precision. Following first kinetic test runs indicating oversaturation of albite, K-feldspar and illite, different models that include or exclude precipitation of the three minerals were set up to find the most suitable model and to analyze the effects of different scenarios. The best match with experimentally measured ion concentrations was obtained by the model suppressing any mineral precipitation. This observation is in agreement with the findings from the laboratory experiments, in which no new formed minerals were detected.

Keywords: PHREEQC; comparison of experimental and modeling results; best match; impacts of including/precluding precipitation.

1. Introduction

Laboratory autoclave experiments on whole rock samples from the reservoir of the Ketzin pilot CO_2 storage site, Germany, have been performed in order to evaluate effects of site-specific CO_2brine-rock reactions (Fischer et al., 2010; Fischer et al., submitted). Target reservoir is the Triassic

Stuttgart Formation – a weakly cemented, siliciclastic saline aquifer located at approximately 630 m depth. Initial sandstone samples are composed of 24.1 to 41.4 wt% quartz, 16.8 to 35.1 wt% plagioclase, 10.1 to 29.2 wt% illite+muscovite, 5.5 to 12.5 wt% K-feldspar, 0.8 to 4.7 wt% chlorite+biotite, and 0.7 to 4.5 wt% hematite. Analcime (0 to 11.6 wt%), anhydrite (0 to 36.7 wt%) and dolomite (0 to 3.0 wt%) occur as pore filling cement phases. The synthetic brine was prepared by dissolving 229.81 g NaCl, 8.54 g $MgSO_4 \cdot 7H_2O$, 5.79 g $CaCl_2$, 0.54 g KCl and 0.03 g $FeCl_3 \cdot 6H_2O$ in one liter deionized water. For 40 months, rock samples were stored in autoclave reactors together with the synthetic brine and pure CO_2 at 40 °C and 5 MPa. During evaluation of the batch experiments it turned out to be difficult to distinguish natural, lithologic variability from CO_2-induced changes. Dissolution of calcic plagioclase, anhydrite and K-feldspar were observed, but no mineral precipitates were detected during the experiments; possibly because too little new material formed (Fischer et al., 2010; Fischer et al., submitted).

Complementary to the laboratory experiments reactive geochemical modeling was conducted. For a simulation period of 24 months, different models were set up and run to (i) try to match the experimental observations, (ii) compare and directly validate theoretical models against experimental observations, and (iii) evaluate the effect of including/precluding precipitation for certain, potentially supersaturated minerals during modeling.

2. Modeling approach

The speciation software PHREEQC (Parkhurst and Appelo, 1999) was used for equilibrium as well as kinetic modeling. The investigation of highly saline systems (Ketzin reservoir brine TDS > 230 g/L) requires a thermodynamic database and corresponding activity model capable of handling such elevated ionic strengths. The Pitzer-based Eq3/6 database (Wolerly, 1992), transformed into PHREEQC format by Quintessa Ltd. (Benbow et al., 2008) – hereafter referred to as Quintessa database –includes relevant Al and Si species, thus allowing modeling of alumosilicate mineral reactions, and was retained for this study. For more details see De Lucia et al. (2012). The models were scaled to the amount of water present in the autoclave reactors. The composition of the initial synthetic brine is as follows: Na^+=3.9e-1 mol, K^+=1.3e-3 mol, Ca^{2+}=4.2e-3 mol, Mg^{2+}=5.0e-3 mol, Cl^- =4.1e-1 mol, and SO_4^{2-}=8.7e-4 mol.

First, an equilibrium model (**Model_A**) is calculated to analyze CO_2-independent reactions by equilibrating the experimentally used synthetic brine and mineral assemblage as quantified by XRD analysis (see above). While the pH of 7 for the synthetic brine was chosen according to analysis of formation fluids from the Ketzin reservoir (Wuerdemann et al., 2010), the redox potential has been determined iteratively. Solid solution minerals are studied as end-member phases, so that anorthite and albite are hence introduced for plagioclase with each accounting for half the quantity of total plagioclase. Furthermore, chamosite-7A is used for chlorite, and illite_IMt-2 (adapted from Gailhanou et al., 2007) for illite. Chamosite-7A is chosen as iron-rich member of the chlorite group, and illite_IMt-2 shows best results during both XRD Rietveld refinements, and first kinetic test runs. Thermodynamic constants for chamosite-7A have been derived from the LLNL database. Chamosite-7A and illite_IMt-2 are hereafter referred to as chamosite and illite, respectively. The following mineral quantities are initially considered in **Model_A**: 0.285 mol albite, 0.13 mol analcime, 0.03 mol anhydrite, 0.285 mol anorthite, 0.03 mol chamosite, 0.03 mol dolomite, 0.08 mol hematite, 0.23 mol illite, 0.16 mol K-feldspar and 3.15 mol quartz.

Next, a second equilibrium model (**Model_B**) including the initial synthetic brine, the mineral assemblage and CO_2 is calculated in order to reproduce the experimentally obtained brine ion concentrations and to iteratively identify most reactive (i.e. primary) minerals. In **Model_B**, each mineral phase is equilibrated with the synthetic brine and CO_2, which is introduced as an equilibrium

gas phase with a pressure (P=5.5 MPa) and salinity (ionic strength=3.6) corrected solubility (log fugacity 1.6).

During kinetic modeling, Lasaga-type rate laws for mineral dissolution-precipitation reactions are applied. Temperature and pH dependencies of fluid-mineral reactions are fully implemented by an Arrhenius type equation that accounts for reaction mechanisms in neutral, acid and base environments. Rate law parameters are taken from Palandri and Kharaka (2004); auxiliary calculations show that the term for the base mechanism (i.e. reactions in alkaline conditions) is orders of magnitude smaller than that of the neutral and acid mechanisms under high CO_2 partial pressures and is therefore excluded from further computation. Parameters for illite are set to those of smectite. Specific reactive surface areas are calculated based on specific geometric surface areas, which are a function of mineral density and average grain diameter. Under the assumption of spherical geometry, grain diameters are 20 and 200 μm for clay (here chamosite and illite) and non-clay minerals, respectively. A scaling factor of 0.001 and a surface roughness factor of 10 are additionally included to account for mineral accessibility. Because no kinetic data is available for analcime, and quartz is assumed to be inert, both phases are excluded from the kinetic calculations. Having reaction rates several orders of magnitude quicker than the other minerals present in the Stuttgart Formation, anhydrite and dolomite are both defined as equilibrium phases. Hence, albite, anorthite, chamosite, hematite, illite and K-feldspar are reacted with synthetic brine and CO_2 during kinetic simulations.

Because no new formed mineral was detected during laboratory experiments, first kinetic simulations (**Model_C**) only considered dissolution, and suppressed precipitation. As described later in the text, albite, illite and K-feldspar (amongst others) are supersaturated in the brine of **Model_C**. Hence, it was reasonable to script three successive models allowing precipitation of albite (**Model_D1**), simultaneous precipitation of albite and illite (**Model_D-2**), and simultaneous precipitation of albite, illite and K-feldspar (**Model_D-3**), respectively. Precipitation rates are set equal to those of dissolution using the same kinetic rate expression as for dissolution. The only difference is that the reactive surface area is proportional to the amount of mineral present during dissolution, but constant during precipitation (see also, e.g., Gaus et al., 2005).

3. Results

Model_A reveals that albite, anhydrite, hematite and illite would precipitate, and the remainder minerals would dissolve to attain total equilibrium between synthetic brine and mineral assemblage (Table 1). While analcime and chamosite are completely dissolved and still undersaturated (SI<0) at the end of the simulation, substantial dissolution of quartz (-0.92 moles) and anorthite (-0.20 mol) are the major effects of equilibration. Most significant changes in brine ion composition are increased Ca^{2+} (+0.21 moles) and decreased Na^+ (-0.39 moles) concentrations. Ionic strength increases from 3.62 to 5.34 and pH drops from 7 to 5.65.

Albite, anhydrite, dolomite and illite are identified as primary minerals in **Model_B**. After addition of gaseous CO_2, a fairly good match between modeled and experimentally determined ion brine concentrations is achieved through precipitation of albite, and dissolution of anhydrite, dolomite and illite. At the end of the simulation, only K-feldspar (SI=0.2) and kaolinite (SI=4.7) are supersaturated. Ionic strength increases from 3.62 to 3.76, and pH drops from 7 to 4.36 (Table 1).

Model_C shows a good match between experimentally observed and modeled brine ion concentrations with time. Most significant changes generally occur within the first four months after CO_2 addition. From this moment forth all ions (Na^+, K^+, Ca^{2+}, Mg^{2+}, Fe^{2+}, Al^{3+}, Si^{4+}, Cl^-, SO_4^{2-}) as well as key parameters (ionic strength and pH) are constant to the end. Ionic strength increases from 3.62 to 3.77, and pH drops from 7 to 4.38 (Table 1). From the kinetically modeled minerals, albite (SI=6.8),

illite (SI=7.9) and K-feldspar (SI=7.0) are supersaturated at the end. It is furthermore noteworthy that analcime (SI=4.8), kaolinite (SI=10.6) and quartz (SI=1.8) are also supersaturated. While 0.45 g of anhydrite and 0.16 g anorthite dissolve during the simulation, the other implemented minerals are virtually unaffected.

Table 1 – Comparison of key parameters as determined from the distinct models.

		INPUT VALUES	MODEL_A	MODEL_C	MODEL_D1	MODEL_D2	MODEL_D3
Mineral Abundance [moles]	**Albite**	0.285	0.80	0.285	0.2894	0.2891	0.2883
	Analcime	0.13	0.00	n.d.			
	Anhydrite	0.03	0.03	0.03	0.03	0.03	0.03
	Anorthite	0.285	0.08	0.284	0.284	0.279	0.278
	Chamosite	0.03	0.00	0.03	0.03	0.03	0.03
	Dolomite	0.03	0.0221	0.0299	0.0349	0.0348	0.0348
	Hematite	0.08	0.10	0.08	0.08	0.08	0.08
	Illite	0.23	0.28	0.23	0.23	0.23	0.23
	K-feldspar	0.16	0.12	0.16	0.16	0.16	0.16
	Quartz	3.15	2.23	n.d.			
Ion Concentration [moles]	**Na$^+$**	0.395	0.001	0.395	0.391	0.391	0.392
	K$^+$	0.001	0.000002	0.001	0.001	0.001	0.0002
	Ca^{2+}	0.004	0.2	0.008	0.009	0.009	0.009
	Fe^{2+}	b.d.l.	1.94E-09	0.000005	0.000005	4.72E-14	2.91E-12
	Mg^{2+}	0.005	0.0000003	0.005	0.0001	0.0002	0.0002
	Al^{3+}	b.d.l.	0.0000005	0.001	0.009	0.008	0.008
	Si^{4+}	b.d.l.	0.00001	0.001	0.000002	0.000003	0.000003
	Cl$^-$	0.414	0.414	0.414	0.414	0.413	0.414
	SO$_4^{2-}$	0.001	0.001	0.004	0.004	0.004	0.004
Saturation Index (SI) [a]	**Albite**	n.d.	0	6.8	1.0	1.1	1.0
	Analcime		-0.2	4.8	1.6	1.5	1.6
	Aragonite		0	-0.7	0.2	0.1	0.2
	Calcite		0	-0.6	0.3	0.2	0.3
	Chamosite		-9.5	-5.7	-3.1	-19.7	-16.0
	Goethite		-0.5	-1.0	0.2	-8.0	-6.2
	Hematite		0	-1.0	1.4	-15.0	-11.4
	Illite		0	7.9	3.2	0.1	0.1
	K-feldspar		0	7.0	1.2	1.3	0.3
	Kaolinite		6.7	10.6	9.0	8.8	9.0
pH			5.65	4.38	4.82	4.75	4.82
Ionic Strength			5.34	3.77	3.89	3.87	3.89

b.d.l. = below detection limit
n.d. = not determined in the respective model
[a] *Only SI of those minerals listed that reveal supersaturation in any of the six models.*
Note: MODEL_B is not listed because this simulation was not based on the input values as shown in Tab. 1.

By allowing albite to precipitate, **Model_D-1** shows a good match between experimentally determined and modeled brine concentrations for most ions, but significant mismatches for Al^{3+}, Mg^{2+} and Fe^{2+} concentrations. In comparison to **Model_C,** main differences are precipitating albite (+4.4e-3 mol) and dolomite (+4.9e-3 g), and dissolution of -6.6e-3 mol anorthite and -3.4e-3 mol anhydrite (Table 1). Aluminum as well as Fe^{2+} brine concentrations continuously increase to finally attain 8.8e-3 and 5.0e-6 mol. Magnesium increases to a maximum brine concentration of 5.8e-3 mol after one month of CO₂ exposure, and decreases to 1.3e-4 mol from then forth to the end of the simulation.

While albite (SI=1.0), illite (SI=3.2) and K-feldspar (SI=1.2) are supersaturated to a lesser extent compared to **Model_C**, analcime (SI=1.6) and kaolinite (SI=9.0), but now also aragonite (SI=0.2), calcite (SI=0.3), goethite (SI=0.2) and hematite (SI=1.4) are supersaturated. The latter four minerals are undersaturated at the start, but change to supersaturation at the end of the simulation. Ionic strength increases from 3.62 to 3.76 within the first month and to 3.89 from than forth to the end. The pH drops sharply from 7 to 4.37 after CO_2 addition, and then increases slowly but continuously to 4.82 at the end.

In due consideration of albite and illite precipitation, **Model_D-2** also reveals a good match between experimentally determined and modeled brine concentrations for most ions, but still significant mismatches for Al^{3+}, Mg^{2+} and Fe^{2+} concentrations. 1.3e-5 mol illite, 4.1e-3 mol albite and 4.8e-3 mol dolomite precipitate, and -6.2e-3 mol anorthite and 3.4e-3 mol anhydrite dissolve (Table 1). Most ion concentrations are congruent compared to those determined in **Model_D-1**, significant differences are lower Fe^{2+} (4.7e-14 mol) and K^+ concentrations (1.3e-3 mol). While albite (SI=1.1), illite (SI=0.1), K-feldspar (SI=1.3), analcime (SI=1.5), aragonite (SI=0.1) and calcite (SI=0.2) are slightly supersaturated, kaolinite (SI=8.8) is strongly supersaturated at the end of the simulation. It is noteworthy that chamosite (SI=-19.7), goethite (SI=-8.0) and hematite (SI=-11.4) turn extremely undersaturated. Ionic strength and pH show identical evolutions with time compared to **Model_D-1**.

Model_D-3, which includes precipitation of albite, illite and K-feldspar, is generally similar to **Model_D-2** revealing, e.g., identical evolutions of pH, ionic strength as well as anhydrite and dolomite concentrations. Largest differences compared to the previous model are precipitation of 1.1e-3 mol K-feldspar, a little less precipitation of albite (3.3e-3 mol) and enhanced dissolution of anorthite (-6.6e-3 mol). Again 1.4e-5 mol illite precipitates. Potassium brine concentration decreased by $^1/_8^{th}$ to 1.7e-4 mol at the end of the simulation, when albite (SI=1.0), analcime (SI=1.6), aragonite (SI=0.2), calcite (SI=0.3), illite (SI=0.1) and K-feldspar (SI=0.3) are slightly, and kaolinite (SI=9.0) is strongly supersaturated (Table 1).

4. DISCUSSION

In **Model_A**, equilibration of the synthetic brine used in the laboratory experiments with the mineral assemblage as determined by XRD analysis clearly shows that the synthetic brine triggers chemical reactions that are not caused by CO_2 exposure. Hence, dissolution of analcime, anorthite, chamosite, dolomite, K-feldspar and quartz, as well as precipitation of albite, anhydrite, hematite and illite with subsequent changes in respective brine ion concentrations can be expected to be caused – at least to a certain degree – by simple brine-rock equilibration, and not only by CO_2. **Model_A** would generate a less strong pH drop, but a higher ionic strength compared to kinetic simulations. The pH drop signifies inaccuracy of pH determination during the pump test, and a pH between 5 and 5.5 can be expected to better represent in situ reservoir brine conditions.

By yielding a fairly good match with the experimentally determined brine ion concentrations in **Model_B**, precipitating albite, and dissolving anhydrite, dolomite and illite are the most reactive minerals. Despite intense dissolution of dolomite (-5.9e-2 mol), the pH drops to 4.36 and is therewith, as is the modeled ionic strength, very similar in comparison to subsequent kinetic simulations.

Results of **Model_C** indicate potential clay mineral formation as kaolinite and illite reveal strongest supersaturation. Albite, analcime, K-feldspar and quartz are also supersaturated, but because analcime and quartz were excluded from kinetic modeling, and kaolinite has not been detected in any sample analyzed prior to or after the experiments, the latter three phases are not further investigated as potential precipitates. Note that dissolution of anhydrite and anorthite are also detected during the experiments (Fischer et al., 2010; Fischer et al., submitted).

Precipitation of albite and dolomite in **Model_D1** leads to significantly reduced supersaturation of albite, analcime, illite, K-feldspar and kaolinite, and cause Mg^{2+} as well as Na^+ brine ion concentrations to decrease. The continuous increase of Al^{3+} brine ion concentrations throughout the simulation is related to enhanced anorthite dissolution; a process that is possibly overrated. Given the good match of Mg^{2+} concentrations in **Model_C** and the lack of hints of dissolution of dolomite during laboratory experiments, but also given the comparatively low pH of about 4.5, the predicted formation of dolomite is rather questionable. The increase of Fe^{2+} concentrations is related to dissolution of minor fractions of chamosite and hematite. Note that illite is supersaturated. Both minerals reveal increasing saturation indexes and hematite finally changes to supersaturation.

Model_D2 shows that after precipitation of 1.3e-5 mol illite and thereby lowered K^+ and Fe^{2+} brine concentrations, illite is finally very close to equilibrium (SI=0.1), and chamosite, goethite and hematite turn extremely undersaturated. Note that the mismatch between measured and modeled K^+ and Fe^{2+} brine concentrations is further increased.

Due to precipitation of 1.1e-3 mol, K-feldspar is close to equilibrium (SI=0.3) at the end of **Model_D3**. Through decreased K^+ brine concentrations, and similar Mg^{2+}, Fe^{2+} and Al^{3+} brine concentrations compared to the previous simulation, **Model_D3** results in a larger mismatch with the measured ion concentrations. K-feldspar precipitation has generally little effect on the saturation state and abundance of other minerals.

5. CONCLUSIONS

At least to some extent brine-rock reactions are not related to CO₂ exposure, but triggered by the composition of the synthetic brine and respective equilibration of the synthetic brine with the reservoir rock. Comparison of the different kinetic models reveals that the best match with experimental observations is yielded by the model that suppresses any mineral precipitation. This result is in line with the experimental observations that did not reveal any new formed mineral precipitates. Nonetheless it became apparent that the described models do not completely cover the chemical system of the laboratory experiments. This is related to an incomplete data set, on the one hand, but also to the complex experimental test matrix (whole rock samples, brine composition), on the other. The presented study showed that simplified simulations are capable of identifying key mineral phases and fundamental processes under the respective assumptions, but also that the models do not provide all possible contingencies. Future work will include the compilation of more structured and complex models also with regard to, e.g., precipitation of kaolinite.

REFERENCES

Benbow, S., Metcalfe, R., Wilson, J., 2008: Pitzer databases for use in thermodynamic modeling. Quintessa Technical Memorandum (unpublished).

De Lucia, M.; Bauer, S.; Beyer, C.; Kuehn, M.; Nowak, T.; Pudlo, D.; Reitenbach, V.; Stadler, S., 2012: Modelling CO₂-induced fluid-rock interactions in the Altensalzwedel gas reservoir. Part I: from experimental data to a reference geochemical model. Environmental Earth Sciences, 67, 2, 563-572.

Fischer, S., Liebscher, A., Wandrey, M., 2010: CO₂-brine-rock interaction – First results of long-term exposure experiments at in situ P-T conditions of the Ketzin CO₂ reservoir. Chemie der Erde/Geochemistry 70, 3, 155-164.

Fischer, S., Liebscher, A., De Lucia, M., Hecht, M.: Reactivity of sandstone and siltstone samples from the Ketzin pilot CO₂ storage site – Laboratory experiments and reactive geochemical modeling. Submitted to Environmental Earth Sciences, Springer.

Gailhanou, H., van Miltenburg, J., Rogez, J., Olives, J., Amouric, M., Gaucher, E., Blanc, P., 2007: Thermodynamic properties of anhydrous smectite mx-80, illite imt-2 and mixed-layer illite smectite

iscz-1 as determined by calorimetric methods. part I: Heat capacities, heat contents and entropies. Geochim Cosmochim Acta 71, 22, 5463-5473.

Gaus, I., Azaroual, M., Czernichowski-Lauriol, I., 2005: Reactive transport modelling of the impact of CO_2 injection on the clayey cap rock at Sleipner (North Sea). Chem Geol, 217, 319–337.

Palandri, J.L., Kharaka, Y.K., 2004: A compilation of rate parameters of water-mineral interaction kinetics for application to geochemical modeling. US Geol Survey Water-Resources Investigations, Open File Report 2004–1068.

Parkhurst, D.L., Appelo, C.A.J., 1999: User's guide to PHREEQC (version 2)-A computer program for speciation, batch-reaction, one-dimensional transport, and inverse geochemical calculations. U.S. Geological Survey Water-Resources Investigations Report 99–4259.

Wolery, T., 1992: Eq3/6, a software package for geochemical modeling of aqueous systems: Package overview and installation guide (version 7.0) ucrl-ma-110662. Technical Report, Lawrence Livermore National Laboratory.

Wuerdemann, H., Moeller, F., Kuehn, M., Heidug, W., Christensen, N.P., Borm, G., Schilling, F.R., CO_2Sink Group, 2010: CO₂SINK-From site characterisation and risk assessment to monitoring and verification: One year of operational experience with the field laboratory for CO_2 storage at Ketzin, Germany. Int J Greenh Gas Control 4, 938–951.

5. Publication IV:

"Reactivity of sandstone and siltstone samples from the Ketzin pilot CO₂ storage site – Laboratory experiments and reactive geochemical modeling"

SPECIAL ISSUE

Reactivity of sandstone and siltstone samples from the Ketzin pilot CO₂ storage site-Laboratory experiments and reactive geochemical modeling

Sebastian Fischer · Axel Liebscher · Marco De Lucia · Lutz Hecht · and the Ketzin Team

Abstract To evaluate mineralogical-geochemical changes within the reservoir of the Ketzin pilot CO₂ storage site in Brandenburg, Germany, two sets of laboratory experiments on sandstone and siltstone samples from the Stuttgart Formation have been performed. Samples were exposed to synthetic brine and pure CO₂ at experimental conditions and run durations of 5.5 MPa/40 °C/40 months for sandstone and 7.5 MPa/40 °C/6 months for siltstone samples, respectively. Mineralogical changes in both sets of experiments are generally minor making it difficult to differentiate natural variability of the whole rock samples from CO₂-induced alterations. Results of sandstone experiments suggest dissolution of the anorthite component of plagioclase, anhydrite, K-feldspar, analcime, hematite and chlorite + biotite. Dissolution of the anorthite component of plagioclase, anhydrite and K-feldspars is also observed in siltstone experiments. In an inverse modeling approach, an extensive set of equilibrium simulations was set up in order to reproduce the experimental observations of the sandstone experiments. Simulations generally show fairly good matches with the experimental observations. Best matches with measured brine data are obtained from mineral combinations of albite, analcime, anhydrite, dolomite, hematite, illite, and kaolinite. The major discrepancies during equilibrium modeling, however, are reactions involving Fe²⁺ and Al³⁺. The best matching subsets of the equilibrium models were finally run including kinetic rate laws. These simulations reveal that experimentally determined brine data was well matched, but reactions involving K⁺ and Fe²⁺ are not fully covered. The modeling results identified key primary minerals as well as key chemical processes, but also showed that the models are not capable of covering all possible contingencies.

Keywords Laboratory experiments · Sandstone and siltstone reactivity · Geochemical modeling · CO₂ storage · Ketzin pilot site

S. Fischer (✉) · A. Liebscher · M. De Lucia
Helmholtz Centre Potsdam, GFZ German Research Centre for Geosciences, Telegrafenberg, 14473 Potsdam, Germany
e-mail: fischer@gfz-potsdam.de

S. Fischer
Berlin Institute of Technology, Chair of Mineralogy–Petrology, Department of Applied Geosciences, School VI, Ackerstrasse 76, 13355 Berlin, Germany

L. Hecht
Museum für Naturkunde, Leibniz Institute for Research on Evolution and Biodiversity at the Humboldt University Berlin, Invalidenstrasse 43, 10115 Berlin, Germany

Introduction

Geological storage of carbon dioxide (CO₂) in deep saline aquifers is considered to be one of the key options for reducing anthropogenic CO₂ emissions and to stabilize atmospheric CO₂ levels in order to mitigate global warming without drastically changing our energy-producing technologies (e.g. Gunter et al. 1993; Bachu et al. 1994; IPCC 2005; Michael et al. 2010). When CO₂ is injected into an aquifer it will partially dissolve into the formation brine to form carbonic acid. So, introducing CO₂ into a siliciclastic aquifer system will trigger a complex set of chemical reactions between injected CO₂, formation brine and reservoir and cap rocks (e.g. Holloway 1997; Hitchon et al. 1999; Watson et al. 2002; Rochelle et al. 2004; Moore et al. 2005; Czernichowski-Lauriol et al. 2006; Gaus 2010), which again may have major impact on the mineral assemblage and thermodynamic equilibrium. Dissolution

🖄 Springer

of primary minerals (e.g. silicates) or precipitation of secondary minerals (e.g. carbonates) may occur, which in turn affect petrophysical properties such as permeability, porosity or injectivity. For a safe long-term underground storage it is necessary to understand these complexly coupled physico–chemical processes within reservoir and cap rocks to not only assess their impact on reservoir system integrity (Wiese et al. submitted) but also to better understand the complex suite of chemical reservoir processes and the evolution as well as the movement of the CO_2 plume within the reservoir (cf. Kempka and Kühn 2013). Several laboratory autoclave experiments (e.g. Sass et al. 1999; Rochelle et al. 2002; Kaszuba et al. 2003, 2005; Rosenbauer et al. 2005; Bateman et al. 2005; Wigand et al. 2008; Smyth et al. 2009; Rosenqvist et al. 2012) investigated the effects of CO_2 on chemical and/or petrophysical properties of different reservoir rocks. One major finding was that each reservoir has to be studied separately, because CO_2 reactivity is highly reservoir-specific and generalized predictions are inadequate; a consequence of the high variability in reservoir brine composition and pH, in situ pressures, and temperatures as well as chemical complexity of reservoir rocks (e.g. Holloway 1997).

In this study, we present results from laboratory autoclave experiments as well as reactive geochemical modeling on CO_2-brine-rock interactions performed on sandstone and siltstone samples from the Ketzin pilot site. The Ketzin pilot site in Brandenburg, Germany, was the first European onshore test site for the geological storage of CO_2 in a saline aquifer. About 65,000 t of CO_2 have been injected into the siliciclastic Stuttgart Formation, since June 2008 (Martens et al. 2012, 2013). The site represents an example of CO_2 injection into an anticlinal structure below a low-permeability cap rock (Förster et al. 2006). The Upper Triassic Stuttgart Formation was deposited in a fluvial environment and is highly heterogeneous both vertically and laterally with sandstone channel facies rocks of good reservoir quality alternating with muddy flood plain facies rocks of poor reservoir quality (Förster et al. 2006). It is located at depths between 630 and 710 m and the initial temperature was about 38 °C (Prevedel et al. 2008).

Materials and methods

Sample description

At the Ketzin site, one injection well (Ktzi 201) and three observation wells (Ktzi 200, 202, 203) have been drilled to depths between 700 and 800 m (Prevedel et al. 2008; Martens et al. 2013). The seven samples used in this study were recovered from observation well Ktzi 202 from the depth interval 625.8 m to 634.0 m (Fig. 1) and are labeled B1-2 (625.8–626.0 m), B2-1 (627.0–627.2 m), B2-2 (627.7–627.9), B2-3 (628.4–628.6 m), B3-1 (629.6–630.0 m), B3-3 (631.2–632.2 m), and B4-2 (633.5–633.7 m). Sample B1-2 is a siltstone from directly above the CO_2 sandstone reservoir and represents the transition to the overlaying cap rocks of the Weser and Arnstadt Formations. Samples B2-1 to B4-2 represent typical reservoir sandstones of the Ketzin site. In hand specimens, all samples are finely laminated on mm- to cm-scale with occasional fine cross-bedding textures. They are only weakly consolidated with an uneven distribution of cement phases within isolated, poikilitic patches. The uppermost sandstone samples B2-1 and B2-2 reveal strongest cementation that tendentially decreases with depth.

Experimental procedure

From the sandstone experiments, a total of 35 individual sub-samples were analyzed. Untreated sub-samples were used for baseline characterization. CO_2-treated sub-samples were taken after 15, 21, 24, and 40 months run time (Table 1), respectively. For CO_2 treatment, at least four sub-samples from each sample were placed in a common autoclave, filled with synthetic brine and pressurized with ≥99.9 vol% pure CO_2. The synthetic brine was prepared based on fluid data available at the start of the experiments. As described in Fischer et al. (2010) subsequent studies revealed that the synthetic brine only contained about 80 % of total dissolved solids (TDS). Consequently, due to the use of this synthetic brine some re-equilibration reactions with the rock core material were expected independent of CO_2. Run conditions were 5.5 MPa/40 °C. Results from

Fig. 1 Part of the well-logging profile from observation well Ktzi 202 signifying lithological units and depths of siltstone and sandstone samples, respectively. Modified after Förster et al. (2010)
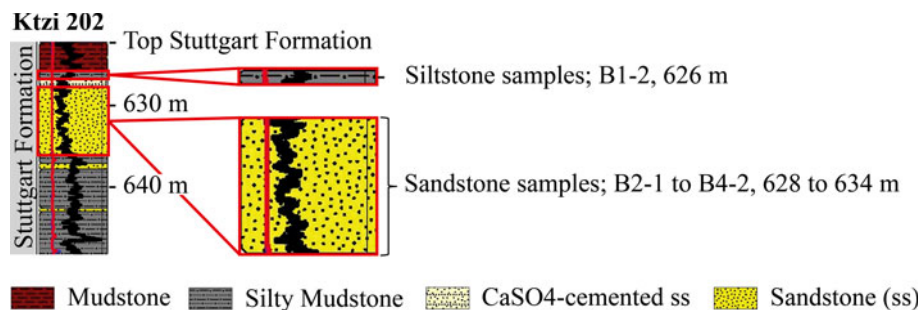
Table 1 Modal composition (wt%) of sandstones as determined by XRD

Sample no.	B2-1					B2-2					B2-3				
Depth (m)	627.5–627.7					627.7–627.9					628.4–628.6				
Run duration (months)	0	15	21	24	40	0	15	21	24	40	0	15	21	24	40
Number of individual samples per set	1	1	1	1	1	1	1	1	1	1	2	1	1	1	2
Quartz	l.d.p.	25.7 (1.2)	25.1 (1.1)	24.1 (1.1)	30.9 (1.0)	37.5 (1.4)	32.7 (1.6)	40.6 (1.2)	32.5 (1.5)	37.3 (1.3)	35.1 (1.1)	33.2 (2.0)	36.8 (1.2)	32.9 (1.4)	38.8 (1.2)
Plagioclase		22.1 (1.4)	23.6 (2.0)	16.8 (1.1)	22.5 (1.2)	29.3 (1.6)	26.1 (1.7)	28.7 (1.3)	25.7 (1.8)	26.0 (1.5)	30.2 (1.1)	32.5 (2.3)	31.7 (1.3)	33.0 (1.4)	28.3 (1.3)
Illite + muscovite		17.9 (2.7)	18.5 (3.7)	13.6 (2.5)	12.5 (2.0)	16.1 (2.4)	23.3 (3.0)	14.8 (2.1)	22.9 (2.8)	14.4 (2.1)	15.3 (1.9)	10.1 (3.9)	13.8 (1.8)	15.0 (2.0)	15.0 (1.7)
K-feldspar		7.5 (9)	9.3 (1.3)	5.7 (8)	5.5 (8)	8.3 (1.1)	9.0 (1.0)	8.5 (9)	10.6 (1.2)	7.9 (1.0)	9.5 (9)	11.2 (1.3)	9.4 (1.1)	8.7 (1.2)	6.0 (8)
Chlorite + biotite		2.8 (9)	3.1 (1.3)	1.5 (9)	0.8 (4)	2.3 (7)	3.3 (1.0)	1.3 (6)	1.2 (6)	1.3 (8)	3.3 (8)	4.7 (1.3)	3.2 (8)	3.0 (1.3)	1.5 (7)
Hematite		0.8 (2)	0.8 (3)	0.7 (2)	0.7 (2)	2.1 (2)	1.4 (2)	2.5 (2)	1.5 (2)	1.4 (2)	0.9 (2)	2.0 (3)	1.2 (2)	1.1 (3)	1.3 (2)
Anhydrite		21.7 (1.1)	17.0 (1.4)	36.7 (1.4)	24.3 (8)	n.d.[a,b]	1.7 (5)	0.9 (5)	2.1 (5)	6.9 (6)	2.1 (5)	1.1 (7)	n.d.[b]	2.7 (4)	1.9 (4)
Analcime		1.2 (5)	1.2 (7)	0.8 (5)	1.7 (6)	1.3 (6)	n.d.[a]	2.7 (4)	1.2 (8)	1.5 (8)	1.7 (6)	2.3 (8)	1.8 (7)	1.5 (8)	2.3 (5)
Dolomite		n.d.	0.9 (4)	n.d.	1.2 (5)	2.7 (4)	2.3 (6)	n.d.	2.3 (7)	2.2 (5)	1.9 (5)	3.0 (8)	2.0 (5)	2.0 (6)	2.5 (4)
Halite		0.5 (2)	0.7 (2)	n.d.	n.d.	0.4 (2)	n.d.	n.d.	n.d.	0.3 (2)	n.d.	n.d.	n.d.	n.d.	2.4 (2)
Σ		100.01	99.99	100.00	100.00	100.00	100.01	100.00	100.01	99.99	100.01	100.00	99.99	99.99	100.01

Sample no.	B3-1					B3-3					B4-2				
Depth (m)	629.6–630.0					631.2–632.2					633.5–633.7				
Run duration (months)	0	15	21	24	40	0	15	21	24	40	0	15	21	24	40
Number of individual samples per set	1	1	1	1	1	1	1	1	1	2	2	1	1	1	1
Quartz	35.7 (1.3)	36.1 (1.3)	40.6 (1.3)	38.8 (1.4)	38.1 (1.5)	38.7 (1.2)	37.8 (1.4)	41.4 (1.2)	39.4 (1.4)	37.9 (1.4)	27.3 (1.5)	28.2 (1.4)	37.9 (1.2)	32.9 (1.5)	40.5 (1.4)
Plagioclase	25.5 (1.3)	28.5 (1.5)	29.0 (1.3)	29.1 (1.5)	29.4 (1.6)	29.8 (1.2)	35.1 (1.4)	27.4 (1.2)	28.8 (1.4)	30.5 (1.5)	24.0 (1.7)	24.3 (1.7)	26.5 (1.3)	22.5 (1.6)	27.6 (1.3)
Illite + muscovite	13.9 (2.0)	15.2 (2.1)	17.9 (2.0)	16.5 (2.3)	14.0 (2.9)	14.4 (1.9)	10.6 (1.7)	12.0 (1.9)	16.5 (2.2)	16.7 (2.2)	21.9 (3.6)	29.2 (2.7)	13.6 (2.0)	25.8 (2.6)	15.4 (2.1)
K-feldspar	5.6 (9)	9.0 (1.0)	7.6 (9)	8.9 (1.1)	7.1 (9)	8.6 (9)	10.3 (1.1)	7.2 (8)	8.4 (1.0)	7.9 (1.0)	8.6 (1.1)	12.5 (1.2)	8.2 (9)	10.0 (1.0)	8.6 (9)
Chlorite + biotite	4.6 (1.3)	1.5 (7)	1.4 (6)	1.1 (6)	1.7 (8)	3.4 (1.0)	1.6 (1.1)	2.8 (1.0)	2.4 (8)	1.9 (8)	3.1 (1.2)	3.3 (7)	2.2 (1.1)	3.8 (1.1)	3.4 (1.1)
Hematite	3.1 (2)	2.2 (2)	1.8 (2)	2.2 (2)	1.1 (2)	0.7 (2)	1.1 (2)	0.8 (1)	1.3 (2)	1.1 (2)	4.5 (4)	1.2 (2)	0.8 (2)	3.1 (3)	0.8 (2)
Anhydrite	n.d.[a]	n.d.	n.d.	n.d.	n.d.[b]	n.d.[a]	n.d.	n.d.	n.d.	n.d.	2.0 (6)	n.d.	n.d.	n.d.	n.d.
Analcime	11.6 (8)	7.3 (8)	1.6 (5)	3.4 (9)	4.3 (8)	4.2 (7)	1.2 (7)	6.1 (6)	3.1 (7)	2.5 (7)	8.2 (9)	1.3 (6)	8.4 (7)	1.9 (9)	2.4 (6)
Dolomite	n.d.	n.d.	0.9 (4)	n.d.	n.d.	n.d.	n.d.	n.d.	n.d.	n.d.	n.d.	n.d.	n.d.	n.d.	n.d.
Halite	n.d.	n.d.	0.7 (2)	n.d.	4.2 (3)	n.d.	2.1 (3)	2.4 (2)	n.d.	1.4 (2)	0.3 (2)	n.d.	2.3 (2)	n.d.	1.2 (2)
Σ	100.00	100.00	99.99	100.00	99.99	100.01	100.00	100.00	100.00	100.00	100.04	100.00	100.00	100.00	100.01

Set: 1 untreated, 2 15 months, 3 21 months, 4 24 months, 5 40 months of CO_2 treatment

Number in parenthesis denotes analytical error

l.d.p. lost during preparation, n.d. not detected

[a] n.d presence proven by EMPA

[b] n.d presence proven by SEM

Fig. 2 a Sketch of a Teflon-coated autoclave used for the siltstone experiments. **b** View on the core section B1-2; *dashed lines* indicate saw profiles. **c** *Top view* on core section base plane; *dashed lines* indicate saw profiles; *numbers* label sections used for baseline characterization; *blue area* marks inner core section used for the experiment. **d** *Top view* on inner core section with saw profiles indicated by *dashed lines*; *Roman numbers* label core prisms that are placed into autoclaves (KST I–III were treated with CO_2; KST IV with N_2). **e** Exemplary picture of KST II just after recovery from the autoclave
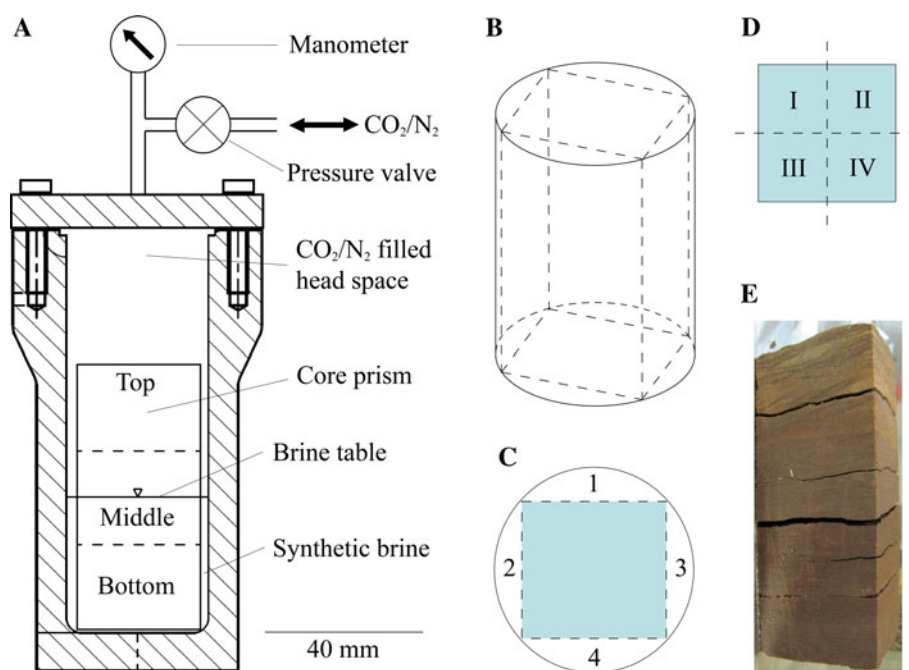
experiments with 15 months run time were already discussed in Fischer et al. (2010) and the reader is referred to this paper for more details on sample preparation. For sampling, the autoclaves were opened and fluid and rock samples were taken. After each sampling, autoclaves were closed again, re-pressurized to 5.5 MPa using a CO_2 flask and put back into the heating cabinet. Initial rock to brine weight ratios were between 2:1 and 4:1, typically representing between 470 to 640 g rock and 140 to 230 ml synthetic brine.

For the siltstone experiment core section B1-2 was sawed into four $4 \times 4 \times 8$ cm rectangular prisms (Fig. 2b–d). These prisms (KST I, II, III, and IV) were placed into four individual Teflon-coated autoclaves (Fig. 2a). Offcuts from the core section were used for baseline characterization (=untreated sub-samples). Because of the unwanted re-equilibration reactions due to synthetic brine used in the sandstone experiments (see above) updated data was used to prepare a synthetic brine with a composition analogous to original Ketzin reservoir brine. Based on pump test data obtained after borehole completion at Ketzin (Würdemann et al. 2010), the synthetic brine was prepared by dissolving 229.81 g NaCl, 8.54 g $MgSO_4 \cdot 7H_2O$, 5.79 g $CaCl_2$, 0.54 g KCl, and 0.03 g $FeCl_3 \cdot 6H_2O$ in one liter of deionized water. Initially, sample prisms were pre-saturated with the synthetic brine and then stored halfway in it for the experiments to simulate different conditions within the reservoir. The residual headspace was filled with ≥99.9 vol. % pure CO_2. Consequently, the bottom part of the prisms corresponds to a brine saturated reservoir, the upper part corresponds to

reservoir parts saturated with a free CO_2 phase and the middle part corresponds to the CO_2-brine interface layer. Individual experiments were run for 2 (KST II), 4 (KST I) and 6 months (KST III), respectively; one autoclave was filled with N_2 instead of CO_2 to serve as blank experiment and also reacted for 6 months (KST IV; Table 2). To achieve the desired experimental P–T conditions of 7.5 MPa and 40 °C, autoclaves were cooled in icy water during CO_2 filling to allow for a higher density and hence higher pressure after heating. About 230 g rock and 55 ml brine were loaded into the autoclaves resulting in a rock to brine weight ratio of approximately 3.5:1. At the end of each individual experiment, autoclaves were opened and brine and rock samples were taken. According to their position within the autoclave, rock samples were split into top, middle, and bottom section (Fig. 2a).

Analytical techniques

All rock samples were washed several times with deionized water and cautiously dried at 45 °C prior to further analytical treatment (additional details on analytical techniques can be found in Fischer et al. 2010). Individual samples were then analyzed by optical microscopy, X-ray diffraction (XRD) with Rietveld refinement, electron microprobe analysis (EMPA), and scanning electron microscopy (SEM). For thin section preparation samples were embedded in blue colored epoxy resin.

Petrographic thin section analyses were done on a Leitz polarizing microscope. Average grain sizes of each sample were determined based on measured long-axes of about 50

Table 2 Modal siltstone composition (wt%) as determined by XRD

Sample labels	Baseline			KST II			KST I			KST III			KST IV		
Gas medium	/			CO$_2$			CO$_2$			CO$_2$			N$_2$		
Months	0			2			4			6			6		
Section	Top	Middle	Bottom	Top	Middle	Bottom	Top	Middle	Bottom	Top	Middle	Bottom	Top	Middle	Bottom
Quartz	30.7 (7)	32.5 (7)	32.2 (8)	31.6 (9)	30.0 (9)	32.5 (9)	32.7 (8)	34.5 (6)	31.3 (8)	32.6 (8)	31.4 (8)	33.2 (9)	26.3 (8)	34.5 (8)	35.0 (8)
Plagioclase	24.0 (8)	22.2 (8)	22.3 (8)	24.6 (9)	22.8 (1.0)	26.5 (1.0)	25.3 (8)	23.6 (6)	24.2 (9)	23.5 (8)	23.3 (8)	23.8 (8)	23.4 (1.0)	27.7 (8)	24.5 (8)
Illite + Muscovite	23.6 (1.6)	26.8 (1.3)	26.3 (1.5)	23.2 (1.7)	27.1 (1.8)	23.1 (1.8)	20.1 (1.5)	21.8 (1.0)	25.8 (1.6)	21.0 (1.5)	26.3 (1.4)	26.5 (1.8)	27.4 (1.8)	20.6 (1.5)	22.8 (1.4)
K-feldspar	10.8 (6)	9.6 (6)	10.7 (6)	10.8 (6)	11.6 (7)	10.9 (6)	10.1 (6)	9.8 (6)	10.7 (7)	10.5 (6)	10.4 (7)	9.3 (6)	9.3 (7)	10.3 (6)	9.5 (6)
Chlorite + Biotite	5.0 (8)	6.3 (8)	5.8 (7)	5.6 (8)	5.6 (8)	4.6 (8)	4.8 (7)	7.7 (7)	5.6 (8)	5.8 (7)	6.0 (8)	4.8 (8)	3.5 (8)	4.8 (7)	5.7 (8)
Hematite	1.2 (1)	1.6 (1)	1.8 (1)	1.0 (1)	1.7 (1)	1.3 (1)	0.9 (1)	1.6 (1)	1.4 (1)	1.0 (1)	1.7 (1)	1.6 (1)	0.8 (1)	1.3 (1)	1.6 (1)
Anhydrite	3.7 (2)	n.d.	n.d.	2.0 (2)	n.d.	n.d.	5.5 (3)	n.d.	n.d.	4.3 (2)	n.d.	n.d.	9.1 (4)	n.d.	n.d.
Analcime	1.1 (4)	1.0 (4)	0.9 (4)	1.1 (4)	1.2 (4)	1.1 (4)	0.7 (2)	1.0 (3)	0.9 (4)	1.3 (4)	0.9 (4)	0.9 (3)	0.2 (2)	0.9 (3)	1.0 (4)
Σ	100.00	100.01	100.01	100.00	100.01	100.01	100.00	100.00	100.01	100.00	100.00	100.01	100.00	100.00	100.00

Number in parenthesis denotes analytical error

n.d. not detected

grains per sample. Roundness and sorting were determined by standard charts for comparison (Pettijohn et al. 1987).

For XRD analyses with Rietveld refinement powder specimens were obtained from the washed samples. Powders were homogenized in an agate mortar and pestle for about 10 min and then evenly spread on glass slides. X-ray diffraction patterns were collected on an Empyrean Panalytical diffractometer. Data were recorded between 4 and 75°2θ at a scan rate of 1°2θ per minute. AUTOQUAN software (a graphical user interface of BGMN software) was used for Rietveld calculations. Plagioclase was refined as albite and K-feldspar as orthoclase. Separate refinements of illite versus muscovite and of chlorite versus biotite failed due to peak overlapping. Therefore, refinements were simplified by refining only illite and chlorite taking these phases also as proxies for muscovite and biotite. Chlorite (+biotite) was refined as chamosite-7A, while illite (+muscovite) was refined as illite and illite_IMt-2 (after Gailhanou et al. 2007). Results of XRD Rietveld calculations were very sensitive to the choice of the illite phase and deviating results were gained depending on which illite phase was refined.

Electron microprobe analyses (EMPA) were conducted on a Cameca SX 100 and a JEOL JXA-8500F Hyperprobe field emission micro analyzer, respectively. The JEOL JXA-8500F was operating at 15 kV and 15 nA. Smithsonian international mineral standards (Jarosewich et al. 1980) were used for standardization. Counting times were 20 s on peak and 10 s on background and the beam was defocused to 3 μm for sheet silicates and to 5 μm for feldspars and sulfates. Freshly broken and carbon-coated rock fragments were used for SEM analysis, which was done on a Zeiss ultra 55 plus equipped with an energy dispersive X-ray system (EDS). Backscattered electron (BSE) images were taken from polished and carbon-coated thin sections.

Fluid data of the sandstone experiments (Table 3) was acquired by Wandrey et al. (2011; additional data: M. Wandrey, personal communication). For fluid analysis, solids were removed by filtration and centrifugation. Cation and anion concentrations of K$^+$, Ca^{2+}, Mg^{2+}, Mn^{2+}, Fe^{2+}, Sr^{2+}, Al^{3+}, Si^{4+}, NO$_3^-$, SO$_4^{2-}$ were determined in 1:100 dilutions (Cl$^-$ = 1:5,000; Na$^+$ = 1:10,000) using ICP-AES and ion chromatography, respectively. Fluid data of the siltstone experiments is listed in Table 4.

Geochemical modeling

To reproduce the observations of the sandstone experiments with theoretical modeling results, the speciation software PHREEQC (version 2.18; Parkhurst and Appelo 1999) was used for reactive geochemical modeling. The Pitzer-based Eq3/6 database (Wolery 1992), which was

Springer

Table 3 Fluid data of sandstone samples as determined by ICP-AES and ion chromatography, respectively

Sample no.	Reservoir fluid	B2-1				B2-2				B2-3			
Run duration (months)		0	15	21	24	0	15	21	24	0	15	21	24
Na^+	3.93	3.11	3.27	3.19	3.33	3.11	3.24	3.30	3.29	3.11	3.33	3.28	3.39
K^+	7.21	10.22	11.32	12.62	11.43	10.22	15.49	20.09	15.36	10.22	15.19	17.05	15.66
Ca^{2+}	52.15	33.44	62.85	61.87	60.69	33.44	62.32	64.55	60.92	33.44	62.18	60.36	61.19
Mg^{2+}	34.64	39.54	45.39	42.73	43.92	39.54	45.16	43.61	47.60	39.54	44.35	43.08	43.96
Fe^{2+}	0.10	b.d.l.	1.93	2.16	0.11	b.d.l.	0.21	b.d.l.	0.19	b.d.l.	0.03	0.38	0.04
Sr^{2+}	0.56	0.00	0.31	0.35	0.34	0.00	0.41	0.43	0.42	0.00	0.39	0.38	0.38
Mn^{2+}	0.03	b.d.l.	0.08	0.13	0.21	0.00	0.10	0.07	0.15	b.d.l.	0.04	0.12	0.22
Al^{3+}	b.d.l.	0.12	0.30	0.20	b.d.l.	0.12	0.18	0.19	b.d.l.	0.12	0.27	0.33	b.d.l.
Si^{4+}	b.d.l.	b.d.l.	0.04	0.12	b.d.l.	b.d.l.	b.d.l.	b.d.l.	b.d.l.	b.d.l.	b.d.l.	b.d.l.	b.d.l.
Cl^-	3.92	3.21	3.21	3.36	3.45	3.21	3.23	3.38	3.39	3.21	3.41	3.34	3.49
NO_3^-	b.d.l.	0.16	0.14	0.19	b.d.l.	0.16	0.13	b.d.l.	b.d.l.	0.16	0.07	b.d.l.	b.d.l.
SO_4^{2-}	38.97	2.28	28.42	35.50	32.17	2.28	30.55	38.20	36.11	2.28	33.69	39.17	38.33
TDS	236	188	196	200	206	188	196	204	204	188	205	202	209

Sample no.	B3-1				B3-3				B4-2			
Run duration (months)	0	15	21	24	0	15	21	24	0	15	21	24
Na^+	3.11	l.d.p.	3.27	3.28	3.11	3.23	3.27	3.26	3.11	3.28	3.26	3.30
K^+	10.22		18.19	16.82	10.22	17.27	19.59	17.39	10.22	12.34	13.85	12.11
Ca^{2+}	33.44		55.97	55.52	33.44	52.95	53.37	52.55	33.44	59.76	57.27	58.22
Mg^{2+}	39.54		39.14	39.63	39.54	42.92	42.24	42.54	39.54	41.44	39.43	39.98
Fe^{2+}	b.d.l.		2.11	0.81	b.d.l.	0.01	0.07	0.07	b.d.l.	1.36	1.74	1.28
Sr^{2+}	0.00		0.30	0.29	0.00	0.27	0.33	0.34	0.00	0.34	0.35	0.35
Mn^{2+}	b.d.l.		0.04	0.09	b.d.l.	0.01	0.04	0.07	b.d.l.	0.03	0.04	0.06
Al^{3+}	0.12		0.18	0.01	0.12	0.20	0.21	b.d.l.	0.12	0.29	0.23	b.d.l.
Si^{4+}	b.d.l.		0.08	b.d.l.	b.d.l.	b.d.l.	b.d.l.	b.d.l.	b.d.l.	b.d.l.	b.d.l.	b.d.l.
Cl^-	3.21		3.39	3.38	3.21	3.22	3.34	3.34	3.21	3.25	3.38	3.40
NO_3^-	0.16		b.d.l.	b.d.l.	0.16	0.05	0.01	0.16	0.16	0.14	0.13	b.d.l.
SO_4^{2-}	2.28		36.12	37.01	2.28	28.47	33.15	32.76	2.28	31.37	36.32	37.85
TDS	188		203	203	188	195	201	200	188	198	202	204

Ion concentrations are in mmol/L; Na^+ and Cl^- are in mol/L; TDS is in g/L

Reservoir fluid after Würdemann et al. (2010)

l.d.p. Lost during preparation, *b.d.l.* below detection limit

transformed to PHREEQC format by Quintessa Ltd. (Benbow et al. 2008), was applied. The Quintessa database includes Al as well as Si species enabling the setup of geochemical models also considering aluminosilicate reactions (for details see De Lucia et al. 2012). The models are corrected for high CO_2 partial pressures and high salinity fluids. To fully characterize the initial solution used during modeling (i.e. the synthetic brine), pH was taken from pump test data (Würdemann et al. 2010) and pe was determined iteratively. Brine density was calculated using SoWaT software (Driesner and Heinrich 2007; Driesner 2007) based on mole fraction of NaCl and P–T conditions. The average porosity was set to 20.5 %.

In a first step, an equilibrium model (EQUI-MOD_1) was calculated to analyze CO_2-independent reactions by equilibrating the mineral assemblage of the bulk sandstone with the initial synthetic brine composition. Amounts of minerals present per kilogram water (mol/kgw) were taken from mineral abundances as determined by XRD analysis (Table 1). Due to the unavailability of kinetic data for muscovite and biotite, illite, and chlorite are considered as proxies, respectively, making the modeling results also more comparable to those of the XRD measurements (see above). The models are scaled to the amount of pure water present in the autoclave, which is a function of initial brine volume, brine density, and total dissolved solids (TDS).

Table 4 Fluid data of siltstone samples as determined by ICP-AES and ion chromatography, respectively

Sample labels Gas medium Months	Initial brine-untreated / 0	KST II CO_2 2	KST I CO_2 4	KST III CO_2 6	KST IV−blank N_2 6
Na^+	3.93	3.97	4.05	4.05	4.09
K^+	8.77	19.99	19.44	19.18	18.67
Ca^{2+}	53.50	60.89	64.87	64.87	64.87
Mg^{2+}	35.84	48.84	45.26	49.37	37.44
Fe^{2+}	0.08	n.d.	b.d.l.	b.d.l.	b.d.l.
Sr^{2+}	0.01	0.24	0.24	0.27	0.24
Mn^{2+}	b.d.l.	b.d.l.	0.04	0.03	b.d.l.
Cl^-	4.18	3.91	4.09	4.10	4.14
SO_4^{2-}	28.11	32.27	27.07	103.06	102.02

Ion concentrations are in mmol/L, Na^+ and Cl^- are in mol/L

b.d.l. Below detection limit, *n.d.* not detected

The complex mineralogical composition of the reservoir samples derived by laboratory measurements cannot be transposed directly into geochemical models. The following simplifications were made: (1) quartz was considered inert and thus excluded from modeling, (2) plagioclase solid solution is represented by a corresponding mixture of albite and anorthite end-members, (3) iron-rich end-member chamosite-7A $Fe_2[Al_2SiO_5(OH)_4]$ was chosen as proxy for chlorite, and (4) illite $K_{0.6}(Al_{1.8}Mg_{0.25})[Si_{3.5}Al_{0.5}O_{10}(OH)_2]$ as well as illite_IMt-2 $(Na_{0.044}K_{0.762})(Al_{1.427}Fe_{0.376}Mg_{0.241})[Si_{3.387}Al_{0.613}O_{10}(OH)_2]$ were both tested as illite phases. Note that the XRD Rietveld refinements were very sensitive to the choice of the illite phase (see above), and results of calculations either refining illite or illite_IMt-2 strongly deviated in terms of mineral abundance of the respective illite phase. Accordingly, both illite phases were included to test for suitability in matching experimental observations during geochemical modeling.

In a second step (EQUI-MOD_2), CO_2 was added to the equilibrium model to identify most probable reactions explaining measured brine data (Table 2) in the presence of CO_2. More than 2,500 distinct equilibrium models were run within EQUI-MOD_2 that covered all possible combinations of albite, analcime, anhydrite, anorthite, calcite, chamosite-7A, dolomite, hematite, illite, illite_IMt-2, K-feldspar, and kaolinite. Out of these, 1,946 simulations converged and could be analyzed statistically. Note that calcite and kaolinite were arbitrarily added as primary minerals even if they were not detected in XRD analysis. Carbon dioxide is introduced as an equilibrium gas phase with a pressure ($P = 5.5$ MPa) corrected saturation index (CO_2 log fugacity $= 1.6$). The system is maintained saturated with respect to CO_2 during all time steps. To acquire the models that best match the measured ion brine

concentrations after 24 months, the following dispersion relation (Eq. 1) has been defined and applied:

$$MV = \sqrt{\frac{1}{N}\sum_{i=1}^{N}\left(\frac{S_i - M_i}{M_i}\right)^2} \tag{1}$$

where MV is the match value, i is the respective ion, S is the simulated brine ion concentration, M is the measured brine ion concentration after 24 months, N is the number of ions to be matched. Consequently, results of the best matching EQUI-MOD_2 models were evaluated based on distinct ion derivations from the measured values (e.g. simulated K^+ concentration of the distinct simulations versus measured K^+ concentration).

The final modeling step was the introduction of kinetic rate equations for water–rock reactions. The following general kinetic rate equation (Eq. 2) for mineral dissolution and precipitation is used (Lasaga 1984):

$$rate_i = \frac{dm}{dt} = \pm k(T)_i \times S_{r_i} \times m_i \times \left[1 - \left(\frac{Q_i}{K_i}\right)^\theta\right]^\eta \tag{2}$$

where rate is the dissolution/precipitation rate (mol/s) of mineral i, $k(T)$ is the temperature dependent reaction rate constant (mol/cm^2 s), S_r is the specific reactive surface area, Q is the corresponding ion activity product and K is the equilibrium constant at temperature T. The exponentials θ and η are empirical fitting parameters that are typically set to unity due to missing experimental data (e.g. Palandri and Kharaka 2004; Cantucci et al. 2009). Note that rate > 0 denotes dissolution, and rate < 0 denotes precipitation. The temperature dependency of the reaction rate constant k is described by an Arrhenius type equation accounting for acid (H^+), neutral pH, and base (OH^-) mechanisms (Eq. 3). For

Springer

Table 5 Distinct kinetic models for the set of KIN-MOD_2 scripted based on results obtained from EQUI-MOD_2

KIN-MOD_2	.1	.2	.3	.4	.5	.6
Mineral phases	Albite			Albite	Albite	Albite
		Analcime	Analcime		Analcime	Analcime
	Anhydrite	Anhydrite	Anhydrite	Anhydrite	Anhydrite	Anhydrite
						Chalcedony
	Dolomite			Dolomite	Dolomite	Dolomite
	Hematite	Hematite	Hematite	Hematite	Hematite	Hematite
	Illite	Illite			Illite	Illite
		Kaolinite	Kaolinite	Kaolinite	Kaolinite	Kaolinite

Analcime, anhydrite and dolomite were modeled as equilibrium phases; quartz is considered inert in all models

$T = 313.15$ K, the full equation implemented in PHREEQC is the sum of these three mechanisms (cf. Lasaga 1984; Palandri and Kharaka 2004):

$$
k(T) = k_{298.15}^{N} \exp\left(\frac{-E_a^{N}}{R}\left(\frac{1}{T} - \frac{1}{298.15}\right)\right)
$$
$$
+ k_{298.15}^{A} \exp\left(\frac{-E_a^{A}}{R}\left(\frac{1}{T} - \frac{1}{298.15}\right)\right)[H^+]^{n_A}
$$
$$
+ k_{298.15}^{B} \exp\left(\frac{-E_a^{B}}{R}\left(\frac{1}{T} - \frac{1}{298.15}\right)\right)[H^+]^{n_B}
$$
(3)

where N, A and B denote neutral, acid and base mechanism, respectively, $k_{298.15}$ is the rate constant at 25 °C (mol/m² s), E_a is the activation energy (J/mol), R is the gas constant (8.314472 J/mol K), T is the absolute temperature (K), $[H^+]$ is the proton activity, and n represents the reaction order [dimensionless] with respect to $[H^+]$ of that species. The base mechanism from Eq. 3 was excluded from the calculations, since its effect on the overall rate $k(T)$ is orders of magnitude smaller than those of the other two mechanisms in the considered acidic system; this helped improving numerical performance and stability of the models. Precipitation rates of primary and secondary minerals are calculated using the same kinetic rate expression as for dissolution. Rate law parameters E_a, $\log k_{298.15}$ and n were taken from Palandri and Kharaka (2004). Parameters for illite were set to those of smectite; a reasonable approximation because different clay minerals have very similar dissolution rates in acidic environments (e.g. Köhler et al. 2003).

Similar to approaches by Gaus et al. (2005), Cantucci et al. (2009), and Klein et al. (2013), the specific reactive surface area S_r (cm²/g) is calculated based on the specific geometric surface area A_g (cm² g). According to Eq. 4 A_g is calculated using mineral density ρ (g/cm³) and average grain diameter d (cm):

$$
A_g = \frac{6}{\rho \times d}; \quad S_r = 0.001 \times A_g \times 10
$$
(4)

It is assumed that grains have spherical geometry with diameters of 20 and 200 μm for clay minerals (chlorite and illite) and non-clay minerals, respectively. Because mineral grain surfaces are only partly exposed to brine (due to coatings etc.) and thus involved in potential reactions, the geometry-based specific surface area (Eq. 4) is decreased by three orders of magnitude (factor 0.001; Lasaga 1995). A surface roughness factor of ten is defined additionally (e.g. Zerai et al. 2006).

While quartz was generally considered inert during kinetic modeling, analcime, anhydrite, and dolomite were defined as equilibrium phases due to their fast reaction kinetics that are orders of magnitude higher (e−4 to e−5) compared to the other minerals present (e−12 to e−13). Hence, only albite, anorthite, chamosite-7A, hematite, illite, illite-IMt_2, and K-feldspar were included into the kinetic models. While the first kinetic model (KIN-MOD_1) considers albite, anorthite, chamosite-7A, hematite, illite-IMt_2, and K-feldspar based on minerals proven by XRD analysis and for which kinetic data exist, the second set of kinetic models (KIN-MOD_2.1 to 2.4) comprises different combinations of albite, analcime, anhydrite, dolomite, hematite, illite, and K-feldspar based on the evaluation of EQUI-MOD_2. In addition to KIN-MOD_2.1 to 2.4 kinetic models KIN-MOD_2.5 and 2.6 were run, which comprise all minerals present in KIN-MOD_2.1 to 2.4 plus additional chalcedony (as an amorphous SiO₂ phase) in KIN-MOD_2.6 (Table 5; see Results of "Geochemical modeling").

The initially present average amount of plagioclase as determined by Rietveld refinement is 27.7 wt%, which transforms into 0.570 mol plagioclase for the initial average rock sample mass of 543 g. This amount is split half (0.285 mol) between albite and anorthite in order to also consider anorthite reactivity that is known to be higher in acidic environments. While KIN-MOD_1 only considers dissolution, the distinct runs of KIN-MOD_2 suppress precipitation of feldspar minerals (albite, anorthite, and K-feldspar) but include precipitation of the other phases. Precipitation of feldspar minerals is excluded (1) because it is rather unlikely for these minerals to form under the applied experimental P–T conditions, and (2) to increase computation performance. Note that no secondary

precipitates were detected during evaluation of the laboratory experiments. Precipitation rates were set equal to those of dissolution. Also identical kinetic rate expressions were used. The only difference was that the reactive surface area was proportional to the amount of mineral present during dissolution, but constant during precipitation (e.g., Gaus et al. 2005).

Results

Mineralogy

Sandstone

Sandstone compositions as determined by XRD analysis with Rietveld refinements are summarized in Table 1. Quartz (24.1–41.4 wt%), plagioclase (16.8–35.1 wt%), illite + muscovite (10.1–29.2 wt%) and typically perthitic K-feldspar (5.5–12.5 wt%) are major mineral phases, chlorite + biotite (0.8–4.7 wt%) and hematite (0.7–4.5 wt%) are minor constituents. Rock fragments are predominantly composed of either quartz and sheet silicates or mainly feldspar minerals with quartz, opaque phase(s) and sheet silicates. Opaque phases mainly consist of Ti–Fe-Oxi(hydroxi)des. In about every third sandstone sample halite (0.3–4.2 wt%) was verified by XRD analysis; the presence of halite is most likely a consequence of brine evaporation during sample recovery and preparation. Samples are weakly cemented by anhydrite, analcime, and subordinate dolomite. Cements occur as unevenly distributed, isolated poikilitic patches resulting in highly variable modal abundances of the respective minerals. Analcime is present in all samples reaching a maximum of 11.6 wt% in the untreated sample B3-1. Anhydrite and dolomite mainly occur in the upper sandstone sections (B2-1, B2-2, and B2-3) from 627.5 to 628.6 m depth. Especially the uppermost sample B2-1 is strongly cemented by anhydrite (max. 36.7 wt%). Traces of anhydrite were verified in the majority of samples. Dolomite—if present—varies from 0.8 to 3.0 wt%. The petrographic observations are in good accordance with results by Förster et al. (2010).

Despite an apparent variability between different samples and between subsets from the sandstone experiments, a few trends can be evaluated based on XRD data (exemplary plots for analcime, chlorite + biotite, and hematite are shown in Fig. 4). With run time, average analcime, chlorite + biotite as well as hematite abundances decrease from 5.4 to 2.4, 3.4 to 1.8, and 2.3 to 1.1 wt%, respectively. Quartz (not shown) contents are generally constant with 35–40 wt% although sample B4-2 indicates increasing quartz abundances with run time.

Siltstone

Petrographic characteristics of the siltstone sample are very similar to those of the sandstone samples. Major differences are: (1) smaller average grain sizes of mainly <63 μm classifying the sample as siltstone, (2) the absence of dolomite, and (3) the presence of pore-filling $(Ba,Sr)SO_4$ solid solution cement. The siltstone consists of 30.6 ± 4.3 wt% quartz, 25.0 ± 2.7 wt% plagioclase, 23.7 ± 3.6 wt% illite + muscovite, 10.4 ± 1.2 wt% K-feldspar (typically perthitic), 5.6 ± 2.1 wt% chlorite + biotite and 1.3 ± 0.5 wt% hematite (Table 3). Pore-filling cement phases are analcime, anhydrite, and $(Ba,Sr)SO_4$ solid solutions. While anhydrite predominantly occurs in the top section of the sub-samples in which it has abundances of 5.5 ± 3.5 wt%, analcime and $(Ba,Sr)SO_4$ solid solutions are present in all sub-samples, amount to about 1.0 wt% and occur in isolated patches (Fig. 3). None of the minerals identified by XRD shows a clear trend with run time. Mineral abundances are constant within analytical error or show only minor, insignificant changes (Fig. 4).

Mineral surfaces

Sandstone

Dolomite and analcime both occur clean and unaltered showing no corrosion textures even in samples treated for 40 months (Fig. 5d). First signs of anhydrite alteration occur along preferred crystallographic features and were observed in samples taken after 21 and 24 months, respectively (Fig. 5b). After 40 months, some anhydrite crystals display accentuated dissolution holes and fissures that are not restricted to crystallographic features (Fig. 5c). Plagioclase as well as K-feldspar grains show intense alteration. While a few untreated plagioclase grains have clean and unaltered surfaces occasionally (Fischer et al. 2011), plagioclase surfaces of CO_2-treated samples show intensified corrosion textures and advanced dissolution features. These are often crystallographically oriented, but some plagioclase grains are strongly corroded after 24 and 40 months and can have several large, and up to mm-deep dissolution holes (Fig. 5f). Similar, but less intense textures are found on K-feldspar grains of all five subsets. Despite the fact that euhedral albite grains were described in some samples treated for 15 months (Fischer et al. 2010), no such euhedral albite grains were found in the other sub-samples.

Fig. 3 Stitched BSE micrograph of the upper thin section from KST II showing different petrographic domains. *Arrows* indicate poikilitic occurrence of pore-filling anhydrite (anh) and (Ba,Sr)SO$_4$ solid solutions (ba,sr). Top of the thin section is also top of core prism. *fsp* Feldspars, *qtz* quartz
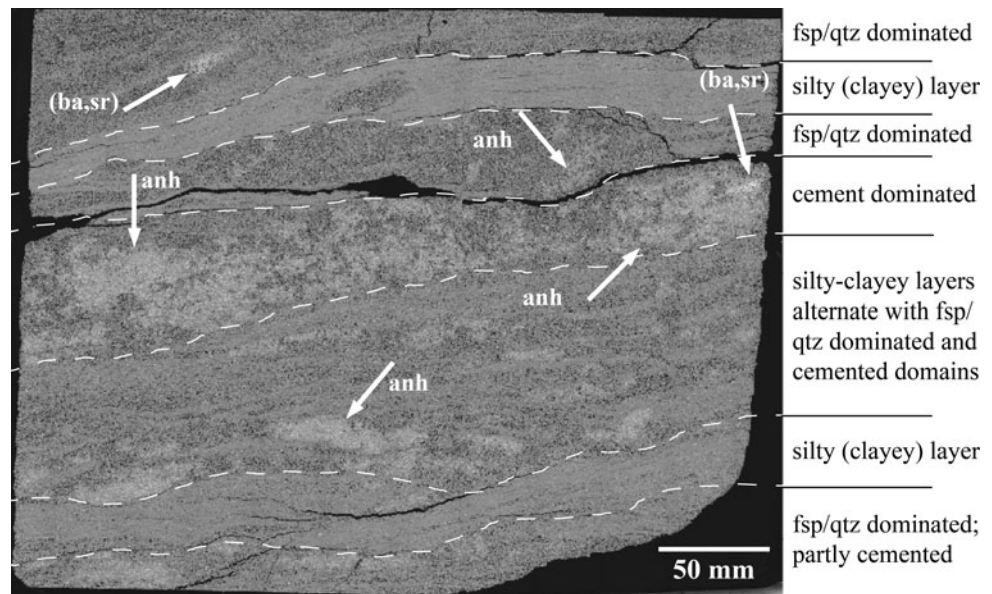
Siltstone

Compared to the untreated and N$_2$-treated samples, mineral surfaces of the CO$_2$-treated siltstone samples provide evidence for dissolution and corrosion processes. In general, the majority of untreated and N$_2$-treated plagioclase and K-feldspar grains are regular and clean. Irregular surface morphologies with pits and holes only occur occasionally. With progressing run time, these corrosion textures intensify (Fig. 6a, c, and e) and clean and unaffected feldspar surfaces become very scarce in the CO$_2$ experiment. While anhydrite grains and surfaces look fresh and clean in the untreated siltstone sample, they appear increasingly corroded with time (Fig. 6b). Some N$_2$-treated samples also indicate alteration of anhydrite. In some samples exposed to CO$_2$ for 6 months dissolution holes and pits on grain surfaces of quartz were found (Fig. 6d). Such textures do neither occur on quartz surfaces of untreated nor N$_2$-treated samples.

Mineral composition of the siltstone

During the siltstone experiment feldspar composition as determined by EMPA does not significantly change (Fig. 7; for mineral compositions of sandstone samples see Fischer et al. 2010). Plagioclase composition for untreated, CO$_2$- and N$_2$-treated samples generally shows two clusters; one with albite end-member (Ab$_{>90}$) and one with intermediate composition. Intermediate plagioclase composition is Ab$_{42-83}$An$_{14-56}$ in the untreated sample and Ab$_{37-88}$An$_{11-55}$, Ab$_{33-86}$An$_{12-65}$, and Ab$_{35-80}$An$_{13-63}$ in samples of 2, 4, and 6 months CO$_2$ exposure, respectively.

Samples of the N$_2$ blank have intermediate plagioclase composition of Ab$_{40-85}$An$_{10-60}$. K-feldspar composition of untreated, CO$_2$- and of N$_2$-treated samples is consistently Or$_{35-99}$. Very few measurements reveal intermediate alkali feldspar composition, or plot in the anorthoclase domain (Or$_{<30-10}$). Intermediate alkali feldspar analyses most probably represent mixed analyses of perthitic feldspar as typically observed in the samples.

No changes in compositions of sheet silicates are apparent. White mica is predominantly muscovite with rare and minor paragonite component; dark mica is biotite of the phlogopite–annite–siderophyllite solid solution. White mica of the untreated sample is (K$_{0.74-0.92}$Na$_{0.01-0.19}$Ca$_{<0.01-}$Ba$_{<0.02}\square_{0.02-0.19}$)(Al$_{1.39-1.92}Fe_{0.05-0.36}Mg_{0.05-0.35}Ti_{<0.13}$) [Al$_{0.47-0.96}Si_{3.04-3.53}O_{10}$|(OH)$_{1.93-2.00}F_{<0.06}Cl_{<0.01}$], untreated dark mica is (K$_{0.46-0.85}$Na$_{0.02-0.07}$Ca$_{<0.07}$Ba$_{<0.01}\square_{0.11-0.44}$) [Al$_{0.03-0.54}Fe_{0.83-1.55}Mg_{0.90-1.75}Ti_{0.05-0.26}$][Al$_{0.90-1.32}$ Si$_{2.68-3.10}$O$_{10}$|(OH)$_{1.52-1.98}$F$_{<0.12}$Cl$_{<0.44}$]. With time of CO$_2$ exposure and also compared to the N$_2$ blank all cations of white as well as dark mica are in the same range pfu and do not indicate any consistent trend. Note that a few biotite analyses from all investigated samples yield totals around or below 90 wt% oxides and possibly indicate chloritization of biotite.

Cement phase compositions are strictly stoichiometric and similar for the different sample sets. Analcime is pure Na$^+$ end-member; anhydrite has traces of Sr^{2+} (<0.02 pfu). Compositions of (Ba,Sr)SO$_4$ solid solutions range from 0.05 to 0.85 pfu Sr^{2+} and 0.12 to 0.94 pfu Ba^{2+}. No preferential dissolution of either cation is detected with time of CO$_2$ exposure; also compared to the N$_2$ blank.
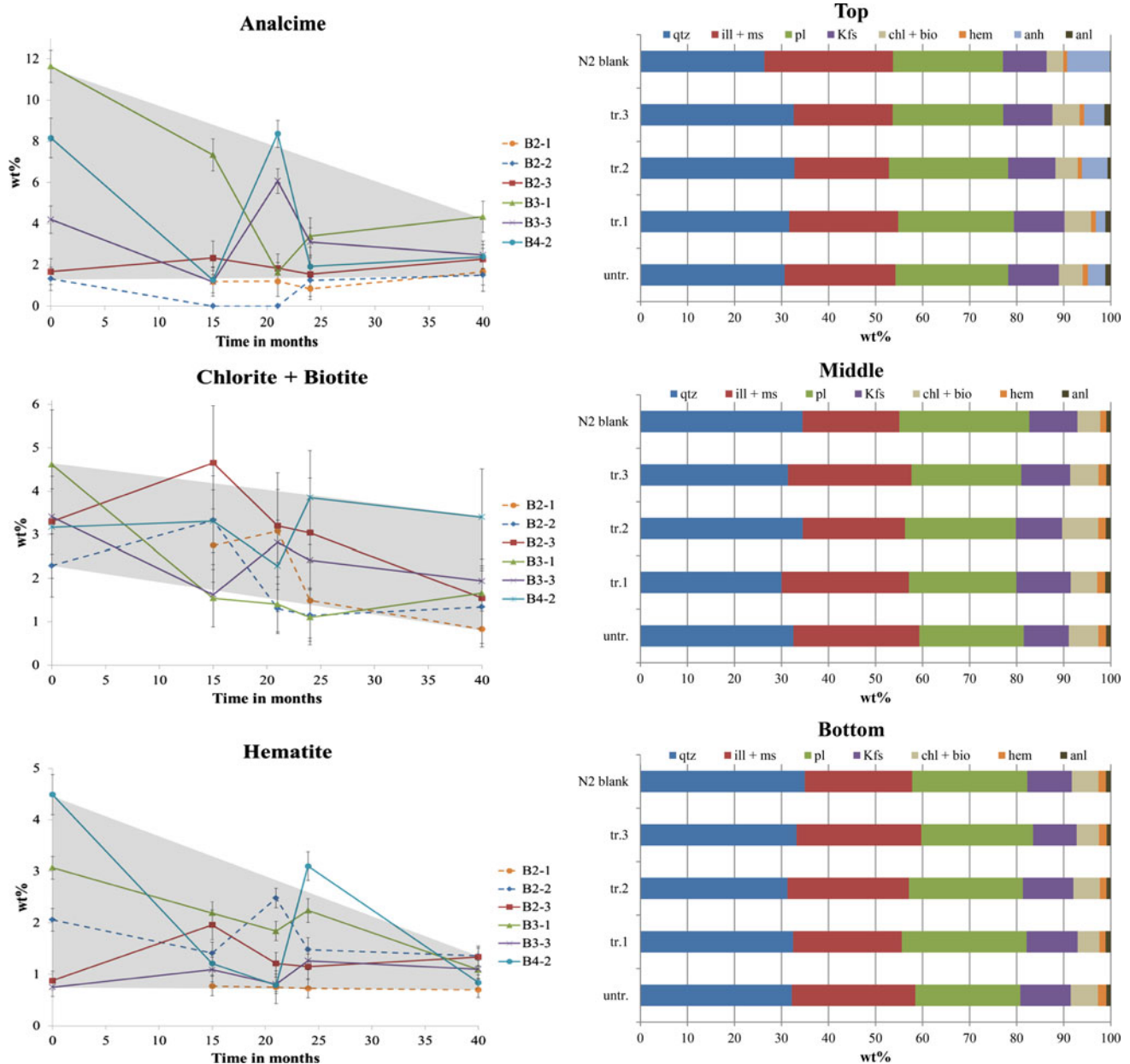
Fig. 4 Rietveld refined XRD data of sandstone (*left*) and siltstone samples (*right*). Exemplarily shown analcime, chlorite + biotite and hematite abundances in sandstone are plotted against run time. *Dashed lines* mark the strongly cemented sandstone samples B2-1 and B2-2. Mineral abundances in siltstone samples are separated into top, middle and bottom sections for untreated, treated 1-3 and N$_2$-blank test samples. Note that the untreated sandstone sample B2-1 was unfortunately lost during preparation. *qtz* quartz, *ill* illite, ms muscovite, *pl* plagioclase, *Kfs* K-feldspar, *chl* chlorite, *bio* biotite, *hem* hematite, *anh* anhydrite, *anl* analcime

Fluid chemistry

Sandstone

During the CO_2-exposure experiments, TDS concentrations increase from 188 g/L in the initial brine to 198 g/L (+5.1 %), 202 g/L (+7.2 %), and 205 g/L (+8.7 %) after 15, 21, and 24 months (Table 3), respectively. Note that fluid data of samples taken after 40 months is pending.

Variations in individual ion concentrations between successive experiments are rather low and individual trends are partly inconsistent (Fig. 8). The largest overall differences generally occur within the first 15 months. While Na^+, Mg^{2+}, and Cl^- increased between 6 and 10 % within 24 months of CO_2 exposure, K^+ (+44 %), Ca^{2+} (+77 %), SO_4^{2-} (+1,257 %) and Sr^{2+} (+14,943 %) show considerably higher increases in the same interval (Fig. 8). The fluid samples taken after 21 months have an average about
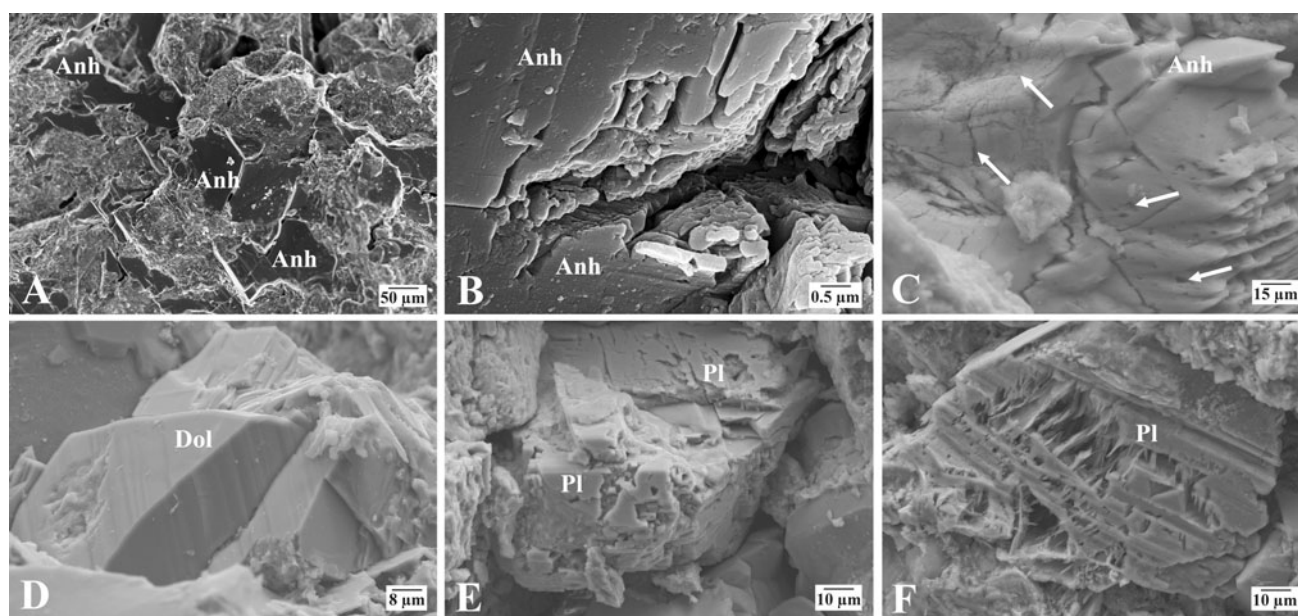
Fig. 5 Series of SEM micrographs taken from broken sandstone fragments. **a** typical pore-filling anhydrite cement of sample treated for 21 months, **b**, **c** corroded anhydrite of samples treated for 21 and 40 months, respectively (*arrows* show dissolution fissures and holes), **d** typical dolomite after 40 months of CO_2 treatment, **e**, **f** strongly corroded plagioclase crystals after 24 and 40 months, respectively. *anh* Anhydrite, *dol* dolomite, *pl* plagioclase
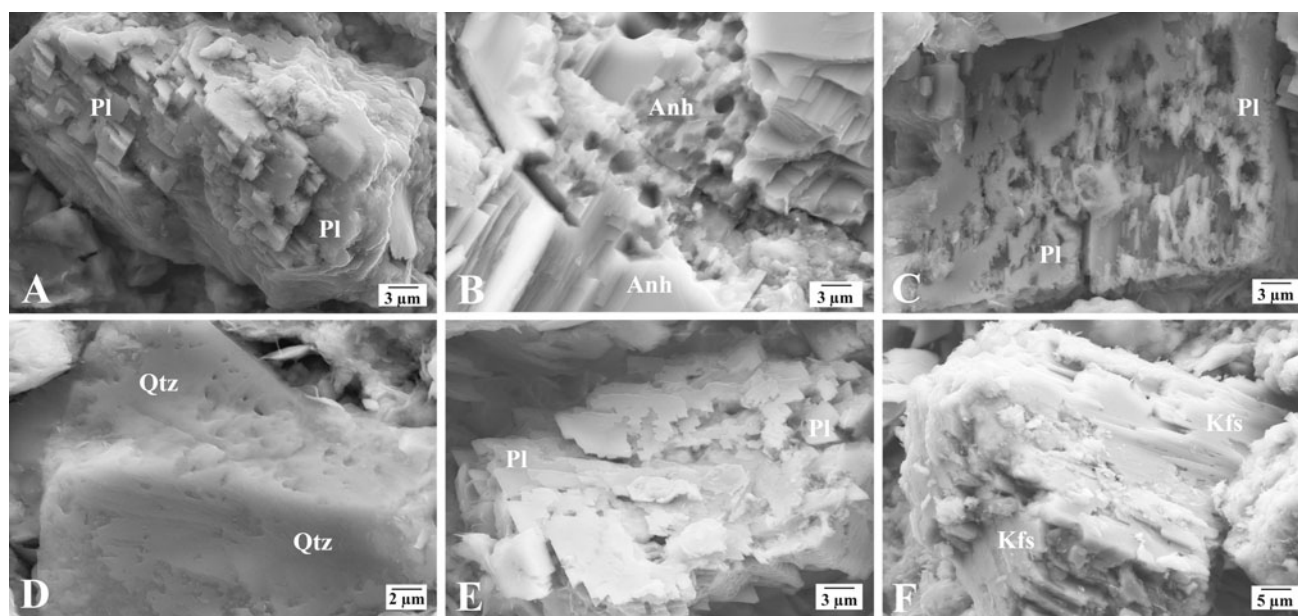
Fig. 6 Series of SEM micrographs taken from broken siltstone fragments. **a** Typical plagioclase in untreated siltstone. **b** Dissolution textures on anhydrite CO_2-treated for 6 months. **c** Strongly corroded plagioclase after 4 months of CO_2 treatment. **d** Dissolution pits and holes in quartz CO_2-treated for 6 months. **e** Corrosion textures on plagioclase occurring after 6 months of CO_2 treatment. **f** Typical K-feldspar grains from the N_2 blank. *pl* Plagioclase, *anh* anhydrite, *qtz* quartz, *Kfs* K-feldspar

4 % lower Mg^{2+} concentrations than those taken after 15 months. Potassium as well as SO_4^{2-} concentrations reached maximum values in samples treated for 21 months and declined thereafter. Ferrous iron and Mn^{2+}, both not added to the initial synthetic brine, increased to 7.1e−4 and 5.2e−5 mol/L in samples treated for 15 months, respectively. Note that Fe^{2+} concentrations in the sandstone experiments show two different clusters; one cluster with "low" Fe^{2+} concentrations below 3.8e−4 mol/L (in samples B2-2, B2-3, and B3-3), the other with "high" Fe^{2+}

Fig. 7 Feldspar compositions in ternary plots for the different siltstone samples separated into top, middle and bottom domains as determined by EMPA. Despite some minor variability between the samples no significant compositional trend is apparent
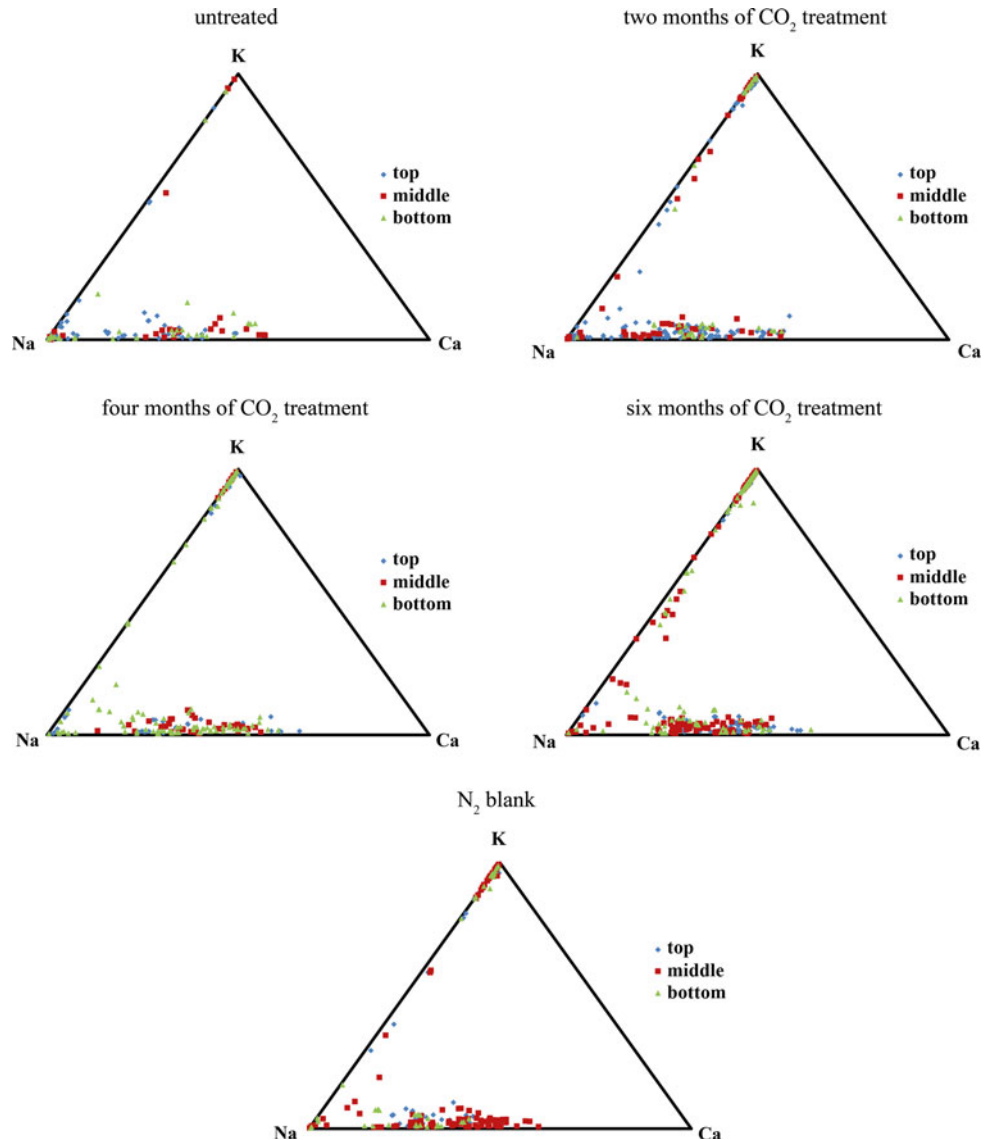
concentrations between 8.1e−4 and 2.2e−3 mol/L (in samples B2-1, B3-1 and B4-2). Silicon was below detection limit in all but two samples from B2-1. Compared to the initial synthetic brine, Al^{3+} shows a coherent increase in samples treated for 15 months, but an inconsistent trend for the period between 15 and 21 months. Concentrations of Al^{3+} in samples B2-1 and B4-2 decrease significantly within 21 months run time (−31 and −20 %, respectively) but increase by +4 % (B2-2), +5 % (B3-3) and +23 % (B2-3) in the other samples. Note that Al^{3+} concentrations were below detection limit in all samples treated for 24 months.

Siltstone

Ion concentrations in the sampled brine generally increase during the siltstone experiment (Fig. 9; Table 4). Changes

of TDS, Na^+ and Cl^- concentrations between different samples are within analytical error (conservatively expected to be ±5 %). Potassium concentrations increased rapidly and reached a maximum of 2.0e−2 mol/L after 2 months. Calcium increases from initially 5.4 to 6.5e−2 mol/L after 4 months, and exhibits constant concentrations afterwards. Magnesium as well as Sr^{2+} show rapid concentration increases from 3.6e−2 to 4.9e−2 mol/L and from 9.5e−6 to 2.4e−4 mol/L after 2 months, respectively, and constant concentration levels within analytical error thereafter. Sulfate concentrations are unchanged within the first 4 months of CO_2 treatment, but reveal a rapid increase from about 3.9e−2 to 1.0e−1 mol/L to the end. Ferrous iron was only detected in the initial brine, Mn^{2+} was only detected in brine samples after 4 and 6 months. After 6 months, the majority of measured brine ion concentrations in the CO_2-treated sample as well as in the N_2-blank
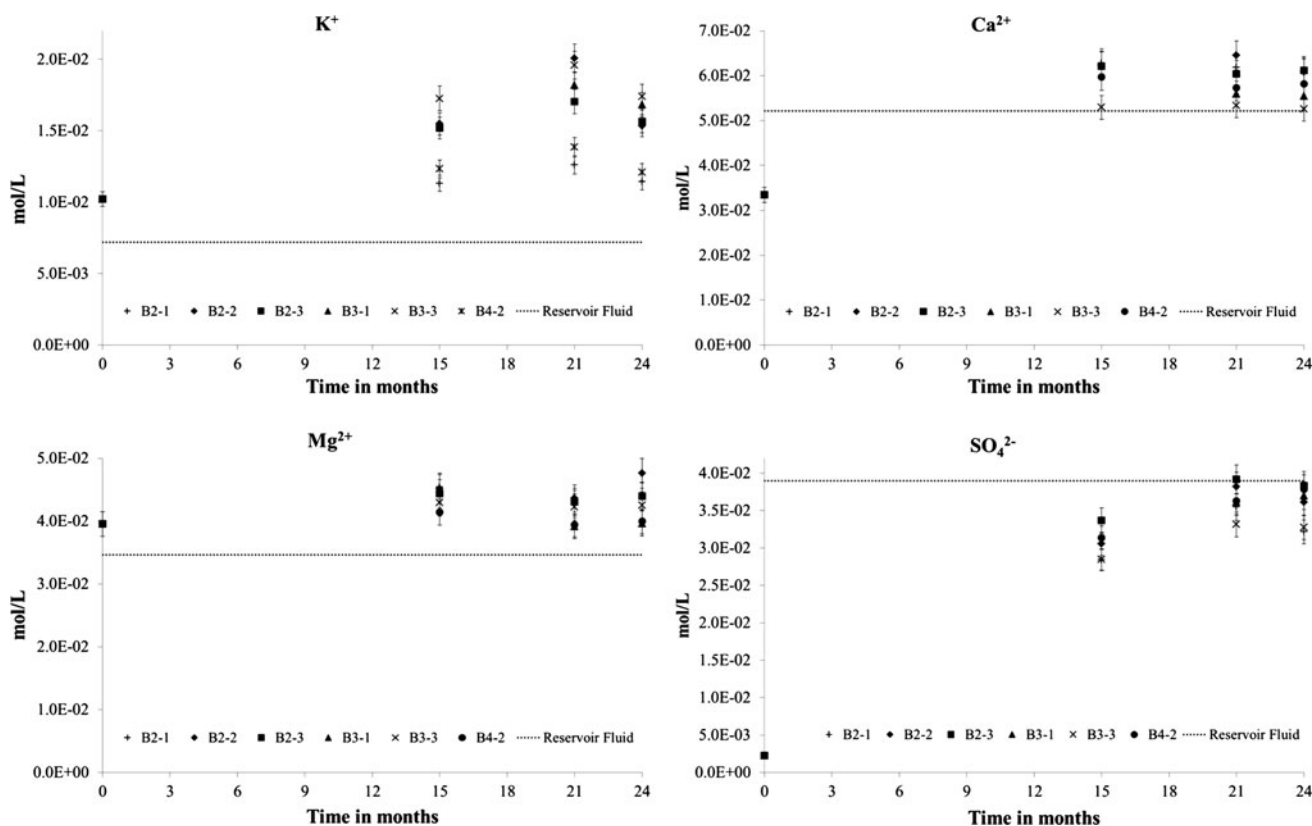
Fig. 8 Fluid data of the sandstone experiment as determined by ICP-AES and ion chromatography. Ion concentrations generally increase during the experiments. 5 % *error bars* are plotted. Note that for B3-1 the sample taken after 15 months was lost during analysis

sample are equal within analytical error. The Mg^{2+} concentration of the N_2-blank brine (3.7e−2 mol/L) is equal within analytical error to that of the initial brine sample (3.6e−2 mol/L), but significantly lower than in the CO_2-treated samples (4.5–4.9e−2 mol/L).

Geochemical modeling

The CO_2-independent equilibrium model EQUI-MOD_1 suggests that albite, anhydrite, hematite, and illite precipitate, while the remaining mineral phases would dissolve in case total equilibrium was attained. Analcime and chamosite-7A would completely dissolve to be still undersaturated at the end of the simulation. Other major effects during equilibration are substantial dissolution of quartz (−0.92 mol) and anorthite (−0.20 mol). Increased Ca^{2+} (+0.21 mol) and decreased Na^+ (−0.39 mol) are most significant changes regarding brine composition.

While K^+, Fe^{2+}, Al^{3+}, Si^{4+}, and SO_4^{2-} are generally rather difficult to match simultaneously in the set of EQUI-MOD_2 simulations, Na^+, Ca^{2+}, Mg^{2+}, and Cl^- show good matches with only minor differences between distinct simulations (Figs. 10, 11). The boxplots of the logarithmic differences between modeled and measured values in Fig. 11 show that a fine matching for Na^+ and Cl^- is

achieved during the complete set of EQUI-MOD_2 simulations, while the variability of other elements, such as Fe^{2+} and Al^{3+}, can span over several orders of magnitude. The simulations generally best matching the measured brine ion concentrations (Fig. 10; Table 5) comprise mineral combinations of albite, analcime, anhydrite, dolomite, hematite, illite, and kaolinite; the overall best match is gained by the model comprising albite, anhydrite, dolomite, hematite, and illite (Table 5).

The measured Mg^{2+} brine concentration of 4.3e−2 mol/L after 24 months was well reproduced by KIN-MOD_2.3 (4.3e−2 mol/L), KIN-MOD_1 (4.4e−2 mol/L) and KIN-MOD_2.2 (4.1e−2 mol/L). However, the Mg^{2+} increase from initial to final measurements is not covered by the modeling results. Calcium shows relatively good matches between measured (5.8e−2 mol/L) and modeled brine concentrations for KIN-MOD_2.6 (4.9e−2 mol/L), KIN-MOD_2.3 (6.6e−2 mol/L) and KIN-MOD_1 (7.2e−2 mol/L). Modeled SO_4^{2-} concentrations are generally in acceptable agreement with the measured data. While measured SO_4^{2-} concentrations of 3.6e−2 mol/L are well matched by KIN-MOD_1 (3.6e−2 mol/L) after 24 months, KIN-MOD_2.5 (3.5e−2 mol/L) and KIN-MOD_2.3 (3.7e−2 mol/L), the (initial) increase of measured SO_4^{2-} concentrations is much slower than the modeled one

Fig. 9 Fluid data of the siltstone experiment as determined by ICP-AES. Ion concentrations typically increase during the experiment. No significant differences between CO_2-treated samples and N_2 blank are apparent. Only Mg^{2+} has significantly higher concentrations in the CO_2-treated samples compared to both untreated and N_2 blank. 5 % *error bars are plotted*
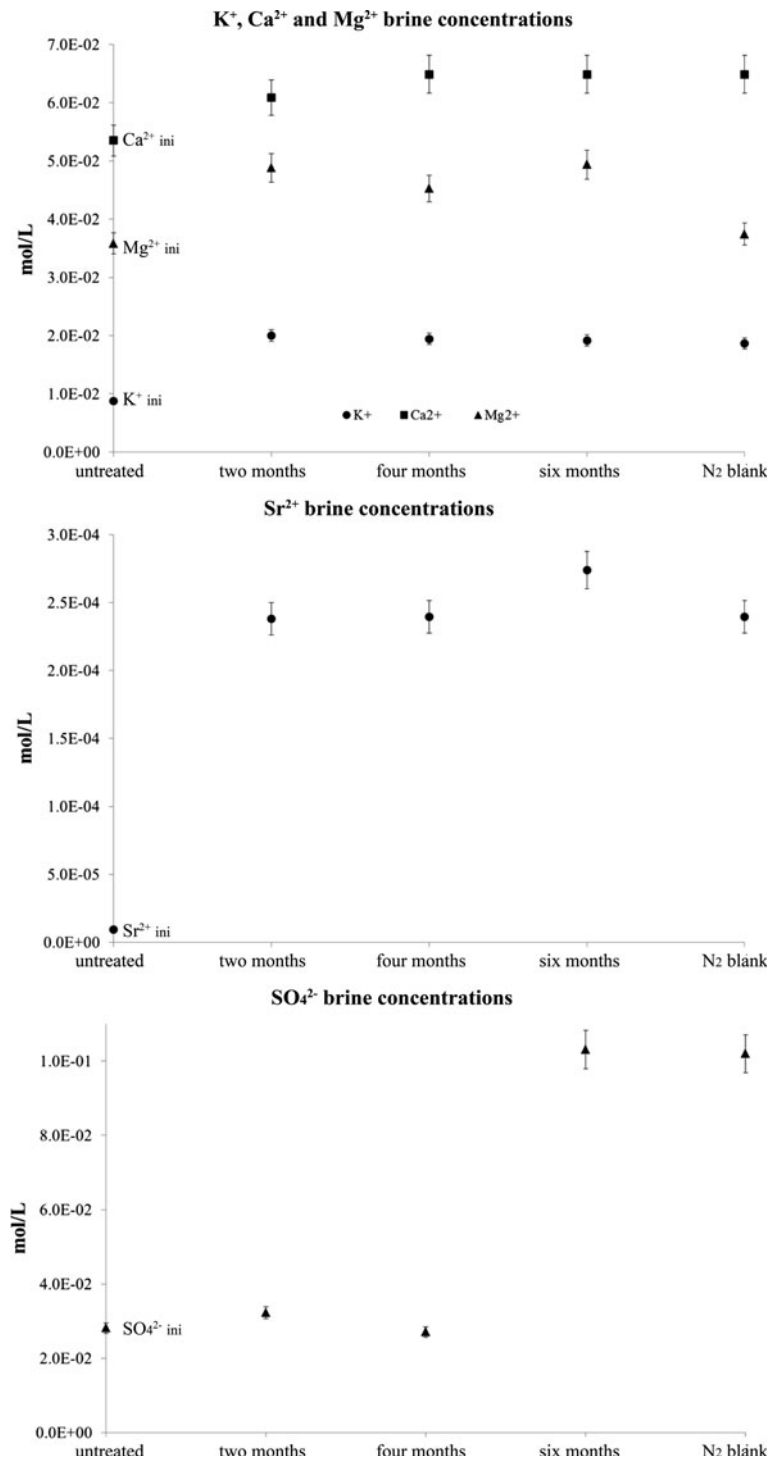
(Fig. 12). The kinetic models generally show a large mismatch to the measured K^+ brine concentration of 1.5e−2 mol/L. Closest matches of 1.1e−2 mol/L result from KIN-MOD_1, KIN-MOD_2.1, 2.3 and 2.4. Even more, the kinetically simulated K^+ concentrations do not only mismatch the increase in measured values, but some models even predict a strong decrease during 24 months to, e.g., 1.2e−5 mol/L K^+ in KIN-MOD_2.6. While the increasing

trend of measured Fe^{2+} brine concentrations was generally predicted by the kinetic models, absolute Fe^{2+} concentrations exhibit a significant mismatch (KIN-MOD_1: 4.5e−5 mol/L, KIN-MOD_2.3: 2.1e−6 mol/L and 2.2: 1.7e−6 mol/L) to the 4.2e−4 mol/L Fe^{2+} measured after 24 months (Fig. 12).

In KIN-MOD_1, anorthite shows decreasing abundances until the third month after CO_2 addition (2.84e−1 mol) and
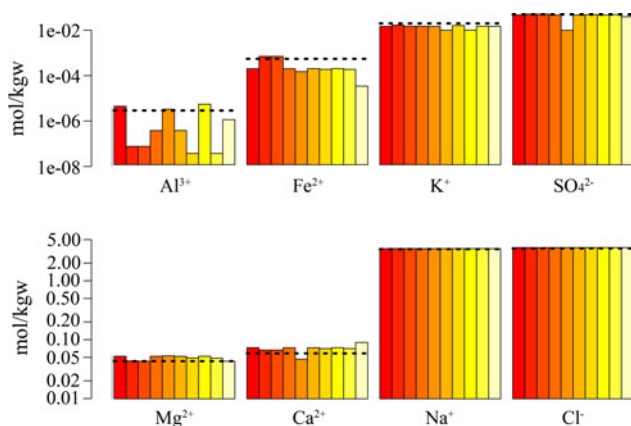
Fig. 10 Results of the set of EQUI-MOD_2 simulations showing the top 10 equilibrium models best matching with experimental data (*dashed lines*). Best model on the *left* in *red*
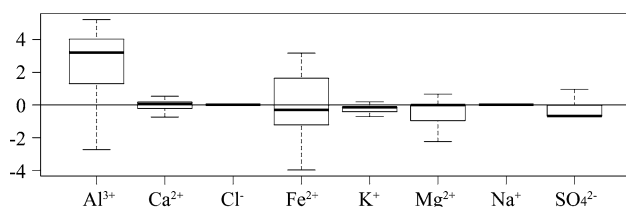

Fig. 11 *Box plots* of the results from EQUI-MOD_2 simulations showing the scatter in data with respect to distinct elements. It is apparent that Na^+ and Cl^- have the lowest, and Fe^{2+} and Al^{3+} the highest degree of uncertainty

constant levels thereafter. The decrease equals 0.17 g of dissolved anorthite. Dolomite and anhydrite abundances also decrease with time. Dolomite shows a rapid drop to 2.94e−2 mol within the first month. This is followed by a slight increase after 4 months and constant dolomite contents of 2.99e−2 mol to the end of the experiments. The decrease in dolomite abundance equals 0.02 g of dissolved dolomite. Anhydrite shows a rapid and sharp decrease within the first month and constant levels of 2.67e−2 mol after 4 months to the end. This decrease equals 0.46 g of anhydrite dissolution. The remainder minerals are unchanged in KIN-MOD_1. After 24 months, analcime, albite, illite_IMt-2, K-feldspar as well as kaolinite are strongly supersaturated. This implies that KIN-MOD_1 has not reached equilibrium after 24 months.

Anhydrite reveals dissolution in all simulations of KIN-MOD_2, but the amount of dissolved anhydrite varies between 3.2 and 5.2e−3 mol (0.44 and 0.71 g) in KIN-MOD_2.1 and 2.4, and KIN-MOD_2.6, respectively. While the amount of anhydrite is constant for the majority of simulations after the first month, only KIN-MOD_2.6 reveals continuous dissolution till the end. All simulations that include analcime show its dissolution. Again, the largest amount of −2.5e−3 mol (0.55 g) occurs during continuous analcime dissolution in KIN-MOD_2.6.

Dolomite is dissolved to a maximum of −1.1e−3 mol (0.20 g) in KIN-MOD_2.1. In KIN-MOD_2.6 dolomite initially dissolves (−3.9e−4 mol) during the first month, but finally 3.8e−3 mol (0.70 g) of dolomite precipitates after 24 months. Albite abundances are constant throughout the runs. Hematite is present in all six simulations of KIN-MOD_2 and uniformly reveals minor dissolution between 1.6e−8 and 3.2e−9 mol. In contrast to that, illite—if considered—shows minor precipitation between 8.9e−5 and 6.4e−7 mol in KIN-MOD_2.6 and KIN-MOD_2.1, respectively. All simulations indicate kaolinite precipitation that ranges from 1.7e−5 to 9.4e−3 mol (0.01–2.43 g) in KIN-MOD_2.4 and KIN-MOD_2.6. In the latter simulation, also 7.1e−5 mol (0.004 g) chalcedony precipitates.

Discussion

The mineralogical and geochemical data obtained from CO_2-exposure experiments on sandstone samples of the Stuttgart Formation at Ketzin indicate only minor changes. The sandstone experiments show that the overall variability between samples B2-1 to B4-2 is larger than that between untreated and CO_2-treated samples. Most minerals show variable abundances and no strictly uniform trend with time. Generally increased porosities (see below) and the overall trend of increasing TDS concentrations, however, clearly point towards dissolution processes during the sandstone experiments. Note that based on subsequent data of the original formation brine composition at Ketzin (which was not available at the start of the experiments; see above) the expected increase of fluid species occurred because the initial ion concentrations in the synthetic brine were below those of pristine reservoir brine reflecting the evolution of the synthetic brine to its potential equilibrium composition, even without any impact of CO_2. Consequently, the large increase in, e.g., SO_4^{2-} brine concentrations during the experiments is to a large extent due to CO_2-independent equilibration of the synthetic brine because only as little as 2.3e−3 mol/L SO_4^{2-} very initially present at the start of the experiments compared to 3.9e−2 mol/L SO_4^{2-} in the original reservoir brine. The CO_2-independent equilibration is also confirmed by EQUI-MOD_1, in which chemical reactions were triggered during equilibration of the CO_2-free synthetic brine with the initial mineral assemblage. Experimentally determined Ca^{2+}, K^+, and Mg^{2+} concentrations, however, clearly exceed pristine reservoir brine concentrations and inevitably indicate dissolution caused by added CO_2.

Sandstone porosities as determined by Zemke et al. (2010) during NMR measurements tendentially increase from top (B2-1) to the base (B4-2). While the untreated

Fig. 12 Molal concentrations of the kinetically modeled brine data in comparison to the measured concentrations (*red dots*) of the distinct elements
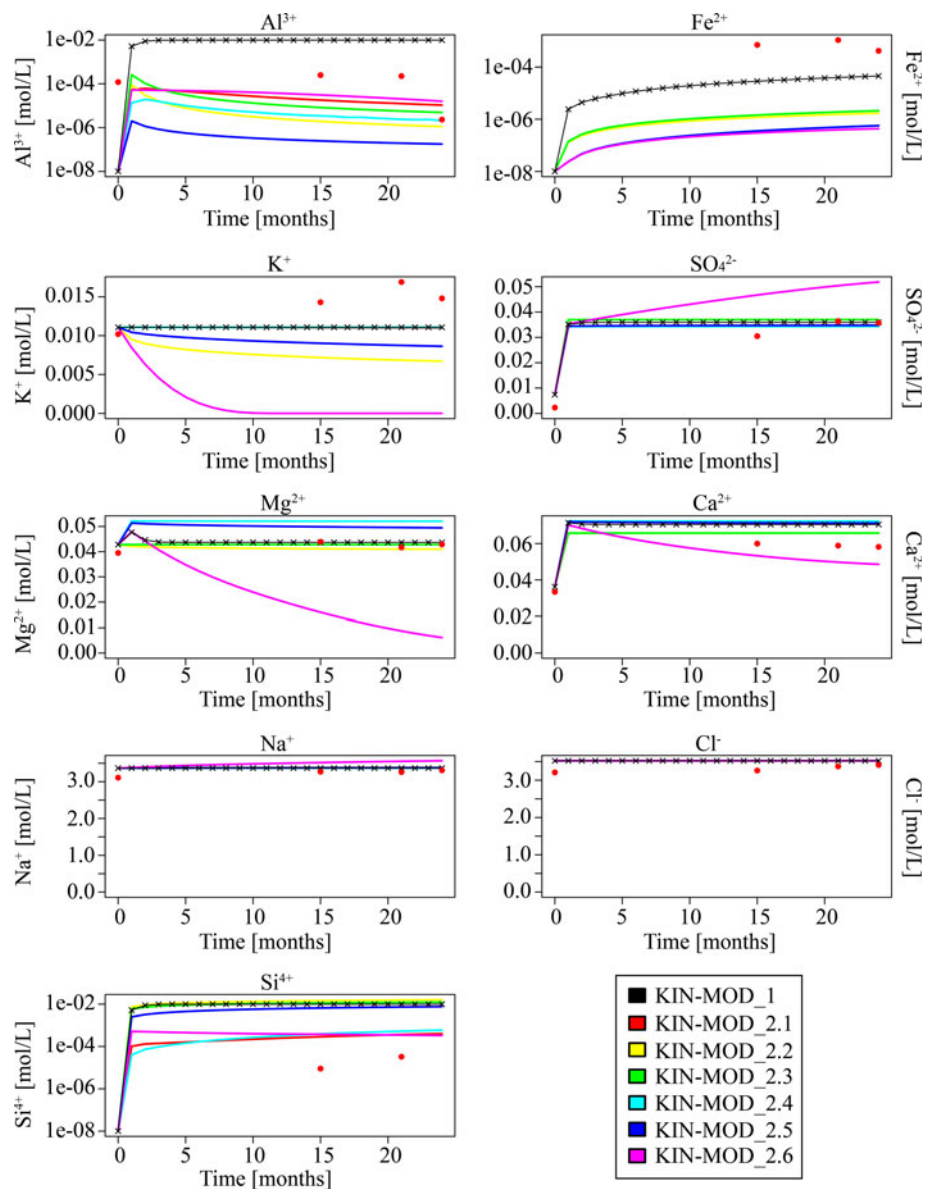
core sections B2-3, B3-1, B3-3, and B4-2 have porosities between 20.5 and 22.0 %, the core section B2-2 shows considerably lower porosity of 16.9 %; the untreated sample of core section B2-1 was unfortunately lost during preparation. In CO_2-treated samples porosities of core sections B2-3, B3-1, B3-3 and B4-2 increased to values between 24.4 and 31.3 %, and porosities of core sections B2-1 and B2-2 are between 7.3 and 17.5 %. The average porosity taken over the distinct subsets increased in the core sections B2-3, B3-1, B3-3, and B4-2 from 21.2 % in the untreated samples to 27.9 % in the samples treated for 15 months. Also core section B2-2 shows a slight increase from 16.9 to 17.5 % after 15 months.

The siltstone CO_2-exposure experiment illustrates only minor mineralogical-geochemical changes with run duration. Also compared to the N_2 blank only slight differences

are apparent. Contrary to the sandstone experiments mineral phases in the siltstone sample show variable abundances and no uniform trend with time. The reaction of the siltstone sample with synthetic brine and CO_2 is characterized by slightly increased TDS concentrations indicating mineral dissolution and mobilization of certain species. Except Mg^{2+}, all measured ions show similar brine concentration in CO_2- and N_2-treated samples suggesting CO_2-independent mineral-fluid equilibration processes. On the opposite, Mg^{2+} brine concentrations in the CO_2-treated fluid samples are significantly higher compared to those in untreated and N_2-treated fluid samples suggesting CO_2-related mineral-fluid processes. Although most ion concentrations increased with time kinetic rates of the underlying dissolution processes appear to be different. While K^+, Mg^{2+} and Sr^{2+} reach constant concentration

levels within 2 months, Ca^{2+} brine concentration is constant after 4 months, and SO_4^{2-} reveals highest brine concentrations only after 6 months. Sodium and Cl^- concentrations in untreated, CO_2- and N_2-treated fluid samples are constant within analytical error.

In sandstone as well as in siltstone experiments, surfaces of plagioclase grains show corrosion and etching textures, which intensify with run duration. Increased Ca^{2+} (and Na^+) concentrations in the sampled brine also point to dissolution of (Na-)Ca-plagioclase. Rietveld refined plagioclase abundances, however, do not show a distinct trend. Note that corrosion textures on plagioclase grains similar to those described above next to albite end-member compositions associated with albitization of plagioclase (and K-feldspar) were also described by Förster et al. (2010) during baseline characterization of the Stuttgart Formation. But as (1) plagioclase grains with fresh and unaltered surfaces were only found in untreated samples, and (2) corrosion textures intensified with run duration, alteration of plagioclase due to the presence of CO_2 is strongly suggested through both experiments. Sodic plagioclase is, however, more stable compared to intermediate or calcic plagioclase. This is also supported by geochemical modeling of the sandstone experiment. In KIN-MOD_1 Ca^{2+} (and Na^+) brine concentration increases and anorthite abundance decreases, whereas the abundance of albite remains unchanged. Furthermore, it is known from literature that calcic plagioclase has higher weathering rates in acidic environments compared to sodic plagioclase (e.g. Blum and Stillings 1995).

Corroded surfaces of K-feldspar grains from CO_2-treated sandstone and siltstone samples next to increased K^+ brine concentrations indicate dissolution of K-feldspar during both experiments. K-feldspar abundances, however, do not show a distinct trend with time and dissolution pits and etch textures were also found on few untreated K-feldspar grains. As also the fate of illite is uncertain during the experiments and illite precipitation with constant or even decreasing K^+ brine concentrations are indicated during modeling (see below), this qualitative contradiction between increased K^+ brine concentrations and corrosion textures on experimentally treated K-feldspars and supersaturation of K-feldspar (and illite) predicted from the models cannot be resolved here. However, our results clearly suggest that dissolution of quantitatively relevant amounts of K-feldspar is unlikely during the sandstone experiments. It is noteworthy that K-feldspar dissolution has been described in other reservoir sandstones both from natural CO_2 accumulations and from batch and flow-through experiments. While Pauwels et al. (2007) found clear signs of K-feldspar alteration in line with increased K^+ brine contents studying the Montmiral CO_2 analog in France, Czernichowski-Lauriol et al. (1996)

describe K-feldspar corrosion in Lower Triassic Sherwood Sandstones that were experimentally treated with CO_2. To date no explanation for the uniform decrease of K^+ brine concentrations in fluid samples between 21 and 24 months is at hand. Despite the fact that no new formed K-bearing mineral was found, it can be expected that K^+ is incorporated into clay minerals (e.g. illite) that typically form during feldspar weathering. Clay mineral colloid suspensions were observed in brine samples of both experiments. These clogged the filters used to clean the fluids after sampling and it is highly probable that these clays also contained K^+—amongst cations like Mg^{2+}, Al^{3+}, Si^{4+}.

Corrosion textures on anhydrite surfaces of CO_2-treated samples as well as increased SO_4^{2-} brine concentrations clearly point to anhydrite dissolution during both experiments. Note that anhydrite is the only quantitatively relevant sulfur/sulfate-source in both rocks. Anhydrite occurs in all untreated sandstone samples, but was not detected in any subsets of samples B3-1, B3-3, and B4-2, respectively. Sample sets B2-1, B2-2, and B2-3 do not show a consistent trend for anhydrite abundances with run time; a fact mainly attributable to the heterogeneous, poikilitic distribution of anhydrite cement. Anhydrite dissolution during the sandstone experiments is at least partially related to brine-rock equilibration caused by SO_4^{2-} undersaturation in the initial synthetic brine. The simulated equilibrium model (EQUI-MOD_1) between synthetic brine and mineral assemblage (without CO_2) also shows increased SO_4^{2-} brine concentrations due to anhydrite dissolution. Based on fluid data of sandstone experiments between 2.4 and 3.9e−3 mol/L Ca^{2+} and between 3.3 and 4.6e−3 mol/L SO_4^{2-} were added to the brine, respectively. The average dissolved SO_4^{2-} increase is about 1.3 times higher than that of the average dissolved Ca^{2+} increase and about 8.1e−4 mol/L Ca^{2+} must hence have precipitated in a solid, yet undetected phase (possibly carbonate) again. Assuming that the SO_4^{2-} increase is solely caused by anhydrite dissolution between 0.45 and 0.64 g anhydrite dissolved within 24 months of CO_2 exposure.

In a core-flooding laboratory study on Tensleep reservoir sandstone (Wyoming, USA), Shiraki and Dunn (2000) observed dissolution of anhydrite in experiments using 0.25 M NaCl brine, on the one hand, but anhydrite precipitation during experiments using a mixed Ca–Mg–Na–SO_4–Cl brine, which had been pre-saturated with respect to anhydrite, on the other. Their findings also support the argument of anhydrite dissolution during the here performed sandstone experiments (mainly) due to the SO_4^{2-} deficit in the initial synthetic brine. In the siltstone experiments, SO_4^{2-} brine concentrations are unchanged during the first 4 months, but increase rapidly within the following 2 months of CO_2 treatment. Considering anhydrite as the major source of SO_4^{2-} also in the siltstone sample,

anhydrite dissolution starts between month 4 and 6 after CO_2 addition. Note that despite minor increases in Sr^{2+} brine concentrations (see below), which could be caused by dissolving $(Ba,Sr)SO_4$ solid solutions, no (other) data indicate alteration of respective minerals. The SO_4^{2-} increase in the sampled brine of the siltstone experiment is about 6.5 times higher than the Ca^{2+} increase. Hence, about 0.06 mol/L Ca^{2+} must have precipitated in a solid, yet undetected phase (possibly carbonate) again. Under the assumption that all SO_4^{2-} derived from anhydrite dissolution, 0.57 g anhydrite were dissolved from the siltstone sample. The N_2 blank shows a similar SO_4^{2-} brine concentration compared to that of the CO_2-treated sample taken after 6 months. As the N_2-blank siltstone sample has significantly higher anhydrite abundance, the comparable SO_4^{2-} brine concentrations indicate equilibrium concentrations. The increase in Sr^{2+} brine content is distinct, but only minor (2.6e−4 mol/L Sr^{2+}). Similar Sr^{2+} brine concentration increases were also found in the experiments on Stuttgart Formation sandstone, in which no $(Ba,Sr)SO_4$ solid solutions were detected. The Sr^{2+} increases may also be caused by the dissolution of anhydrite, which can accommodate up to 1200 ppm Sr^{2+} as detected in the siltstone sample of the present study, and as much as 1,800 ppm Sr^{2+} as determined by Förster et al. (2010) for the Stuttgart Formation.

Decreasing analcime, chlorite + biotite, and hematite abundances indicate dissolution of the respective minerals caused by chemical equilibration during the sandstone experiments. Dissolution of analcime is in contrast to findings by Kaszuba et al. (2005) who observed decreasing Na^+ brine concentrations as well as euhedral analcime crystals during coupled arkose–shale CO_2-exposure experiments. The authors conclude that analcime formed as an equilibrium phase. In the presented study changes in Na^+ brine concentrations are minor, analcime surfaces do not show any signs of dissolution in both experiments but potential dissolution of analcime is indicated by XRD data obtained from the sandstone experiments (see above). The dissolution of analcime is also supported by geochemical modeling. Note, however, that analcime is only modeled as an equilibrium phase since no kinetic data are available.

The experimental data suggest chlorite and/or biotite dissolution during the experiments. The observed increase of Mg^{2+} brine concentrations in both experiments is probably due to incongruent (non-stoichiometric) dissolution of 2:1 sheet silicates in line with findings by Nagy (1995) who showed that the release rate for sheet silicates in acidic to neutral solutions is greatest for Mg-octahedral sheets. Chlorite/chamosite dissolution as a consequence of reaction of rock with CO_2-rich brine has also been described in flow-through experiments using chlorite/zeolite-rich sandstones from Pretty Hill Formation (Otway

Basin, Australia) by Luquot et al. (2012). The authors describe corrosion textures on chlorite/chamosite surfaces and also link increased Mg^{2+} and Fe^{2+} concentrations in experimentally sampled brine to chamosite dissolution. However, stable chlorite/clinochlore was observed by Liu et al. (2012), who performed batch experiments on Eau Claire shale from Indiana, USA. Although both the sandstone and siltstone experiments reveal increased Mg^{2+} brine concentrations that could be related to chlorite/chamosite dissolution, the trend of decreasing chlorite abundances in the sandstone samples is not uniform and differences between distinct samples are apparent. Sample B4-2, e.g., shows slightly higher chlorite + biotite abundances to the end of the experiments. Note that most changes in chlorite + biotite abundances as determined by Rietveld refinements are within analytical error. Chloritization and/or dissolution of biotite may also explain increased K^+ brine concentrations during both experiments. However, neither lower K^+ nor lower total weight percentages oxides—as typically associated with chloritization of biotite—have been unequivocally observed in both experiments.

Increased Fe^{2+} brine concentrations in samples B3-1 and B4-2, which have the highest initial hematite abundances of all samples, together with decreased modal hematite abundances to the end of the experiments clearly point to hematite dissolution. The tendentially decreasing hematite abundance in sample B2-1 is also suggestive of hematite dissolution although the trend is not that clear as in samples B3-1 and B4-2. Samples B2-2, B2-3, and B3-3 are characterized by comparatively low Fe^{2+} brine concentrations and also constant or slightly increased hematite abundances during the experiments, so the results from these experiments are equivocal with respect to hematite dissolution or precipitation. The suggested hematite dissolution is consistent with results by Murphy et al. (2011), Palandri and Kharaka (2005) and Palandri et al. (2005), who likewise found hematite dissolution in CO_2-rich and aqueous sulfide bearing fluid-mineral systems. However, Schoonen et al. (2011) did not observe any change of hematite abundance in crushed Moenkopi sandstone from Flagstaff, Arizona (USA) during CO_2-charged batch as well as flow-through experiments.

Geochemical modeling

Highly complex and variable natural media can only be partially simulated and described by numerical models, especially when geochemical reactions in deep formations with high salinity fluids are investigated (e.g. Gaus 2010). The high ionic strength of the solutions in the sandstone experiments requires the adoption of a well-suited activity model such as that proposed by Pitzer (1973). However,

Pitzer-based thermodynamic databases are incomplete especially concerning aluminosilicates and redox-sensitive reactions, so that many modelers prefer to use more standard—and more validated, at least for low ionic strengths—Debye–Hückel models. Taking into account mineral reaction kinetics, however, helps limiting the influence of the underlying chemical database. Further sources of significant inaccuracies for the modeling are the necessary simplifications of natural media in "pure" mineral phases (e.g. albite and anorthite; no intermediate plagioclase), and, for reaction kinetics, the quantification of the reactive surface areas.

The modeling part of this study focused on matching the experimental observations. The comparison of databases, a thorough sensitivity and uncertainty analysis or more accurate inverse modeling combined with calibration of kinetic parameters, is beyond the scope of this paper. Nonetheless, the results of rather simplified models assuming local equilibrium and also considering reaction kinetics are in relatively good agreement with the observations obtained from the sandstone experiments. Namely, the experimental concentrations of major ions are matched by the models. The only systematic discrepancies—corresponding to qualitative differences between experiments and modeling—occur regarding dissolved K^+, Fe^{2+} and Al^{3+}; Fe^{2+} being also quite variable in the sandstone experiments (see above). A possible reason for this discrepancy can be ascribed to the quality of the underlying thermodynamic database, especially with regard to possibly imprecise data (such as respective solubility products) for K- and Fe-bearing phases, but also to the choice of the mineral phase taken as proxy for illite. Moreover, probable chloritization and/or dissolution of biotite, as well as Na^+/K^+ ion exchange in clay minerals are processes not covered during modeling and may explain the mismatch for dissolved K^+. Iron species are furthermore redox sensitive, but as redox reactions are only partially incorporated into the selected database, this circumstance also leads to incomplete results. Another source of uncertainty with regard to iron species is associated with iron oxi(hydroxi)de coatings that could possibly be mobilized during CO_2-exposure experiments. These are generally rather difficult to incorporate into geochemical models also because of being inherently difficult to identify and quantify within bulk rock samples.

In the simulations considering kinetic rate laws, reactions hardly reached equilibrium for most input minerals (SI $\approx \pm 2$) and most models after 24 months of CO_2 exposure. KIN-MOD_1 is still far from equilibrium at the end of the simulation period (SI $\gg 0$ for albite, analcime, illite, K-feldspar and kaolinite), and anorthite and hematite are strongly undersaturated (SI $\ll 0$) in the distinct models of KIN-MOD_2. Nonetheless, equilibrium as well as

kinetic models are able to unravel the ongoing geochemical processes. The equilibrium model best matching with experimental observations comprises albite, anhydrite, dolomite, hematite and illite. It is noteworthy that only KIN-MOD_2.6 predicts mineral carbonation in the form of 0.70 g dolomite precipitation. Quartz was generally considered inert during kinetic modeling; a consideration confirmed by KIN-MOD_2.6, in which chalcedony was incorporated as a SiO_2 proxy based on generally very similar SI values for both chalcedony and quartz, and respective results show relatively large mismatches with experimental brine data.

Note that hematite is strongly undersaturated in the kinetic simulations but does not show significant dissolution due to kinetic limitation; a fact that possibly also explains the discrepancy with respect to the equilibrium models, which consider the same mineral assemblage. This furthermore points towards a possible need of re-parametrization of the associated kinetic rate law.

Conclusions

The experimental data clearly show that CO_2 exposure triggers dissolution of the anorthite component of plagioclase, K-feldspar, anhydrite but stabilizes the albite component of plagioclase. By trend decreasing mineral abundances also suggest dissolution of analcime and chlorite + biotite. However, no other direct evidence for dissolution was found for these minerals. Also hematite abundances tendentially decrease in line with increasing Fe^{2+} brine concentrations strongly suggesting hematite dissolution. Trends in mineral abundances and the quantification of dissolution processes are generally difficult to determine due to the pre-experimental heterogeneity of the samples and pre-existing, diagenetic alteration. No precipitation of secondary minerals, such as carbonates, was observed. This is supported by modeling results as only one single model predicts precipitation of minor amounts of dolomite within 24 months. Initial equilibrium models confirmed CO_2-independent reactions caused by the experimentally used synthetic brine. During inverse equilibrium modeling good matches with experimental data were reached for Na^+, Ca^{2+}, Mg^{2+}, and Cl^-; major mismatches are obtained for Fe^{2+} and Al^{3+}. By considering quartz as inert during sandstone experiments, the equilibrium model best matching the measured brine data comprises albite, anhydrite, dolomite, hematite, and illite. The evolution of brine data during the sandstone experiments were also well matched by kinetic simulations; major discrepancy being reactions involving K- and Fe-bearing minerals. The contradiction between increased K^+ brine concentrations and corrosion textures on experimentally

treated K-feldspars and supersaturation of K-feldspar (and illite) predicted by the models cannot be resolved here. The modeling approach illustrates that key primary minerals and fundamental chemical processes of the sandstone experiment could be identified, but also that the modeling is not capable of covering the complete range of natural variability. In summary it can be said that the models show dissolution of the anorthite component of plagioclase and cement phases (analcime, anhydrite, dolomite), and precipitation of clay minerals (chlorite, illite, kaolinite).

References

Bachu S, Gunter WD, Perkins EH (1994) Aquifer disposal of CO2: hydrodynamic and mineral trapping. Energy Convers Manag 35:269–279

Bateman K, Turner G, Pearce JM, Noy DJ, Birchall D, Rochelle CA (2005) Large-scale column experiment: study of CO2, porewater, rock reactions and model test case. Oil Gas Sci Technol Rev IFP 60(1):161–175

Benbow S, Metcalfe R, Wilson J (2008) Pitzer databases for use in thermodynamic modeling. Quintessa Technical Memorandum (unpublished)

Blum AE, Stillings LL (1995) Feldspar dissolution kinetics. In: White AF, Brantley SL (eds) Chemical weathering rates of silicate minerals. Mineralogical Society of America, Washington, DC, pp 291–351

Cantucci B, Montegrossi G, Vaselli O, Tassi F, Quattrocchi F, Perkins EH (2009) Geochemical modeling of CO2 storage in deep reservoirs: the Weyburn Project (Canada) case study. Chem Geol 265(1–2):181–197

Czernichowski-Lauriol I, Sanjuan B, Rochelle C, Bateman K, Pearce JM, Blackwell P (1996) Inorganic geochemistry. In: Holloway S (ed) Final report of the Joule II project No. CT92-0031: The underground disposal of carbon dioxide. British Geological Survey, Keyworth, pp 183–276

Czernichowski-Lauriol I, Rochelle C, Gaus I, Azaroual M, Pearce J, Durst P (2006) Geochemical interactions between CO2, pore-water and reservoir rock. Adv Geol Storage Carbon Dioxide 65:157–174

De Lucia M, Bauer S, Beyer C, Kühn M, Nowak T, Pudlo D, Reitenbach V, Stadler S (2012) Modeling CO2-induced fluid—rock interactions in the Altensalzwedel gas reservoir Part I: from experimental data to a reference geochemical model. Environ Earth Sci 67(2):563–572

Driesner T (2007) The system H2O–NaCl. Part II. Correlations for molar volume, enthalpy, and isobaric heat capacity from 0 to 1000 °C, 0 to 5000 bar, and 0 to 1 X_{NaCl}. Geochim Cosmochim Acta 71:4902–4919

Driesner T, Heinrich CA (2007) The system H2O–NaCl. Part I. Correlation formulae for phase relations in temperature–pressure-composition space from 0 to 1000 °C, 0 to 5000 bar, and 0 to 1 X_{NaCl}. Geochim Cosmochim Acta 71:4880–4901

Fischer S, Liebscher A, Wandrey M (2010) CO2-brine-rock interaction – First results of long-term exposure experiments at in situ P–T conditions of the Ketzin CO2 reservoir. Chemie der Erde/Geochem 70(3):155–164

Fischer S, Zemke K, Liebscher A, Wandrey M (2011) Petrophysical and petrochemical effects of long-term CO2-exposure experiments on brine-saturated reservoir sandstone. Energy Procedia 4:4487–4494

Förster A, Norden B, Zinck-Jørgensen K, Frykman P, Kulenkampff J, Spangenberg E, Erzinger J, Zimmer M, Kopp J, Borm G, Juhlin C, Cosma C, Hurter S (2006) Baseline characterization of the CO2SINK geological storage site at Ketzin, Germany. Environ Geosci 133:145–161

Förster A, Schöner R, Förster H-J, Norden B, Blaschke A-W, Luckert J, Beutler G, Gaupp R, Rhede D (2010) Reservoir characterization of a CO2 storage aquifer: The Upper Triassic Stuttgart Formation in the Northeast German Basin. Mar Pet Geol 27(10):2156–2172

Gailhanou H, van Miltenburg J, Rogez J, Olives J, Amouric M, Gaucher E, Blanc P (2007) Thermodynamic properties of anhydrous smectite mx-80, illite imt-2 and mixed-layer illite smectite iscz-1 as determined by calorimetric methods. Part I: heat capacities, heat contents and entropies. Geochim Cosmochim Acta 71(22):5463–5473

Gaus I (2010) Role and impact of CO2-rock interactions during CO2 storage in sedimentary rocks. Int J Greenh Gas Control 4:73–89

Gaus I, Azaroual M, Czernichowski-Lauriol I (2005) Reactive transport modeling of the impact of CO2 injection on the clayey cap rock at Sleipner (North Sea). Chem Geol 217:319–337

Gunter WD, Perkins EH, McCann TJ (1993) Aquifer disposal of CO2-rich gases: reaction design for added capacity. Energy Convers Manag 34:941–948

Hitchon B, Gunter WD, Gentzis T, Bailey RT (1999) Sedimentary basins and greenhouse gases: a serendipitous association. Energy Convers Manag 40:825–843

Holloway S (1997) An overview of the underground disposal of carbon dioxide. Energy Convers Manag 38:193–198

IPCC (2005) Intergovernmental panel on climate change special report on carbon dioxide capture and storage. Cambridge University Press, New York

Jarosewich E, Nelen JA, Norberg JA (1980) Reference samples for electron microprobe analysis. Geostand Newsl 4:43–47

Kaszuba JP, Janecky DR, Snow MG (2003) Carbon dioxide reaction processes in a model brine aquifer at 200 °C and 200 bars: implications for geologic sequestration of carbon. Appl Geochem 18:1065–1080

Kaszuba JP, Janecky DR, Snow MG (2005) Experimental evaluation of mixed fluid reactions between supercritical carbon dioxide and NaCl brine: relevance to the integrity of a geologic carbon repository. Chem Geol 217:277–293

Kempka T, Kühn M (2013) Numerical simulations of CO2 arrival times and reservoir pressure coincide with observations from the Ketzin pilot site, Germany. Environ Earth Sci. doi:10.1007/s12665-013-2614-6

Klein E, De Lucia M, Kempka T, Kühn M (2013) Evaluation of long-term mineral trapping at the Ketzin pilot site for CO2 storage: an integrative approach using geochemical modeling and reservoir simulation. IJGGC. doi:10.1016/j.ijggc.2013.05.014

Köhler SJ, Dufaud F, Oelkers EO (2003) An experimental study of illite dissolution kinetics as a function of pH from 1.4 to 12.4 and temperature from 5 to 50°C. Geochim Cosmochim Acta 67:3583–3594

Lasaga AC (1984) Chemical kinetics of water–rock interactions. J Geophys Res 89(B6):4009–4025

Lasaga AC (1995) Fundamental approaches to describing mineral dissolution and precipitation rates. Rev Mineral 31:23–86

Liu F, Lu P, Griffith C, Hedges SW, Soong Y, Hellevang H, Zhu C (2012) CO$_2$-brine-caprock interaction: reactivity experiments on Eau Claire shale and a review of relevant literature. Int J Greenh Gas Control 7:153–167

Luquot L, Andreani M, Gouze P, Camps P (2012) CO$_2$ percolation experiment through chlorite/zeolite-rich sandstone (Pretty Hill Formation, Otway Basin, Australia). Chem Geol 294–295:75–88

Martens S, Kempka T, Liebscher A, Lüth S, Möller F, Myrttinen B, Norden B, Schmidt-Hattenberger C, Zimmer M, Kühn M (2012) Europe's longest-operating on-shore CO$_2$ storage site at Ketzin, Germany: a progress report after three years of injection. Environ Earth Sci 67(2):323–334

Martens S, Liebscher A, Möller F, Henninges J, Kempka T, Lüth S, Norden B, Prevedel B, Szizybalski A, Zimmer M, Kühn M (2013) CO$_2$ storage at the Ketzin pilot site, Germany: fourth year of injection, monitoring, modelling and verification. Energy Procedia (in press)

Michael K, Golab AV, Shulakova V, Ennis-King JG, Allinson G, Sharma S, Aiken TT (2010) Geological storage of CO$_2$ in saline aquifers—a review of the experience from existing storage operations. Int J Greenh Gas Control 4:659–667

Moore J, Adams M, Allis R, Lutz S, Rauzi S (2005) Mineralogical and geochemical consequences of the long-term presence of CO$_2$ in natural reservoirs: an example from Springerville-St. Johns Field, Arizona, and New Mexico. USA. Chem Geol 217:365–385

Murphy R, Lammers K, Smirnov A, Schoonen MAA, Strongin DR (2011) Hematite reactivity with supercritical CO$_2$ and aqueous sulfide. Chem Geol 283:210–217

Nagy KL (1995) Dissolution and precipitation kinetics of sheet silicates. Rev Mineral 31:173–233

Palandri JL, Kharaka YK (2004) A compilation of rate parameters of water-mineral interaction kinetics for application to geochemical modeling. US Geological Survey Water-Resources Investigations, Open File Report 2004-1068

Palandri JL, Kharaka YK (2005) Ferric iron-bearing sediments as a mineral trap for CO$_2$ sequestration: iron reduction using sulfur-bearing waste gas. Chem Geol 217(3–4):351–364

Palandri JL, Rosenbauer RJ, Kharaka YK (2005) Ferric iron in sediments as a novel CO$_2$ mineral trap: CO$_2$–SO$_2$ reaction with hematite. Appl Geochem 20(11):2038–2048

Parkhurst DL, Appelo CAJ (1999) User's guide to PHREEQC (version 2)-A computer program for speciation, batch-reaction, one-dimensional transport, and inverse geochemical calculations. U.S. Geological Survey Water-Resources Investigations Report 99–4259

Pauwels H, Gaus I, Michel le Nindre Y, Pearce J, Czernichowski-Lauriol I (2007) Chemistry of fluids from a natural analogue for a geological CO$_2$ storage site (Montmiral, France): lessons for CO$_2$–water–rock interaction assessment and monitoring. Appl Geochem 22:2817–2833

Pettijohn FJ, Potter PE, Siever R (1987) Sand and sandstones. Springer, New York

Pitzer K (1973) Thermodynamics of electrolytes. I. Theoretical basis and general equations. J Phys Chem B 77(2):268–277

Prevedel B, Wohlgemuth L, Henninges J, Krüger K, Norden B, Förster A, CO2SINK Drilling Group (2008) The CO2SINK boreholes for geological storage testing. Sci Drill 6:32–37

Rochelle CA, Birchall DJ, Bateman K (2002) Geochemical interaction between supercritical CO$_2$ and the Midale formation. I: introduction to fluid–rock interaction experiments. British Geological Survey Commissioned Report Cr/02/289

Rochelle CA, Czernichowski-Lauriol I, Milodowski AE (2004) The impact of chemical reactions on CO$_2$ storage in geological formations: a brief review. In: Baines SJ, Worden RH (eds) Geological storage of carbon dioxide, vol 233. Geological Society, Special Publications, London, pp 87–106

Rosenbauer RJ, Koksalan T, Palandri JL (2005) Experimental investigation of CO$_2$–brine–rock interactions at elevated temperature and pressure: implications for CO$_2$ sequestration in deep-saline aquifers. Fuel Proc Technol 86:1581–1597

Rosenqvist J, Kilpatrick AD, Yardley BWD (2012) Solubility of carbon dioxide in aqueous fluids and mineral suspensions at 294 K and subcritical pressures. Appl Geol 27:1610–1614

Sass BM, Gupta N, Ickes JA, Engelhard MH, Baer DR, Bergman P, Byrer C (1999) Interaction of rock minerals with carbon dioxide and brine: a hydrothermal investigation. In: Conference PROCEEDINGS CD, 1st national conference on carbon sequestration, Washington, DC

Schoonen MAA, Sklute EC, Dyar MD, Strongin DR (2011) Reactivity of sandstones under conditions relevant to geosequestration: 1. Hematite-bearing sandstone exposed to supercritical carbon dioxide with aqueous sulfite or sulfide solutions. Chem Geol 296–297:96–102

Shiraki R, Dunn TL (2000) Experimental study on water–rock interactions during CO$_2$ flooding in the Tensleep Formation, Wyoming, USA. Appl Geochem 15:265–279

Smyth RC, Hovorka SD, Lu J, Romanak KD, Partin JW, Wong C, Yang C (2009) Assessing risk to fresh water resources from long term CO$_2$ injection—laboratory and field studies. Energy Procedia 1:1957–1964

Wandrey M, Pellizari L, Zettlitzer M, Würdemann H (2011) Microbial community and inorganic fluid analysis during CO$_2$ storage within the frame of CO2SINK—long-term experiments under in situ conditions. Energy Procedia 4:3651–3657

Watson MN, Zwingmann N, Lemon NM (2002) The Ladbroke Grove–Katnook carbon dioxide natural laboratory: a recent CO$_2$ accumulation in a lithic sandstone reservoir. Extended abstract E1-5, sixth international conference on greenhouse gas control technologies (GHGT-6), Kyoto, Japan, 6p, October 1–4

Wigand M, Carey JW, Schuett H, Spangenberg E, Erzinger J (2008) Geochemical effects of CO$_2$ sequestration in sandstones under simulated in situ conditions of deep saline aquifers. Appl Geochem 23:2735–2745

Wolery T (1992) Eq3/6, a software package for geochemical modeling of aqueous systems: Package overview and installation guide (version 7.0) ucrl-ma-110662. Technical Report, Lawrence Livermore National Laboratory

Würdemann H, Möller F, Kuehn M, Heidug W, Christensen NP, Borm G, Schilling FR, CO2Sink Group (2010) CO2SINK-From site characterisation and risk assessment to monitoring and verification: one year of operational experience with the field laboratory for CO$_2$ storage at Ketzin, Germany. Int J Greenh Gas Control 4:938–951

Wiese B, Zimmer M, Nowak M, Pilz P (submitted) Above-zone well-based hydraulic and geochemical monitoring of the CO$_2$ reservoir in Ketzin, Germany. Submitted to Environ Earth Sci

Zemke K, Liebscher A, Wandrey M, the CO2SINK Group (2010) Petrophysical analysis to investigate the effects of carbon dioxide storage in a subsurface saline aquifer at Ketzin, Germany (CO2SINK). Int J Greenh Gas Control 4:990–999

Zerai B, Saylor BZ, Matisoff G (2006) Computer simulation of CO$_2$ trapped through mineral precipitation in the Rose Run Sandstone, Ohio. Appl Geochem 21:223–240

6. Publication V:

"Does injected CO$_2$ affect (chemical) reservoir system integrity? – A comprehensive experimental approach"

GHGT-11

Does injected CO_2 affect (chemical) reservoir system integrity? – A comprehensive experimental approach

Sebastian Fischer[a,b,*], Axel Liebscher[a], Kornelia Zemke[a], Marco De Lucia[a], and the Ketzin Team

[a]Helmholtz Centre Potsdam, GFZ German Research Centre for Geosciences, Centre for CO_2 Storage, Potsdam, Germany
[b]Berlin Institute of Technology, School VI, Department of Applied Geosciences, Chair of Mineralogy-Petrology, Berlin, Germany

Abstract

In order to investigate and characterize single fluid-mineral interactions we successfully implemented a new hydrothermal laboratory. CO_2-exposure experiments using separates of rock-forming minerals were performed on a hydrothermal rocking autoclave. The system is equipped with flexible Titanium cells allowing for isobaric sampling. Experiments were run for one week at 80 °C and 20 MPa/30 MPa. Rietveld refined XRD data reveal that the initial siderite separate is composed of 69.6±1.3 wt% siderite, 26.7±1.2 wt% ankerite and 3.8±0.8 wt% quartz, respectively. Over time, siderite abundances increase and ankerite abundances correspondingly decrease, while quartz abundances are constant within error. Fluid data show rapid increases for Ca^{2+}, Mg^{2+}, Mn^{2+} and Fe^{2+}. After these rapid increases, Ca^{2+} and Mg^{2+} reveal slight decreases that are followed by subsequent rises to maximum concentrations at the end of the experiments, while Mn^{2+} and Fe^{2+} decrease continuously after the initial maxima. SEM micrographs of CO_2-exposed samples indicate dissolution of ankerite, while siderite and quartz are mainly unaffected. The experiments on the siderite separate clearly show that ankerite is dissolved and siderite is stable. We conclude that siderite is a potential CO_2 trapping phase in iron-bearing reservoirs.

* Corresponding author: Sebastian Fischer. Tel.: +49 (0)331 288 28 37.
E-mail address: fischer@gfz-potsdam.de.

1. Introduction

   Static batch experiments have been performed to investigate mineralogical and geochemical effects of CO_2 exposure on whole rock core samples from the Ketzin pilot site. Powdered monomineralic separates were used to conduct complementary laboratory experiments in order to be able (i) to characterize single fluid-mineral interactions in a relatively simple system, (ii) to assign individual reactions to one mineral and (iii) to calculate dissolution rates for individual rock-forming minerals. In addition, potential mineral precipitates should be easier detectable in these monomineralic experiments.

   The first two sets of long term CO_2-exposure experiments were performed on reservoir and cap-rock-like core material from the pilot CO_2 storage site at Ketzin. Reservoir sandstone samples were exposed to pure CO_2 and synthetic reservoir brine at near in-situ P-T conditions (40°C, 5.5 MPa) for a maximum of 40 months (Exp-A). In a second approach, cap-rock-like siltstone samples were exposed to pure CO_2 and synthetic reservoir brine at 40°C and 7.5 MPa for a maximum of six months (Exp-B). Results of Exp-A were presented and discussed in [1] and [2]. To complete the experimental investigations of mineralogical-geochemical interactions likely to occur within a storage system, siderite was chosen to react with pure CO_2 and 2 M NaCl brine in a new hydrothermal rocking autoclave system equipped with flexible Titanium cells. In this paper we focus on the monomineralic experiments using siderite (Exp-C1) and we will only briefly refer to results of Exp-A and Exp-B.

2. Materials and Methods

2.1 Sample Description

   The monomineralic siderite (iron carbonate) separate used for the experimental series (Exp-C) was received from BRG Hannover and prepared according to procedures described in [3]. Siderite was crushed and sieved to arrive at a grain size fraction of 100 to 200 μm. Based on [3], XRD data with Rietveld refinement prove that the siderite separate is composed of 80 wt% siderite, 17 wt% ankerite and 3 wt% quartz. As determined by EDS multipoint data, the formula of siderite is $Fe_{0.8}Mg_{0.1}Mn_{0.1}CO_3$, that of ankerite is $Ca(Mg_{0.2}Mn_{0.1}Fe_{0.8})(CO_3)_2$; in siderite, Mn^{2+} contents correlate with those of Fe^{2+} [3].

2.2 Experimental Approach

   The experiments using monomineralic separates were performed on a new hydrothermal rocking autoclave system equipped with flexible Titanium Grade-2 cells (Fig. 1). Confining pressure was generated and controlled with an air driven fluid pump (Confining Pressure Controller). During heat up, sampling and/or cooling the pressure was held constant using a backpressure regulator.

   Approximately 5.5 g of the powdered mineral separate were filled into the flexible Ti-cell, which had a volume of about 150 ccm. The Ti-cell was then completely filled with 2 M NaCl and attached to the autoclave vessel, which was then loaded into the oven. The 2 M NaCl brine was prepared using Sigma-Aldrich NaCl salt powder with a purity of ≥99.5%. After all pressure connections were tested for tightness, the system was set to 8.0 MPa. The Ti-cell valve was then cautiously opened to take out a pre-calculated brine volume. Next, an industrial CO_2 flask (at a pressure of approximately 6.0 MPa) was connected with the Ti-cell valve and CO_2 was added to the Ti-cell by lowering the autoclave pressure slowly below that of the CO_2 flask (below 6.0 MPa) using the backpressure regulator. A measuring cylinder was put under the overflow pipe of the autoclave to control the added CO_2 volume, which was sufficient to guarantee for excess CO_2 during the course of the experiment. It was assumed that the volume of displaced water from the autoclave equals the loaded CO_2 volume. Next, the Ti-cell valve was

tightly closed. Afterwards, the system was pressurized to 20 MPa/30 MPa and heated to 80 °C thereafter. For heating, the backpressure regulator was set to experimental pressure. Displaced water was collected in an external reservoir and the autoclave as well as the loaded Ti-cell were isobaric at all times. For each individual experiment, the brine to mineral weight-ratio was 20 to one. During sampling, the oven unit was turned upside down to assure sampling of brine instead of CO_2 fluid from the headspace. Sampling was performed by setting the air pump slightly above 20 MPa/30 MPa so that, once brine fluid left the Ti-cell, water could flow into the autoclave to keep the system isobaric. In order to determine time dependent dissolution behavior, successive fluid samples were taken after several different time steps. A total of 2.5 to 3.0 ml fluid were sampled for each sampling run; 1.0 ml out of the uptake, which was poured away, 1.0 ml for cation, and between 0.5 to 1.0 ml for anion analysis. Accordingly, the total amount of solution sampled (three to seven samples of 2.5 to 3.0 ml each in Exp-C1) did not exceed 12% of the initial solution volume. Sampling vials for cation analysis were acidified with 10 µl of 65% pure HNO_3. The pH was estimated using pH indicator paper, which was held directly at the Ti-cell valve outlet. Solid samples were washed out of the Ti-cell and filtered after quenching at the end of the run. Individual experiments were run for one week.
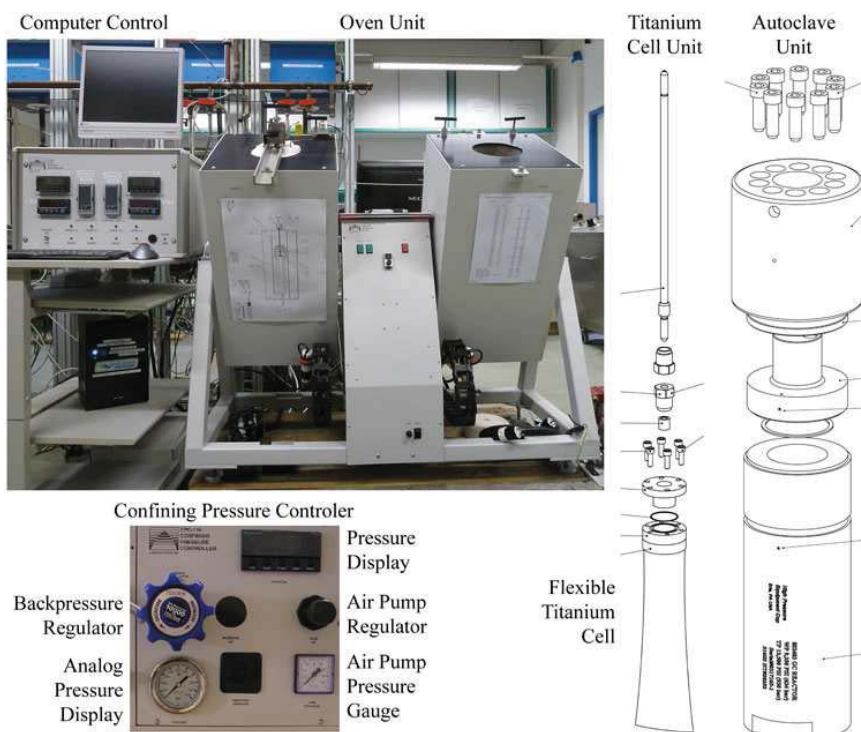

Fig. 1 – The hydrothermal rocking autoclave system used for the monomineralic experiments (Exp-C).

3. Analytical Techniques

3.1 Fluid Analysis

A DIONEX DX-120 ion chromatograph was used to determine Cl^- and SO_4^{2-} concentrations in the experimental brine. Deionized water was used for dilution to 1/100. Other anions were below detection limit. Cations were analyzed with a Varian VISTA-MPX ICP-AES device operating with axial plasma. Samples were diluted with deionized water to 1/100 for Mn^{2+}, Ba^{2+} and Sr^{2+}, 1/1,000 for Ca^{2+}, Mg^{2+} and Fe^{2+}, and 1/10,000 for Na^+. Sampled fluids were not additionally filtered because a filter was used with the Ti-cell adapter plug.

3.2 Analysis of Solid Material

In order to identify possible changes within each mineral and to be able to identify and quantify any new formed mineral phase(s), XRD measurements were performed on homogenized sample aliquots. Homogenization was done with an agate mortar and pestle; each sample aliquot was ground for ten minutes. X-ray diffraction data was collected on a Panalytical Empyrean diffractometer. Rietveld refinements were done with AutoQuan, a BGMN based software.

Selected samples were additionally investigated for changes of mineral surfaces with a Zeiss Ultra 55 plus Scanning Electron Microscope (SEM) equipped with an energy dispersive X-ray (EDS) system. The SEM was operated at 20 kV and 15 nA. Au-coatings were used to allow for carbonate detection and identification.

4. Results of Siderite Experiments

Until today three individual experiments using the siderite separate have been performed and evaluated; these are hereafter referred to as Exp-C1-1, Exp-C1-2 and Exp-C1-3, respectively. Exp-C1-1 was the first experiment conducted on the new rocking autoclave system. Due to problems related to the heating process and handling of the pump, anticipated experimental P-T conditions were reached only after 232 h (Fig. 2). Handling of the heat-up process was much better controlled and quicker for Exp-C1-2 and Exp-C1-3. The latter experiment was performed at 30 MPa. In the sampled brine, all three siderite experiments show generally increased ion concentrations for Ca^{2+}, Mg^{2+}, Mn^{2+} and Fe^{2+} with experimental run duration. Sr^{2+} was below detection limit in all samples. Na^+ was only measured in Exp-C1-1. In all the three siderite experiments, Ca^{2+} and Mg^{2+} as well as Fe^{2+} and Mn^{2+} concentrations, respectively, show similar behavior over time (Fig. 2).

In Exp-C1-1, Ca^{2+} and Mg^{2+} are steadily increasing to reach maximum concentrations of 1.62e-2 and 4.44e-3 mol/L after 576 h at the end of the experiment. Fe^{2+} and Mn^{2+} reach maximum concentrations of 1.22e-2 and 2.37e-4 mol/L after 312 h and continuously decrease from that moment on. Na^+ concentration levels are constant until 312 h and then decline slightly to a minimum of 1.78 mol/L after 456 h. To the end, Na^+ concentrations increase again slightly.

In Exp-C1-2, handling of the autoclave system was improved and the heat-up process was much quicker so that first samples could be taken about three hours after CO_2 addition. More samples were taken during the first hours of the experiment in order to have information of the phase of rapid concentration increase (which was not sampled in Exp-C1-1). Ca^{2+} and Mg^{2+} show a rapid increase and reach first maximum concentrations of 1.23e-2 and 3.67e-3 mol/L after 25 h. Both ions reveal decreasing concentrations to minima of 1.07e-2 and 3.38e-3 mol/L after 73 h. From that moment on, both ions continuously increase again to 1.21e-2 and 3.67e-3 mol/L at the end of the experiment. Fe^{2+} and Mn^{2+} also display similar behavior with the difference that after the maxima were reached during the initial

phase within 18 (Mn^{2+} = 4.27e-4) and 25 h (Fe^{2+} = 1.96e-3), respectively, both ions continuously decrease throughout the rest of the experiment.
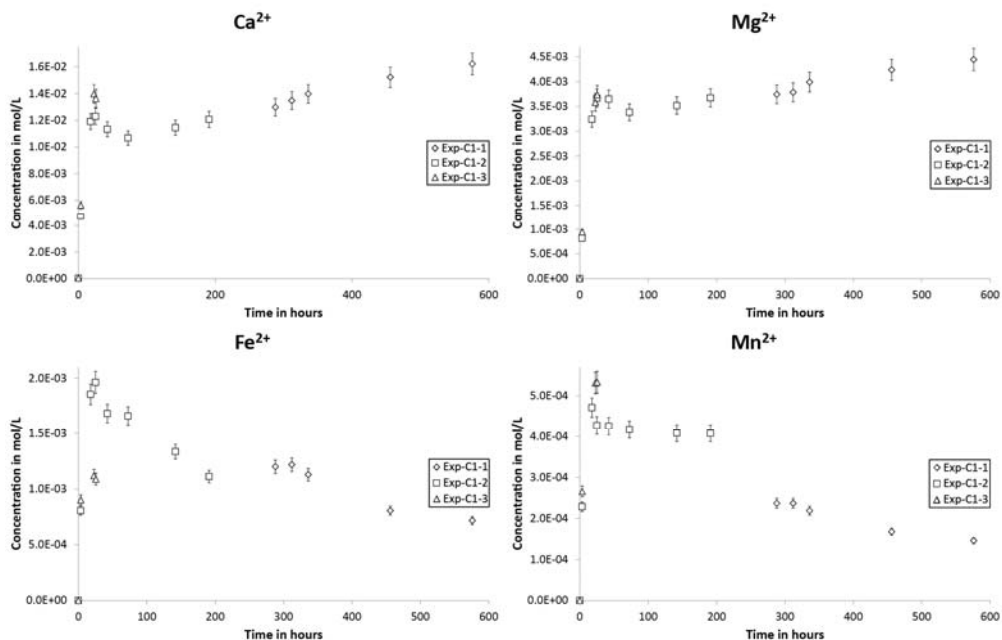

Fig. 2 – Fluid data for major cations from the three siderite experiments (Exp-C1-1, Exp-C1-2 and Exp-C1-3) plotted against experimental run duration. It is apparent that Ca^{2+} and Mg^{2+} as well as Fe^{2+} and Mn^{2+}, respectively, show similar behavior. Error bars plotted refer to 5% rel.

In Exp-C1-3, first samples were already taken four hours after CO_2 addition. In that time span, Ca^{2+}, Mg^{2+}, Mn^{2+} and Fe^{2+} increased rapidly. Ca^{2+} and Fe^{2+} concentrations reached maxima after 23 h (1.4e-2 and 1.1e-3 mol/L, respectively), while Mg^{2+} and Mn^{2+} concentrations continue to increase to the end of the experiment. Exp-C1-3 had to be stopped after approximately 30 h, because no more fluid could be sampled. It is assumed that the filter was blocked.

The comparison of Exp-C1-1, Exp-C1-2 and Exp-C1-3 reveals that the collected data for the siderite separate can be discussed and evaluated as one complete data set. In Figure 3 it is apparent that the quickest and highest initial concentration increases for Ca^{2+}, Mg^{2+} and Mn^{2+} generally occurred in Exp-C1-3, but also that Fe^{2+} concentrations in Exp-C1-3 are not as high as in Exp-C1-2. It is furthermore apparent that the comparatively late sampling but the longer run duration of Exp-C1-1 nicely completes the datasets of Exp-C1-2 and Exp-C1-3, respectively.

Mineral surfaces of grains from the untreated siderite separate as well as of Exp-C1-1 were studied with SEM. Quartz and traces of pyrite, K-feldspar and a K-rich clay mineral, possibly illite, were found next to siderite and ankerite. Untreated siderite shows surface structures that are characterized by relatively sharp edges and steps within the crystal, but also by fines and minor holes/kinks and pits occasionally (Fig. 3A). Surface structures on untreated ankerite (Fig. 3B) are very similar compared to untreated siderite. Nonetheless, siderite and ankerite grains can be clearly identified and differentiated optically and chemically. CO_2-treated ankerite grains show strongly corroded surface structures with

larger and much more frequent dissolution holes and pits (Fig. 3C+D), while some CO_2-treated siderite surfaces are less sharp-edged but reveal no change in quantity and depth of holes and pits (Fig. 4C).

Collected XRD diffractograms of the untreated siderite separate and the three siderite experiments reveal significant differences between the distinct samples; especially for the two carbonate phases. Siderite, ankerite and quartz were verified by XRD measurements. No new formed mineral phase was determined in any of the CO_2-treated samples. In Figure 4 it is apparent that siderite shows increasing modal abundances with time (from initially 69.6±1.3 to 80.7±1.5 wt% at the end), while ankerite shows the opposite trend (from initially 26.7±1.2 to 16.2±1.4 wt% at the end). Changes in quartz abundances are within analytical error (i.e. constant between 2.9±0.9 and 3.8±0.8 wt%). The untreated siderite separate is composed of 69.6±1.3 wt% siderite, 26.7±1.2 wt% ankerite and 3.8±0.8 wt% quartz. These mineral abundances slightly differ from those described in [3].

Experiments on illite and labradorite separates (Exps-C2 and Exps-C3) are still on-going and results will be at hand soon.
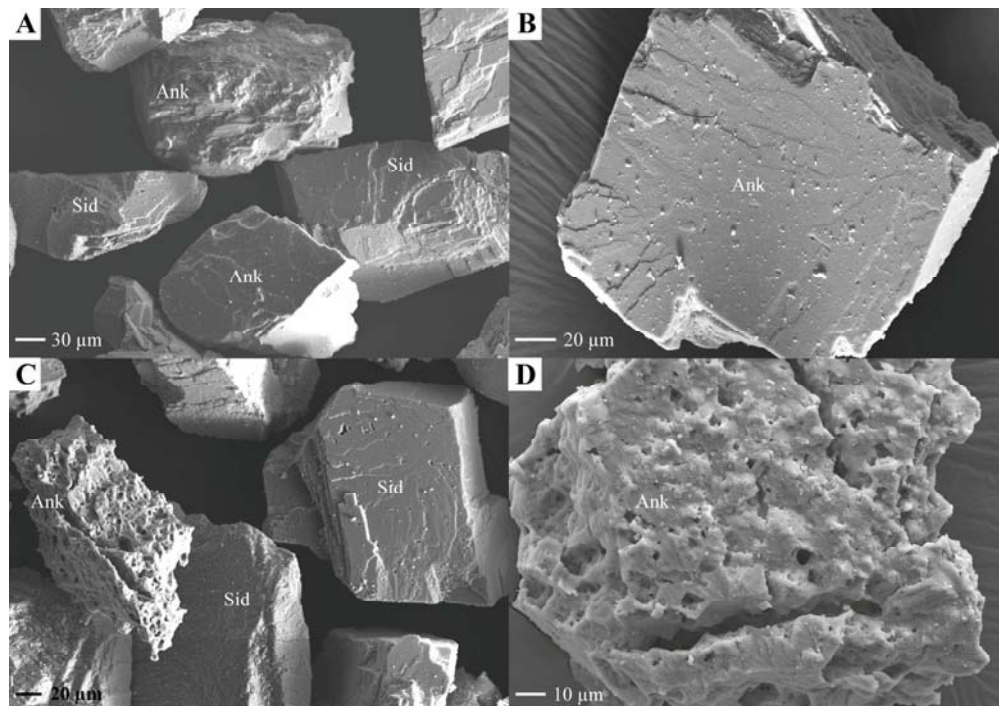

Fig. 3 – SEM micrographs showing surface structures of grains from the siderite separate. A – Typical untreated siderite and ankerite grains. B – Untreated ankerite grain with fines on the surface. C shows CO_2-treated grains of Exp-C1-1 that display some holes and pits on siderite surfaces, and strongly corroded ankerite surfaces. D – A CO_2-treated ankerite grain displaying typical dissolution features.

5. Discussion

The reaction of the siderite separate with CO_2 and 2 M NaCl brine is characterized by generally increased Ca^{2+}, Mg^{2+}, Mn^{2+} and Fe^{2+} concentrations. Optical and chemical grain inspection of the

untreated siderite separate reveals clear differentiation between siderite and ankerite, but also shows the presence of quartz, pyrite, K-feldspar and illite (?). The SEM investigation of grain surface morphologies additionally point towards higher solubility of ankerite over siderite under the applied experimental conditions. This is also supported by Rietveld refined XRD data, which reveal decreasing ankerite and increasing siderite abundances over time.
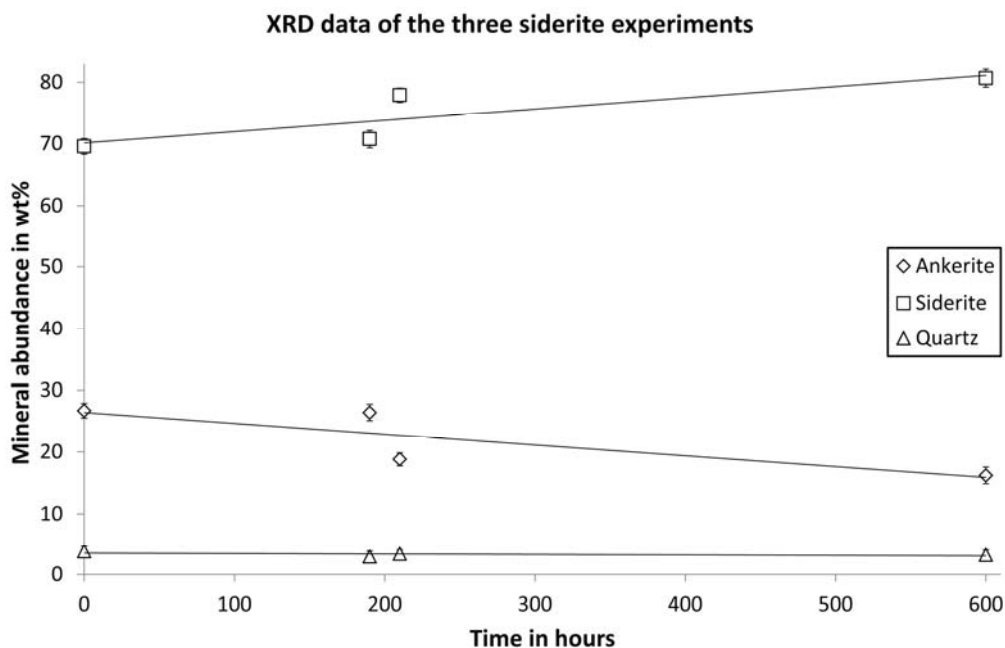
Fig. 4 – Mineral abundances plotted against time of CO_2 treatment. While quartz reveals constant abundances, siderite shows increasing and ankerite decreasing weight percentages over time, respectively. Error bars indicate relative errors for each refinement. 0 h refers to the untreated siderite separate, <200 h to Exp-C1-3, >200 h to Exp-C1-2, and 600 h to Exp-C1-1, respectively.

Despite the fact that Exp-C1-3 was conducted at 30 MPa, and Exp-C1-1 and Exp-C1-2 only at 20 MPa, respectively, we believe that – based on our data (Fig. 2) – all three siderite experiments can be discussed and evaluated as one complete data set. Preliminary calculations performed with the software SUPCRT [4] indicate that the influence of pressure on mineral solubilities – especially for carbonates – is rather negligible (< 1% relative difference) in the range 20-30 MPa, but needs to be considered in the range 0.1-20 MPa. For these differences in pressure thermodynamic databases used for geochemical modeling, e.g., should hence be fitted.

Concentrations of Ca^{2+}, Mg^{2+}, Mn^{2+} and Fe^{2+} in the brine show rapid and steep initial increases followed by slight decreases afterwards (Fig. 1). The initial increases are most likely related to kinetically rapid dissolution of fines (e.g. [5], [6], [7]) present in the untreated siderite separate; possibly due to crushing. Such fines were detectable on grain surfaces of some untreated siderite and ankerite grains (Fig. 2B). Subsequent decreases in ion concentration levels are related to the formation of (a) mineral phase(s) incorporating the respective cations. Note that no newly formed phase(s) were detected. This is most likely related to either subsequent dissolution of the new formed phase(s), or to the fact that the amount of (the) new formed phase(s) was too small to be detected. After reaching a minimum, Ca^{2+} and Mg^{2+} brine

concentrations increase again implying dissolution of Ca^{2+} and Mg^{2+} components to the end of the experiments. In contrast to that, Fe^{2+} and Mn^{2+} concentrations in the samples brine decrease after having reached a maximum. This implies continuous precipitation of (a) mineral(s) incorporating Fe^{2+} and Mn^{2+} ions, respectively. These findings are in line with SEM investigations, which clearly show dissolution of CO_2-exposed ankerite, but minor dissolution features or partially undissolved siderite grains (Fig. 2C).

These latter observations can be explained by kinetically rapid dissolution of $Ca^{2+}(/Mg^{2+})$-rich ankerite, that, after Ca^{2+} (super)saturation is reached in the brine, changed into precipitation of $Fe^{2+}(/Mn^{2+})$-rich siderite. As Mg^{2+} is also present in siderite it is furthermore possible that partial dissolution of Mg^{2+} occurs in siderite leaving other ions largely unaffected within the crystal lattice. Another explanation would be the substitution of Mg^{2+} by Fe^{2+} and Mn^{2+} in siderite and/or ankerite. It is known from literature that in siderite Fe^{2+} is replaced by other metallic ions such as Mg^{2+} and Mn^{2+}, but also that the main substitution in ankerite is that of Fe^{2+} for Mg^{2+}, and subordinately for Mn^{2+} [8]. Similar substitution processes in the siderite separate could explain increasing Mg^{2+} opposed to decreasing Fe^{2+} and Mn^{2+} brine concentrations by Mg^{2+} substitution for Fe^{2+} and Mn^{2+} in ankerite (and/or siderite).
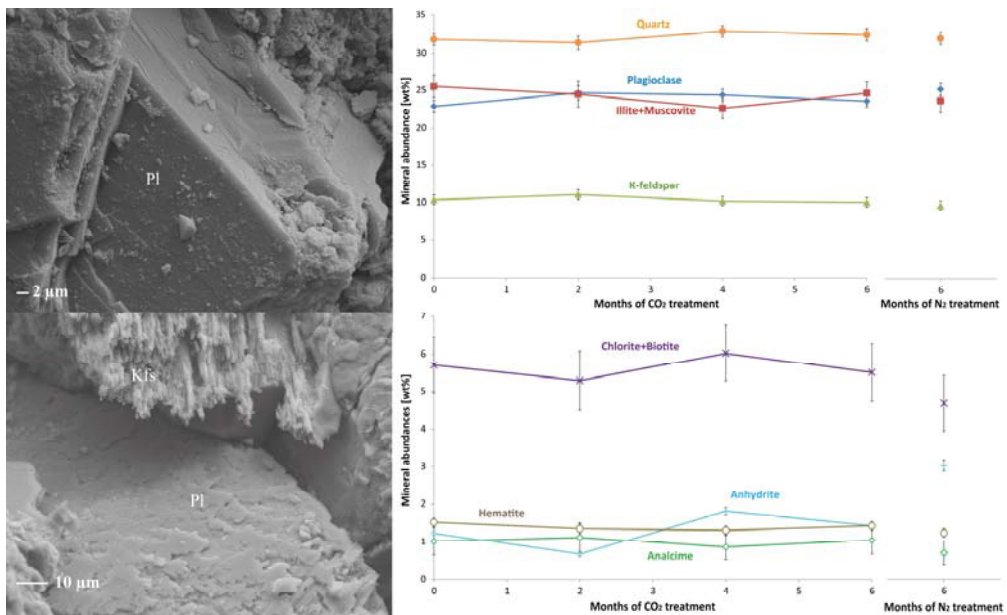

Fig. 5 – Micrographs of untreated (top) and CO_2-treated (bottom) feldspar mineral surfaces of Exp-A showing dissolution of plagioclase (pl) as well as of K-feldspar (Kfs) due to CO_2 exposure. The right side shows two plots of Rietveld refined XRD data of Exp-B for major (top) and minor (bottom) mineral phases of the CO_2- and N_2-treated siltstone, respectively. Changes in mineral abundance are related to the natural variability and not caused by CO_2 exposure.

By performing a reservoir simulation study of geochemical processes occurring within the reservoir of the Ketzin pilot site, [9] found out that siderite is the most stable carbonate mineral trapping phase. Similar observations are described in [10], who performed geochemical modeling using Rotliegend Sandstone and observed dissolution of anhydrite and hematite next to precipitation of iron carbonate at 5 MPa pCO_2. [11] also concluded that in low-temperature (37 °C) Utsira-like reservoirs, the formation of siderite (or hydrous magnesium carbonates) is favored over that of ankerite (and dolomite and magnesite).

The findings of the latter three papers performing numerical experiments are supported by the here presented laboratory experiments, in which ankerite dissolves and siderite is more stable. While e.g. [9] included other carbonates (i.e. calcite, dolomite and magnesite) in their models and conclusions are more robust accordingly, the here used siderite separate only contained ankerite next to siderite as carbonate phases and conclusions regarding carbonate stabilities in general are obsolete. Nonetheless, our results show that siderite is likely to be a stable mineral trapping phase; at least in Fe^{2+}-bearing reservoirs. In contrast to that, [6] and [12] argued that, amongst others, ankerite can replace siderite or precipitate instead of it due to increased Ca^{2+} brine concentrations. Their findings originate from a very specific modeling study. They evaluated geochemical changes in ferric-iron bearing synthetic redbed reservoirs as a consequence of co-injecting CO_2 and sulfur-bearing waste gas. Thermodynamic data for ankerite was not available in the kinetic modeling database. For that reason ankerite was excluded from the mineral assemblages. A comparison of siderite and ankerite stabilities over time is thus missing, and it is concluded that siderite is a major carbonate trapping phase.

Exp-A and Exp-B show only minor changes during long-term CO_2-exposure experiments. In sandstone (Exp-A), major changes are related to feldspar minerals that show (intensified) dissolution with experimental time (Fig. 5). In siltstone, mineral abundances do not reveal significant differences comparing untreated and N_2-treated with CO_2-treated siltstone samples (Fig. 5).

6. Conclusions

The analysis of CO_2-exposure experiments performed on the monomineralic siderite separate show that ankerite is dissolved and siderite is stable. Accordingly, it is likely that siderite is a stable CO_2 trapping phase in Fe-bearing reservoirs.

The experiments on sandstone and siltstone samples from the Ketzin reservoir reveal only minor changes in mineralogy and geochemistry. In sandstone samples, analcime, chlorite, hematite and illite abundances slightly decrease, while quartz abundances tendentially increase with time. Feldspar minerals (plagioclase and K-feldspar) show clear signs of dissolution. In siltstone, changes of mineral abundances are mainly within analytical error. By performing whole rock exposure experiments it is generally difficult to differentiate CO_2-related changes from the natural variability of the samples.

Based on our studies, the chemical integrity of the Ketzin reservoir is not (significantly) affected by the injection of CO_2, and siderite is presumably a stable (long-term) CO_2 trapping phase.

References

[1] Fischer, S., Liebscher, A., Wandrey, M., and the CO_2SINK Group, 2010. CO_2-brine-rock interaction – first results of long-term exposure experiments at in situ P-T conditions of the Ketzin CO_2 reservoir. Chem. Erde 70, 155–164.

[2] Fischer, S., Zemke, K., Liebscher, A., Wandrey, M., and the CO_2SINK Group, 2011. Petrophysical and petrochemical effects of long-term CO_2-exposure experiments on brine-saturated reservoir sandstone. Energy Procedia (4), 4487–4494.

[3] Kaufhold, S., Dohrmann, R., 2012. Mineral standards for the COORAL project (#COO14 Siderite). Internal Technical Report, BGR Hannover.

[4] Johnson, J.W., Oelkers, E.H., Helgeson, H.C., 1992. SUPCRT92: A software package for calculating the standard molal thermodynamic properties of minerals, gases, aqueous species, and reactions from 1 to 5000 bar and 0 to 1000°C. Computers & Geosciences 18 (7), 899–947.

[5] Palandri, J.K., Rosenbauer, R.J., Kharaka, Y.K., 2005. Ferric iron in sediments as a novel CO_2 mineral trap: CO_2-SO_2 reaction with hematite. Appl. Geochem. 20, 2038–2048.

[6] Holdren, G.R., Berner, R.A., 1979. Mechanism of feldspar weathering. 1. Experimental Studies. Geochim. Cosmochim. Acta 43, 1161-1171.

[7] Bateman, K., Turner, G., Pearce, J.M., Noy, D.J., Birchall, D., and Rochelle, C.A., 2005. Large-Scale Column Experiment: Study of CO_2, Porewater, Rock Reactions and Model Test Case. Oil & Gas Science and Technology – Proceedings of the International Conference on Gas-Water-Rock Interactions Induced by Reservoir Exploitation, CO_2 Sequestration and Other Geological Storage, Vol. 60 (1), 161–175.

[8] Deer, W. A., Howie, R. A., Zussman, J., 1992. An Introduction to the Rock-Forming Minerals (2nd Edition), Prentice Hall, London.

[9] Klein, E., De Lucia, M., Kempka, T., Kühn, M. Evaluation of long-term mineral trapping at the Ketzin pilot site for CO_2 storage: An integrative approach using geochemical modelling and reservoir simulation. Submitted to IJGGC.

[10] De Lucia, M., Bauer, S., Beyer, C., Kühn, M., Nowak, T., Pudlo, D., Reitenbach, V., Stadler, S., 2012. Modeling CO_2-induced fluid-rock interactions in the Altensalzwedel gas reservoir. Part I: From experimental data to a reference geochemical model. Environ. Earth Sci. 67 (2), 563–572.

[11] Pham, V.T.H., Lu, P., Aargaard, P., Zhu, C., Hellevang, H., 2011. On the potential of CO_2-water-rock interactions for CO_2 storage using a modified kinetic model. IJGGC 5, 1002–1015.

[12] Palandri, J.L., Kharaka, Y.K., 2005. Ferric-iron bearing sediments as a mineral trap for CO_2 sequestration: Iron reduction using sulfur-bearing waste gas. Chem. Geol. 217 (3–4), 351–364.

7. Publication VI:

"Mineral solubilities in CO$_2$-saturated NaCl brine systems"

Water Rock Interaction [WRI 14]

Mineral solubilities in CO_2-saturated NaCl brine systems

Sebastian Fischer[a,b,*] and Axel Liebscher[a]

[a]Helmholtz Centre Potsdam, GFZ German Research Centre for Geosciences, Telegrafenberg, D-14473 Potsdam, Germany
[b]Berlin Institude of Technology, Chair of Mineralogy-Petrology, Ackerstrasse 76, D-13355 Berlin, Germany

Abstract

Experiments on CO_2-brine-mineral interactions were designed to provide kinetic data for individual rock-forming minerals. Samples of an illite-smectite mixed layer mineral and a labradorite separate were stored in flexible Ti-cells together with 2 M NaCl brine and pure CO_2 at 80 °C and 20 MPa for two and three weeks, respectively. The empirical formulae $K_{0.5-0.7}(Mg_{0.1-0.2}Al_{1.8-1.9})(Al_{0.4-0.6}Si_{3.4-3.6})O_{10}(OH)_2$ and $Na_{0.5-0.6}Ca_{0.4-0.5}Al_{1.3-1.6}Si_{2.4-2.6}O_8$ were calculated for illite and labradorite. X-ray diffraction data with Rietveld refinements reveal a pure labradorite separate. The illite separate is composed of 73.5±1.3 wt% illite, 10.8±1.3 wt% Ca-smectite, 11.9±0.4 wt% orthoclase, and 3.9±0.2 wt% quartz. Based on the acquired geochemical data, the experiments on monomineralic separates indicate (i) preferred dissolution of the Ca-smectite component out of the illite-smectite mixed layer mineral, and (ii) dissolution of labradorite.

1. Introduction

Geological storage of CO_2 in the subsurface is a key option for reducing anthropogenic gas emissions to the atmosphere and thus to mitigate global warming (e.g. [1]). The presence of CO_2 in a (siliciclastic) storage system will cause complex geochemical reactions between injected CO_2, formation brine and reservoir rock (e.g. [2]). Dissolution of primary minerals (i.e. alumosilicates) and/or precipitation of secondary minerals (i.e. carbonates) are likely to occur (e.g. [3]). To better understand and characterize single fluid-mineral reactions, and to be able to calculate dissolution rates for individual minerals, relatively simple experiments were designed in the scope of GaMin'11 project. The GaMin'11 project is a round robin inter-laboratory comparison of geochemical experiments in gas-fluid-mineral systems and was initiated by BGR Hannover and USGS, Menlo Park, CA. Project members followed identical starting

* Corresponding author: Sebastian Fischer; Tel.: +49 331 288 28 37
E-mail address: fischer@gfz-potsdam.de.

conditions using identical mineral separates and brine compositions. The aim was (i) to provide an estimate of potential variance in kinetic data derived from the respective experiments and (ii) to validate kinetic data for the observed mineral dissolution reactions at P-T conditions relevant for CO_2 storage scenarios. Siderite, illite and labradorite separates were chosen. Siderite is an important mineral in carbonate-bearing, iron-rich reservoirs (e.g. [4]); illite and labradorite are typical in siliciclastic storage environments. In this paper we present results of experiments on illite and labradorite performed at GFZ Potsdam in the context of GaMin'11; siderite experiments are described in Fischer et al. (submitted).

2. Materials & Methods

2.1. Sample Description

Mineral separates of an illite-smectite mixed-layer mineral (Ill-0) and a labradorite (Lab-0) were provided by BGR Hannover; for details see [5] and [6]. Grain sizes are <250 μm for illite, and 100-200 μm for labradorite. Based on EDS measurements, the empirical formula for illite was calculated to be $K_{0.5-0.7}(Mg_{0.1-0.2}Al_{1.8-1.9})(Al_{0.4-0.6}Si_{3.4-3.6})O_{10}(OH)_2$, that of labradorite is $Na_{0.5-0.6}Ca_{0.4-0.5}Al_{1.3-1.6}Si_{2.4-2.6}O_8$. X-ray diffraction calculations reveal disordered illite, Ca-smectite, orthoclase and quartz. The presence of Ca-smectite is consistent with XRF data [6]. Rietveld refinements yield the following composition of the illite separate: 73.5±1.3 wt% illite, 10.8±1.3 wt% Ca-smectite, 11.9±0.4 wt% orthoclase, and 3.9±0.2 wt% quartz. An andesine with An_{50} was the plagioclase revealing the best fit for the labradorite separate.

2.2. Experimental Approach

The separates of illite and labradorite were exposed to pure CO_2 and 2 M NaCl brine at 80 °C and 20 MPa. Experiments were performed on a rocking autoclave system equipped with flexible Titanium Grade-2 cells allowing for isobaric sampling. About 5.5 g of powdered separate were filled into the Ti-cell that has a volume of about 150 cm^3. The Ti-cell was filled with 2 M NaCl brine, which was prepared from ≥99.5% pure Sigma-Aldrich NaCl salt powder, and pure CO_2. Afterwards, the system was pressurized to 20 MPa and heated to 80 °C thereafter. The brine to mineral weight-ratio was 20 to one. Experimental run durations were two (illite) and three weeks (labradorite), respectively. The experiments were repeated under identical conditions in order to collect two data sets for each separate (i.e. Ill-1, Ill-2; Lab-1, Lab-2), and also to test for reproducibility. To determine time dependent dissolution behavior, successive fluid samples were taken after several different time steps. A total of 2.5 to 3.0 ml fluid was taken during each sampling run; 1.0 ml from the uptake that were poured away, 1.0 ml for cation, and between 0.5 to 1.0 ml for anion analysis. Sampling vials for cation analysis were acidified with 10 μl of 65% pure HNO_3. Solids were washed out of the Ti-cell and filtered after quenching at the end of the run.

3. Results

3.1. Illite Experiments

The reaction of illite with 2 M NaCl brine and CO_2 is characterized by generally increased cation concentrations in the sampled brine. Ca^{2+} and Mg^{2+} show very similar behavior (Fig. 1A). After a sharp and rapid increase to maximum values of $2.6 \cdot 10^{-3}$ and $8.8 \cdot 10^{-4}$ mol/L after 49 h, respectively, both cations slightly decrease and show constant concentration levels (within error) from 72 h to final concentrations of $2.5 \cdot 10^{-3}$ and $8.4 \cdot 10^{-4}$ mol/L after 349 h, respectively. Note that K^+ could not be determined in ICP-AES measurements (axial plasma) due to Na^+ peak overlapping. Larger particles are generally composed of very small plates and irregular structures. Smaller crystals and coatings of halite rarely occur in Ill-1.
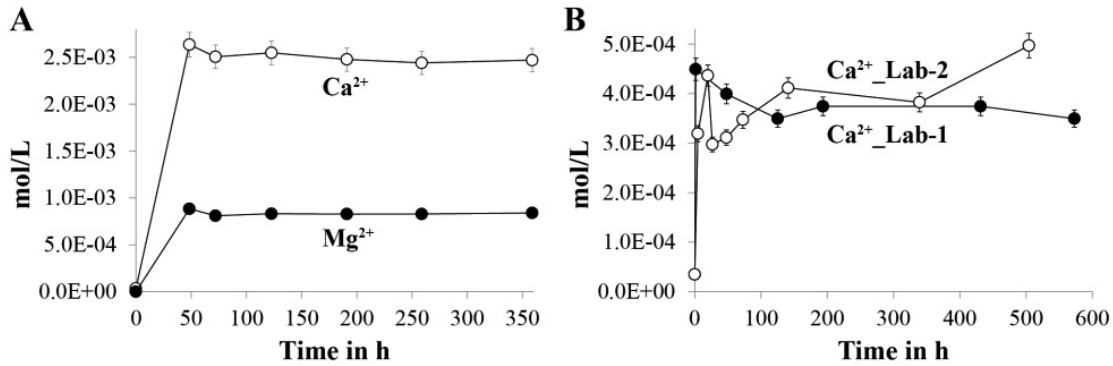
Fig. 1. (A) ICP-AES fluid data of Ill-1; (B) Comparison of fluid data from Lab-1 and Lab-2. 5% error bars are plotted.

About 3.5 wt% of halite is present after the experiment. Normalized mineral abundances on a halite-free basis are 79.0±1.5 wt% illite, 9.3±1.4 wt% Ca-smectite, 9.2±0.5 wt% orthoclase, and 2.5±0.2 wt% quartz. Apart from halite (which precipitated during sample drying after the experiments), no other newly formed mineral phase was detected. Some illite and Ca-smectite peaks show changes in peak shape and intensity. Scanning electron microscopy (SEM) investigations of grain surfaces prior to (Ill-0) and after the experiments (Ill-1 and Ill-2) did not reveal significant changes for phases of the illite separate (Fig. 2A and 2B).

Rietveld refined XRD data indicate dissolution of Ca-smectite, orthoclase and quartz, and a presumably relative enrichment of illite. The coherent increase and behavior of Ca^{2+} and Mg^{2+} in the experimental brine point to preferred dissolution of Ca-smectite in the illite-smectite mixed layer silicate.

3.2. Labradorite Experiments

The XRD analysis revealed the presence of labradorite as the only mineral phase present. Neither in untreated (Lab-0), nor in CO_2-treated labradorite samples other minerals were detected. The comparison of both diffractograms (Lab-0 and Lab-1) shows only very minor differences in peak size; peak shape and position are congruent. The reaction of labradorite with 2 M NaCl brine and CO_2 yields generally increased cation concentrations in the sampled brine. The evolution of fluid data with time shows slight differences between Lab-1 and Lab-2. In both experiments it is apparent that in Ca^{2+} displays very rapid concentration increases within the first hours (Fig. 1B). In Lab-1, Ca^{2+} reached maximum concentrations of $4.5 \cdot 10^{-4}$ mol/L after two h. This maximum is followed by decreasing concentrations to $3.5 \cdot 10^{-4}$ mol/L Ca^{2+} after 125 h. From then on Ca^{2+} levels are constant (within error) till the end of the experiments after 573 h. In Lab-2, Ca^{2+} concentrations show a less steep increase and reach a first maximum of $4.4 \cdot 10^{-4}$ mol/L after 20 h, which is followed by a steep decrease to $3.0 \cdot 10^{-4}$ mol/L after 27 h. From that point on, Ca^{2+} concentrations tendentially increase again to $5.0 \cdot 10^{-4}$ mol/L at the end of the experiment after 504 h. Optical inspection of grain surfaces on SEM micrographs reveals slight changes during the experiments. While clean surfaces and steps are typical for untreated labradorite (Fig. 2C) CO_2-treated labradorite grains display corrosion textures on edges, and dissolution holes on plane surfaces (Fig. 2D).

While XRD data neither show changes in labradorite composition nor newly formed phases, the significantly increased Ca^{2+} concentrations and the presence of corrosion textures on CO_2-treated labradorite grains clearly point toward labradorite dissolution in the course of the experiments. Experimental fluid data reveals slightly different Ca^{2+} behavior between Lab-1 and Lab-2. While Ca^{2+}

evolves to steady concentration levels after approximately 100 h in Lab-1, the tendential increase of Ca^{2+} in Lab-2 from 27 h on is either signifying continuous dissolution, or the trend could be blurred by the last sample after 504 h that yielded the highest Ca^{2+} concentrations of all measured labradorite samples and could thus be an outlier.
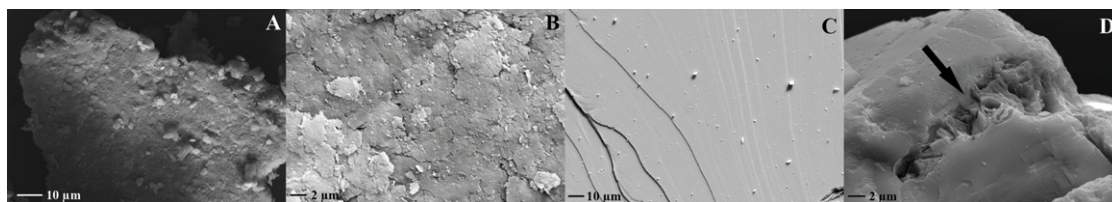

Fig. 2. (A) Typical appearance of illite in untreated sample; (B) Detailed surface structure of a CO_2-treated illite; (C) Smooth surface of a typical untreated labradorite; (D) Corrosion texture (arrow) on a CO_2-treated labradorite.

4. Conclusions

The experiments on monomineralic separates are generally characterized by increasing cation concentrations in the sampled brine, which are caused by CO_2-brine-mineral interactions. Rapid and steep initial increases in ion concentrations are related to fast dissolution kinetics of fines (i.e. micro-scale particles originating from crushing of source material). Results of experiments on the illite separate point toward dissolution of Ca-smectite out of the illite-smectite mixed layer mineral. Data from labradorite experiments show slight corrosion of labradorite. It is noteworthy that in none of the so far performed experiments on mineral separates a newly formed (carbonate) mineral was detected.

Acknowledgements

References

[1] Holloway S. An overview of the underground disposal of carbon dioxide. *Energy Conver. Manag* 1997; **38**: 193– 198.

[2] Rochelle CA, Czernichowski-Lauriol I, Milodowski AE.. The impact of chemical reactions on CO_2 storage in geological formations: a brief review. In: Baines, S.J., Worden, R.H. (Eds.), *Geological Storage of Carbon Dioxide.* Geological Society, London, Special Publications 233; 2004, p 87–106.

[3] Gunter WD, Wiwchar B, Perkins EH.Aquifer disposal of CO_2-rich greenhouse gases: extension of the time scale of experiment for CO_2-sequestration reactions by geochemical modeling. *Mineral. Petrol* 1997; **59**: 121–140.

[4] Testemale D, Dufaud F, Martinez I, Bénézeth P, Hazemann J-L, Schott J, Guyot F. An X-ray absorption study of the dissolution of siderite at 300 bar between 50 °C and 100 °C. *Chem. Geol* 2009; **259**: 8–16.

[5] Kaufhold S, Dohrmann R. *Mineral standards for the COORAL project (#COO7 Illite)*. Internal Technical Report, BGR Hannover; 2012

[6] Kaufhold, S. and Dohrmann, R., 2012B. Mineral standards for the COORAL project (#COO2 Plagioclase). Internal Technical Report, BGR Hannover.

8. SYNOPSIS

Laboratory experiments on sandstone, siltstone and mineral separates of siderite, illite and labradorite have been performed in order to determine and evaluate CO_2-brine-mineral reactions potentially relevant for geologic storage of CO_2 in siliciclastic reservoir systems. Whole rock sandstone and siltstone samples from the reservoir formation (Stuttgart Formation) at the Ketzin pilot CO_2 storage site were experimentally studied to analyze the complexity of site-specific reaction paths that are likely to occur within the Ketzin storage system. Experiments on sandstone samples have been additionally modeled using PHREEQC software in order to compare experimental observations with theoretical simulations. Powdered separates of rock-forming minerals were investigated in relatively simple batch systems to experimentally obtain and quantify single CO_2-brine-mineral reactions and to be able to generate kinetic data for siderite, illite and labradorite.

The synopsis is structured as follows: After summarizing the results obtained from the distinct experiments and modeling, the major findings are discussed also with respect to the geochemical fate of each of the considered minerals. The concluding remarks give a broader context of geochemical reactivity during CO_2 storage and categorize the obtained results from this dissertation regarding their relevance for a better understanding of CO_2-brine-mineral reactions. Finally, the way forward based on the knowledge gained during the dissertation is presented in the section *Outlook*.

8.1 Main results

8.1.1 *Sandstone experiments*

Baseline characterization of the studied core sections B2-2, B2-3, B3-1, B3-3 and B4-2 showed that untreated sandstone samples are composed of quartz (27.3 to 38.7 wt%), plagioclase (24.0 to 30.2 wt%), illite + muscovite (13.9 to 21.9 wt%), typically perthitic K-feldspar (5.6 to 9.5 wt%), chlorite + biotite (2.3 to 4.6 wt%) and hematite (0.8 to 4.5 wt%). The samples are weakly cemented by isolated poikilitic patches of analcime, anhydrite and dolomite. The uppermost core sections B2-1 and B2-2 show strongest cementation, which successively decreases with depth. The uneven distribution of pore-filling cement phases results in highly variable mineral abundances of analcime (1.3 to 11.6 wt%), anhydrite (0 to 2.1 wt%) and dolomite (0 to 2.7 wt%). The untreated core section B2-1, whose CO_2-treated subsets show strongest cementation next to lowest porosities, was unfortunately lost during preparation. Sandstone samples are laminated at the mm- to cm-scale; compared to brighter laminae, darker zones are characterized by higher abundance of mineral coatings of Fe-Ti-(hydr)oxides like hematite. Porosities as determined by NMR measurements generally increase from top (B2-1) to base (B4-2). While untreated core sections B2-3, B3-1, B3-3 and B4-2 have porosities between 20.5 and 22.0%, the porosity of untreated core section B2-2 is substantially lower with only 16.9%.

Identification and quantification of CO_2-brine-rock reactions during the sandstone experiments as studied by sampling campaigns after 15, 21, 24 and 40 months are notably hampered by the initial mm- to cm-scale heterogeneity in mineral abundances. Mineralogical-geochemical changes are generally minor and mainly associated with dissolution processes. Also no secondary mineral precipitates were detected during 40 months of CO_2 exposure. The quantification of the observed mineralogical changes is hardly possible and would also be inappropriate, because untreated cm-sized baseline samples are not representative for respective 1-m-long core section intervals due to the high mineralogical variability in both lateral and vertical direction. Although CO_2-treated samples had been taken in close proximity to the baseline samples as well as to each other the samples represent similar, but still not identical starting compositions. Sample compositions vary between different samples and definite trends for individual minerals over time are often missing. Despite the apparent variability, however, analcime, chlorite + biotite as well as hematite indicate overall decreasing mineral abundances with run duration. Also, after 15 months of CO_2 exposure porosities have increased. While CO_2-treated core sections B2-3, B3-1, B3-3 and B4-2 show porosities between 24.4 and 31.3%, the porosity of core section B2-2 increased to 17.5%. Hence, the average porosity of these five core sections increased from 20.3 to 25.8%. The CO_2-treated core section B2-1 has a porosity of 7.3%.

Contrary to the equivocal results from the XRD measurements, mineral surfaces of anhydrite, plagioclase and K-feldspar grains signify changes during 40 months of CO_2-treatment and provide clear evidences of dissolution processes. While anhydrite grains in untreated samples as well as in samples taken after 15 months appear clean and unaltered, first signs of anhydrite alteration were detected in samples taken after 21 months. Initially, corrosion textures are restricted to crystallographic features, but with time and intensified anhydrite alteration these textures occur independent of crystallographic features. Whereas clean and smooth surfaces were detected on

some few untreated plagioclase grains, such surfaces are completely missing in CO_2-treated samples, in which plagioclase is generally characterized by alteration textures that intensify with run duration. Similar corrosion textures were also detected on CO_2-treated K-feldspar grains. Also untreated sandstone samples reveal diagenetic alteration of K-feldspar; however, quality and quantity of respective alteration features suggest intensified K-feldspar dissolution with time of CO_2 exposure.

In samples treated for 15 months, plagioclase compositions as determined by EMPA data indicate a trend from intermediate towards sodium-rich compositions. Pure albite end-member compositions $Ab_{>99}$ were only detected in CO_2-treated samples that also have slightly lower maximum calcium contents compared to the baseline. Hence, EMPA data may suggest albitization.

In the course of the sandstone experiments, concentration of total dissolved solids (TDS) increased from 188 g/L of the initial synthetic brine to 205 g/L after 24 months. (Note that brine data is not available from samples taken after 40 months.) Despite the fact that trends for individual ions are not strictly uniform with time, and K^+ and SO_4^{2-} ion concentrations, e.g., decreased between months 21 and 24, all measured brine ion concentrations increased compared to those of the initial synthetic brine. Largest increases occur during the first 15 months. After 24 months, K^+, Ca^{2+}, Mg^{2+}, Fe^{2+} and Mn^{2+} concentrations exceed the natural Ketzin reservoir fluid levels. While SO_4^{2-} was highly undersaturated in the initial synthetic brine it strongly increases to levels similar to that of the reservoir formation. With respect to aqueous Fe^{2+} concentrations samples show two clusters; one with low Fe^{2+} concentration levels close to those of pristine reservoir brine, and one cluster with Fe^{2+} levels orders of magnitude higher. Sodium and Cl^- brine concentrations increased by approximately 6% during the experiments to levels that are 1/7th below those of the original reservoir formation. Silicon was below detection limit in all but two samples. Compared with the initial synthetic brine, Al^{3+} shows a coherent increase in samples treated for 15 months, but an inconsistent trend for the period between 15 and 21 months. Note that Al^{3+} concentrations were below detection limit in all samples treated for 24 months.

8.1.2 *Siltstone experiment*

Although only one single siltstone core section was used and also a N_2-blank test was conducted in consequence of the problems related to quantifying CO_2-related mineralogical changes during the sandstone experiments, the observations from the siltstone experiment show that the impact of CO_2 on cap-rock-like samples from the Stuttgart Formation at Ketzin was minor, and the identification of fluid-mineral reactions was generally still difficult.

The siltstone samples reveal similar petrographic characteristics compared to the sandstone samples. Main differences are smaller average grain sizes, lack of dolomite and $(Ba,Sr)SO_4$ solid solution as additional cement phase. The untreated siltstone consists of 30.6±4.3 wt% quartz, 25.0±2.7 wt% plagioclase, 23.7±3.6 wt% illite + muscovite, 10.4±1.2 wt% K-feldspar (typically perthitic), 5.6±2.1 wt% chlorite + biotite and 1.3±0.5 wt% hematite. Analcime, anhydrite and $(Ba,Sr)SO_4$ solid solution occur as isolated, poikilitic cement phases. While the quantifiable occurrence of anhydrite is restricted to the uppermost parts of the siltstone section in which it has abundances of 5.5±3.5 wt%, analcime and $(Ba,Sr)SO_4$ solid solution are present in all samples and in abundances of around 1.0 wt% each. After six months run duration and also compared to the N_2 blank none of the minerals

show a clear trend with time. Smaller changes in mineral abundances are related to the natural variability of the siltstone sample.

Corrosion textures on plagioclase and K-feldspar grains intensify, and clean and unaltered feldspar grain surfaces recede with run duration. Whereas anhydrite surfaces in untreated siltstone are clean and smooth, CO_2- as well as N_2-treated samples suggest anhydrite alteration. Surfaces of the remainder minerals of the siltstone sample are unaffected. Based on EMPA data, mineral compositions of feldspars, mica and cement phases are very similar in untreated, CO_2- as well as in N_2-treated siltstone samples.

Fluid data of the siltstone experiment show increased brine ion concentrations. Largest relative increases show K^+ (+109%), SO_4^{2-} (+279%) and Sr^{2+} (+1129%). After six months run duration, the Mg^{2+} concentration of the CO_2-treated sample is significantly higher (+24%) compared to the N_2 blank. While largest changes in brine ion concentrations generally occur within the first two months and most ions remain constant (within analytical error) thereafter, Ca^{2+} and SO_4^{2-} reach maximum concentrations after four and six months, respectively. In both the CO_2- and N_2-treated brine, the remainder ions have equal concentrations within analytical error.

8.1.3 *Geochemical modeling*

In case equilibrium would be attained between the synthetic brine and the averaged mineral assemblage of the Stuttgart Formation sandstone without the addition of CO_2, the albite component of plagioclase, hematite, illite and anhydrite would precipitate, and analcime, chamosite (iron-rich chlorite), the anorthite component of plagioclase, quartz, K-feldspar and dolomite would dissolve. While analcime and chamosite would completely dissolve and would still be undersaturated at the end of the simulation, also about 2/3rd of the initially present anorthite component of plagioclase would dissolve. This CO_2-independent equilibrium model indicates that chemical reactions are partially triggered by the synthetic brine that was used during the experiments. As the first approach of equilibrium modeling including CO_2 turned out to be rather too simplified by considering only the iteratively determined "best match" with experimental observations, a more comprehensive approach yielded better matching models that were ranked based on a predefined statistical-mathematical dispersion relation. While measured brine ion concentrations can in general be acceptably well matched in these equilibrium models when CO_2 is added to the system, K^+, Fe^{2+}, Al^{3+}, Si^{4+} and SO_4^{2-} are rather difficult to match simultaneously. The model yielding the best match with measured brine data comprises a mineral assemblage of the albite component of plagioclase, anhydrite, dolomite, hematite and illite as primary phases.

Kinetic simulations indicate that the model suppressing any mineral precipitation yields best matches with experimental observations, but also that simplified models do not completely cover the complex geochemical system of the sandstone experiments, nor all possible contingencies. In subsequent simulations, the approach of using the best matching simulations of more structured and complex equilibrium models as basis for kinetic models generally showed good matches with measured brine data. However, respective simulations also reveal distinct mismatches for dissolved K^+ and Fe^{2+}, and hence, that reactions involving K- and Fe-bearing minerals are not completely reproduced. Note that the models generally show larger mismatches for dissolved Al^{3+} as well as Si^{4+}, a circumstance most likely related to the sampling strategy and potentially spontaneous precipitation of phases

incorporating Al^{3+} and Si^{4+} (see below). In general, the kinetic models show that the anorthite component of plagioclase and cement phases (analcime, anhydrite and dolomite) dissolve, while clay minerals (chlorite, illite and kaolinite) should form during the sandstone experiments.

8.1.4 *Siderite experiments*

Three individual siderite experiments have been performed; two at 80 °C/20 MPa and one at 80 °C/30 MPa. The experimentally obtained data set shows that the influence of pressure on carbonate mineral solubility is negligible in the range 20 to 30 MPa. The siderite separate is composed of 69.6±1.3 wt% siderite, 26.7±1.2 wt% ankerite and 2.9±0.9 wt% quartz. While siderite increased to 80.7±1.5 wt% and ankerite decreased to 16.2±1.4 wt%, quartz abundances were constant within analytical error. Also based on optical and chemical data obtained during SEM analysis siderite and ankerite can be clearly differentiated. Respective SEM-BSE point count measurements reveal that untreated as well as CO_2-treated siderite both have the average empirical formula $Fe_{0.8}Mg_{0.1}Mn_{0.1}CO_3$, on the one hand, and that the average empirical formula of untreated ankerite slightly changed from $(Ca_{1.0}Mg_{0.2}Mn_{0.1}Fe_{0.7})(CO_3)_2$ to $(Ca_{0.9}Mg_{0.3}Mn_{0.1}Fe_{0.7})(CO_3)_2$ during CO_2 exposure, on the other. During the siderite experiments, Ca^{2+} and Mg^{2+}, as well as Fe^{2+} and Mn^{2+} indicate similar chemical behavior. After rapidly reaching maximum levels after 25 h, Fe^{2+} and Mn^{2+} concentrations continuously decrease afterwards, whereas Ca^{2+} and Mg^{2+} concentrations decline slightly and then start to increase again to reach highest levels at the end of the experiments. Mineral surfaces of CO_2-treated samples occasionally suggest slightly corroded siderite, and strongly corroded ankerite grains. Hence, ankerite has a higher solubility and siderite is more stable. No secondary mineral precipitates were detected during the siderite experiments.

8.1.5 *Illite experiments*

Rietveld refined XRD data showed that the illite separate is initially composed of 73.5±1.3 wt% illite, 10.8±1.3 wt% Ca-smectite, 11.9±0.4 wt% orthoclase and 3.9±0.2 wt% quartz. Based on EDS measurements obtained during SEM analysis the empirical formula of the untreated illite is $K_{0.5-0.7}(Al_{1.8-1.9}Mg_{0.1-0.2})[Si_{3.4-3.6}Al_{0.4-0.6}O_{10}(OH)_2]$. After two weeks of CO_2 exposure the illite separate has a normalized, halite-free composition of 79.0±1.5 wt% illite, 9.3±1.4 wt% Ca-smectite, 9.2±0.5 wt% orthoclase, and 2.5±0.2 wt% quartz. Apart from some halite that precipitated during sample drying after the run, no secondary mineral precipitates were detected. In XRD analysis, some illite and Ca-smectite peaks show changes in peak shape and intensity. No substantial changes in surface morphologies for any mineral of the illite separate were detected after CO_2 exposure. While Na^+ concentrations are constant within analytical error throughout the experiment, Ca^{2+} and Mg^{2+} show a coherent increase and similar chemical behavior. Note that Mg^{2+} concentrations are three times lower than respective Ca^{2+} concentrations during the runs. After rapid increases to maximum concentrations within 49 h after CO_2 addition, both cations decrease slightly and stay constant within analytical error from then on to the end.

8.1.6 *Labradorite experiments*

The labradorite separate is composed of pure labradorite that has an initial composition of $Na_{0.5-0.6}Ca_{0.4-0.5}Al_{1.3-1.6}Si_{2.4-2.6}O_8$ based on SEM-EDS measurements. The labradorite experiment was repeated under identical starting conditions. The comparison of XRD diffractograms obtained from untreated and CO_2-treated labradorite aliquots shows only very minor differences in peak size, and congruence of peak shape and position. While Ca^{2+} brine ion concentrations generally increase and reveal slight differences in brine evolution of the repeat runs, Na^+ concentrations are constant within analytical error in both experiments. In the first labradorite experiment, Ca^{2+} rapidly reached its maximum concentration after two h which is followed by a 22% decrease and constant levels within analytical error to the end afterwards. In the repeat experiment, Ca^{2+} concentrations increase to a relative maximum after 20 h which is followed by a substantial and rapid 32% drop within the next 7 h. From then on Ca^{2+} levels (tendentially) increase to the maximum at the end of the experiment. Compared with the untreated starting material, CO_2-treated labradorite indicates slight alteration textures on grain surfaces, identical mineral composition and no secondary precipitate.

8.2 Discussion

The full data set obtained from the here presented laboratory experiments and geochemical modeling shows that the reaction of CO_2 with rocks of the Stuttgart Formation at Ketzin as well as with separates of rock-forming minerals only cause minor mineralogical-geochemical changes under the applied P-T conditions and brine salinities, namely mineral dissolution and increased brine TDS concentrations. No secondary mineral precipitates were detected during respective CO_2-exposure experiments in the time scale of up to 40 months. While analcime, anhydrite, ankerite, the anorthite component of plagioclase, hematite and K-feldspar dissolve, and the albite component of plagioclase is stable, the fate of carbonate minerals as well as of mica and clay minerals is not consistent. Despite the fact that dolomite appears completely unaffected and stable, and siderite is largely unaffected, the siderite experiments also show dissolution of ankerite. No new formed carbonate phase was detected in any of the here presented laboratory experiments, and only one single kinetic simulation predicts the formation of minute amounts of dolomite. While the Ca-smectite component dissolves during the illite experiments, and illite + muscovite is stable or tendentially forming as predicted during geochemical modeling, chlorite + biotite is (tendentially) dissolving.

The **sandstone** experiments show that only minor mineralogical-geochemical changes occur during respective CO_2-exposure experiments, on the one hand, but also a high natural variability of the samples, on the other. Hence, the identification of clear trends in mineral abundances with time, the quantification of mineralogical changes, i.e. dissolution processes, as well as the distinction of CO_2-derived alterations from the natural rock-prone variability are strongly hampered. The initial ion concentrations in the synthetic brine, which was prepared based on original Ketzin brine data available at the start of the experiments, were below those of pristine reservoir brine and an increase of fluid species was expected without any impact of CO_2. Experimentally determined K^+, Ca^{2+} and Mg^{2+} concentrations, however, clearly exceed pristine reservoir brine concentrations, which inevitably points on CO_2-related dissolution processes of K^+-, Ca^{2+}- and/or Mg^{2+}-bearing mineral phases, respectively.

The **siltstone** experiment illustrates only minor mineralogical-geochemical changes that are mainly associated with slightly increased TDS concentrations. Siltstone minerals show variable abundances and no uniform, clear trends with time. Grain surfaces of anhydrite, plagioclase and K-feldspar indicate intensifying alteration during CO_2-exposure. With time, K^+, Ca^{2+}, Sr^{2+}, Mn^{2+} and SO_4^{2-} brine concentrations increased in both CO_2- and N_2-filled autoclaves either suggesting similar chemical reactivity of the CO_2- and N_2-systems, or equilibration reactions predominantly caused by the synthetic brine without any influence of the pressure medium. On the opposite, Mg^{2+} brine concentrations in the CO_2-treated fluid samples are significantly higher compared to those in untreated and N_2-treated fluid samples clearly pointing on CO_2-related mineral-fluid processes. Increases of the distinct ions suggest different kinetic rates of the underlying dissolution processes. While K^+, Mg^{2+} and Sr^{2+} show fastest increases and reach approximately constant concentration levels within two months, Ca^{2+} brine concentration is constant after four months, SO_4^{2-} reveals slowest reactivity and highest brine concentrations after six months.

During **geochemical modeling** the initial equilibrium model proved the expected occurrence of CO_2-independent reactions due to the synthetic brine used in the sandstone experiments. Despite some

necessary simplifications and assumptions for model setup comprehensive equilibrium as well as kinetic simulations showed that the results of the geochemical models are in acceptable agreement with the experimental observations. Also the main processes obtained from the sandstone experiments were generally well reproduced. Main discrepancies are related to reactions involving both K- as well as Fe-bearing minerals and the answer to the apparent mismatch of measured and simulated dissolved K^+ and Fe^{2+} concentrations needs further attention. Most kinetic simulations did not reach equilibrium at the end of the simulations emphasizing that geochemical reactions did not come to an end. All in all, the presented geochemical modeling approach is not capable of covering the complete range of natural variability.

The results of the **siderite** experiments form one consistent data set. Rapid and steep initial increases in Ca^{2+}, Mg^{2+}, Fe^{2+} and Mn^{2+} brine concentrations are caused by kinetically rapid dissolution of fines that dissolve quicker due to the larger surface area. Despite the fact that no new formed phase was detected, subsequent decreases in cation concentrations point to the formation of (a) mineral phase(s) incorporating respective cations. While continuous dissolution of Ca^{2+} and Mg^{2+} components is indicated by increasing Ca^{2+} and Mg^{2+} brine ion concentrations to the end of the experiments, continuous precipitation of Fe^{2+}- and Mn^{2+}-bearing mineral(s) is implied by decreasing Fe^{2+} and Mn^{2+} ion concentrations. Surfaces of CO_2-treated ankerite grains indicate strong corrosion, whereas those of CO_2-treated siderite are largely unaffected. This is in line with increasing siderite and decreasing ankerite abundances with run duration, respectively.

The **illite** experiments reveal increased Ca^{2+} and Mg^{2+} brine concentrations and similar chemical behavior of the two ions with run duration. Dissolved Ca^{2+} levels are significantly higher than those of Mg^{2+} and together with decreasing Ca-smectite abundances indicate preferred dissolution of Ca-smectite out of the illite-smectite mixed-layer mineral. No secondary mineral precipitate was detected.

During **labradorite** experiments increased Ca^{2+} brine concentrations in line with corroded grain surfaces clearly suggest labradorite dissolution. Despite minor differences in Ca^{2+} behavior during the two labradorite experiments, Ca^{2+} brine concentrations are in the same order of magnitude and show identical processes, namely the dissolution of labradorite. The reason for the slight difference in Ca^{2+} brine evolution is unclear, but might be related to analytical artifacts; e.g. inaccuracies with regard to dilution. No secondary mineral precipitate was detected.

Plagioclase solid solution shows dissolution during both whole rock experiments and in the labradorite powder experiments. In all the three experimental approaches surfaces of plagioclase grains show corrosion and etching textures, which intensify with time of CO_2 exposure. Increased Ca^{2+} concentrations in the sampled brines in line with more abundant Na-rich plagioclase end-member compositions as determined from EMPA data obtained from sandstone samples taken after 15 months of CO_2 exposure suggest preferred dissolution of the anorthite component of plagioclase. Rietveld refined plagioclase abundances, however, do not show a distinct trend. Note that in Rietveld calculations albite was refined for plagioclase and therefore no differentiation of anorthite and albite is possible during XRD analysis. As the labradorite has an intermediate starting composition of $Ab_{0.5-0.6}$ and $An_{0.4-0.5}$ the monomineralic labradorite experiments are suited for particularly studying the dissolution behavior and stability of the different plagioclase components in a relatively simple CO_2-NaCl-H_2O system. While dissolved Ca^{2+} strongly increases during these experiments, Na^+ brine concentrations are constant within analytical error. Together with corrosion textures observed on

surfaces of CO_2-treated labradorite grains this suggests labradorite dissolution and preferred release of Ca^{2+} into solution. But due to the high, 2 M NaCl brine salinity and also because EMPA data from the solid material was not determined, the fate of (dissolved) Na^+ cannot be explicitly resolved here. Note that evaluation of ICP-MS fluid data is pending. Dissolution of the anorthite component and stabilization of the albite component of plagioclase was also observed during geochemical modeling of the sandstone experiment. In the kinetic simulations, dissolved Ca^{2+} increases and the anorthite abundance decreases, whereas the abundance of albite remains unchanged and also dissolved Na^+ slightly increased.

Similar corrosion textures on plagioclase grains as those described above next to albite end-member compositions associated with albitization of plagioclase and/or K-feldspars are typical diagenetic processes. But as plagioclase grains with fresh and unaltered surfaces were only found in untreated sandstone and siltstone samples, on the one hand, and corrosion textures intensify with run duration, on the other, alteration of plagioclase due to the presence of CO_2 is strongly indicated through both experiments. Also stable or even precipitating albite can be reasonably assumed for the CO_2-exposure experiments. Due to the fact that the experiments have been conducted using a highly saline and Na-rich brine it can also be speculated that Ca^{2+} replacement by Na^+ might also control the chemical behavior and dissolution kinetics of the plagioclase solid solution.

Similar to plagioclase solid solution, **K-feldspar** grains from CO_2-treated sandstone and siltstone samples partially show corroded surfaces that, next to substantially increased K^+ brine concentrations, suggest dissolution of K-feldspar. K-feldspar abundances, however, do not show a distinct trend with time and dissolution pits and etch textures were also found on few untreated K-feldspar grains. Despite the fact that no clear signs of altering mica were detected, this first data set shows decreased K^+ and Al^{3+} contents per formula unit of muscovite that may indicate illitization during the runs. As also the fate of **illite** is uncertain during the sandstone and siltstone experiments, and illite precipitation with constant or even decreasing K^+ brine concentrations are indicated during modeling, this qualitative contradiction between increased K^+ brine concentrations and corrosion textures on experimentally treated K-feldspar and supersaturation of K-feldspar (and illite) predicted from the models cannot be resolved here. The reaction of the illite separate with 2 M NaCl brine and CO_2 is characterized by increasing Ca^{2+} and Mg^{2+} brine concentrations. Note that the evaluation of ICP-MS fluid data is pending. While no significant changes in illite surface morphology were detected, the slightly increased illite abundance with run duration may be due to a relative enrichment of illite compared to the bulk caused by decreasing Ca-smectite and K-feldspar abundances (see above), respectively.

However, our results strongly indicate that dissolution of quantitatively relevant amounts of K-feldspar and illite is unlikely during respective experiments. Dissolving K-feldspar has been described in other reservoir sandstones from both natural CO_2 accumulations and batch as well as flow-through experiments. To date no explanation for the uniform decrease of dissolved K^+ concentrations, which suggest precipitation of a K-bearing mineral, in samples between 21 and 24 months is at hand. Apart from the fact that no new formed K-bearing mineral was detected, K^+ incorporation into clay minerals such as illite, which could potentially form as a result of feldspar weathering, can be speculated. Clay mineral colloid suspensions were observed in brine samples of both sandstone and siltstone experiments. These clogged the filters used for fluid cleaning during sampling and it is highly probable that these clays also contained K^+ amongst cations like Mg^{2+}, Al^{3+} and Si^{4+} (see below). Whereas decreasing K-feldspar (orthoclase) abundances were also detected during the illite

experiments, again the chemical behavior of K-feldspar cannot be (fully) evaluated because of missing K^+ brine data related to Na^+ peak overlapping during ICP-AES measurements with axial plasma. The same holds true for the siderite experiments, in which traces of K-feldspar were also detected, but only ICP-AES brine data is available.

Anhydrite surfaces of CO_2-treated samples show corrosion textures, which together with increased SO_4^{2-} brine concentrations clearly point to **anhydrite** dissolution during both sandstone and siltstone experiments. Anhydrite abundances as determined by XRD analysis do not show a consistent trend with run time. This is most likely related to the heterogeneous, poikilitic distribution of anhydrite cement. First signs of anhydrite alteration have been observed in samples taken after 21 and 24 months, respectively, in which dissolution textures occur along preferred crystallographic features. Subsequent samples display accentuated dissolution holes and fissures that are not restricted to crystallographic features. This in line with strongly increased SO_4^{2-} brine concentrations suggests intensified anhydrite dissolution with run duration. Note that anhydrite is the solitary sulfur/sulfate-source in sandstone, and the only quantitatively relevant sulfur/sulfate-source in siltstone samples. Because the initial synthetic brine is, amongst others, undersaturated with respect to SO_4^{2-}, anhydrite dissolution during the sandstone experiments is partially related to brine-rock equilibration. Based on subsequent data of the original formation brine composition at Ketzin (, which had not been available at the start of the experiments) an increase of fluid species occurred because the initial ion concentrations in the synthetic brine were below those of pristine reservoir brine reflecting the evolution of the synthetic brine to its potential equilibrium composition, even without any impact of CO_2. Therefore, the large increase especially of SO_4^{2-} brine concentrations during the sandstone experiment is to a large extent caused by CO_2-independent equilibration of the synthetic brine. Also geochemical modeling confirmed that during equilibration of the CO_2-free synthetic brine with the initial mineral assemblage chemical reactions were triggered and SO_4^{2-} brine concentrations increased due to anhydrite dissolution. The average dissolved SO_4^{2-} increase is about 1.3 times higher than that of the average dissolved Ca^{2+} increase and about 8.1e-4 mol/L Ca^{2+} must hence have precipitated in a solid, yet undetected phase again. Assuming that the SO_4^{2-} increase is exclusively caused by anhydrite dissolution between 0.45 and 0.64 g anhydrite dissolved within 24 months of CO_2 exposure.

Dissolved SO_4^{2-} concentrations are constant within analytical error during the first four months of the siltstone experiments, but strongly increase within the following two months. Considering anhydrite as the major source of SO_4^{2-} also in the siltstone samples, anhydrite dissolution starts after the fourth month. Note that despite minor increases in Sr^{2+} brine concentrations (see below), which could be caused by dissolving $(Ba,Sr)SO_4$ solid solution, no (other) data suggest alteration of respective minerals. The SO_4^{2-} increase in the sampled brine of the siltstone experiments is about 6.5 times higher than the Ca^{2+} increase. Hence, about 0.06 mol/L Ca^{2+} must have precipitated in a solid, yet undetected phase again. Assuming that all SO_4^{2-} derived from anhydrite dissolution, the SO_4^{2-} increase equals 0.57 g anhydrite dissolved from the siltstone. The N_2 blank shows a similar SO_4^{2-} brine concentration compared to that of the CO_2-treated sample taken after six months. As the N_2-blank sample contains significantly more anhydrite, the comparable SO_4^{2-} brine concentration suggests equilibrium concentrations. The increase in dissolved Sr^{2+} is distinct, but only minor. Similar Sr^{2+} brine concentration increases were also found in the experiments on sandstone, in which no $(Ba,Sr)SO_4$ solid solution was detected. These Sr^{2+} increases may also be caused by the dissolution of anhydrite, which can accommodate up to 1200 ppm Sr^{2+} as determined in the siltstone sample.

Decreasing **analcime** abundance indicates analcime dissolution during the sandstone experiments. While average Na^+ brine concentrations are constant within analytical error and also analcime surfaces do not show any clear sign of dissolution in both whole rock experiments, only Rietveld refined XRD data suggests potential dissolution of analcime. Dissolving analcime is also predicted through geochemical models, in which analcime is, however, only modeled as an equilibrium phase since no kinetic data are available. Based on our data from both sandstone and siltstone experiments the geochemical behavior of analcime during CO_2-exposure cannot be conclusively evaluated.

Results from the experiments as well as from modeling suggest **chlorite and/or biotite** dissolution. The trend of decreasing chlorite (+ biotite) abundances in XRD data from the sandstone samples is not strictly uniform and one sample even indicates slightly higher chlorite (+ biotite) abundances at the end of the experiment. Most changes in chlorite (+ biotite) abundances within the distinct core sections as determined by Rietveld refinements are within analytical error. While the CO_2-independent equilibrium model predicts complete dissolution of the initially present amount of chlorite (chamosite-7A), kinetic models indicate only negligible dissolution of chlorite (chamosite-7A). Note that chlorite (chamosite-7A) is not a primary mineral as determined by the set of comprehensive equilibrium models and hence does not contribute quantitatively to the fluid chemistry of the sandstone experiments. The observed increase of Mg^{2+} brine concentrations in both sandstone and siltstone experiments is probably due to incongruent, non-stoichiometric dissolution of 2:1 sheet silicates. Chloritization and/or dissolution of biotite may also explain increased K^+ brine concentrations during both experiments. However, neither lower K^+ contents nor lower total weight percentages oxides – as is typical for chloritization of biotite – have been unequivocally observed in both experiments.

Hematite dissolution is strongly suggested during the sandstone experiments as well as during modeling. Increased Fe^{2+} brine concentrations in the sandstone samples that have the highest initial hematite contents together with decreasing hematite abundances to the end of the experiments clearly point to hematite dissolution. The remainder sandstone samples are characterized by comparatively low concentrations of dissolved Fe^{2+} and constant hematite abundances within analytical error. While equilibrium models show hematite precipitation, the models including kinetic rate laws suggest strong undersaturation and thus indicate dissolution of hematite. Hence, the presented results both from the laboratory experiments as well as from geochemical modeling are equivocal with respect to the chemical behavior of hematite and need further considerations and investigations (see below).

Rietveld refined XRD data show constant **quartz** abundances and no clear trends with time for both whole rock experiments. Dissolution pits on quartz surfaces of some few siltstone samples treated for six months indicate quartz alteration, but it is not determinable whether these developed during the experiments or if they are remnants of diagenetic alteration. In either case this process would be negligible quantitatively. Quartz was generally considered inert during kinetic modeling. This consideration is confirmed by a kinetic model, in which chalcedony was incorporated as SiO_2 proxy based on similar SI values for both chalcedony and quartz, and the results of respective simulations show relatively large mismatches with experimental brine data. Accordingly, it is reasonable to argue that quartz is chemically inert during the sandstone and siltstone experiments.

The reactivity and chemical behavior of **carbonate minerals** is of outstanding importance during the geological storage of CO_2, because (i) carbonate minerals are commonly present in reservoir

formations, (ii) carbonate minerals are generally very reactive towards CO_2-enriched solutions and in acid environments, respectively, and (iii) carbonate minerals are the most immobile and hence most secure form of CO_2 sequestration.

Despite the fact that **dolomite** does neither display corrosion textures on grain surfaces nor changes in mineral abundance and although no new formed carbonate was detected, one may still speculate that minor amounts of carbonate/dolomite precipitated during the course of the sandstone experiments, e.g. as coatings around existing dolomite grains. But as carbonates generally form in alkaline environments, it is highly unlikely that any carbonate mineral precipitated during the here presented experiments. This is in line with results from geochemical simulations that predict acidic conditions ($4.4 \leq pH \leq 5.7$) next to undersaturation of carbonate minerals and clearly point on preferred carbonate dissolution.

Also during **siderite** experiments no new formed carbonate phase was detected. While **ankerite** shows corrosion textures on grain surfaces and decreasing mineral abundance, siderite reveals largely unaffected grain surfaces and increasing mineral abundance over time. Together with the evolution of inorganic brine data these findings are explainable through (i) kinetically rapid dissolution of $Ca^{2+}(/Mg^{2+})$-rich ankerite that changed into precipitation of $Fe^{2+}(/Mn^{2+})$-rich siderite after Ca^{2+} (super)saturation was reached in the brine, (ii) partial dissolution of Mg^{2+} out of siderite leaving the remainder ions unaffected, or (iii) Mg^{2+} substitution for Fe^{2+} and Mn^{2+} in siderite and/or ankerite. In any case, the data set obtained from the siderite experiments clearly shows higher solubility of ankerite over siderite under the applied experimental conditions and hence suggests that siderite is a stable mineral trapping phase during geological CO_2 storage.

The main focus during **geochemical modeling** of the sandstone experiments was on matching experimental observations. The modeling turned out to be highly complex so that several assumptions and simplifications had to be made. However, the rather simplified equilibrium models and those considering reaction kinetics show acceptable matches with experimentally determined ion concentrations and are capable of identifying the ongoing geochemical processes during the sandstone experiments. In order to improve the description of the complex experimental system a large number of equilibrium models were run. These models comprise all possible combinations of the verified sandstone minerals plus calcite and kaolinite as potential secondary phases, and the definition of a mathematical dispersion relation for statistical analysis and therefore rating of best matching equilibrium models with respective mineral combinations.

Systematic discrepancies with regard to qualitative differences between experiments and modeling occur for dissolved K^+, Fe^{2+} and Al^{3+} (and Si^{4+}). While dissolved Fe^{2+} is also quite variable in the sandstone experiments (see above), potential reasons for such discrepancies can be ascribed to possibly imprecise data for K- and Fe-bearing mineral phases and respective solubility products in the thermodynamic database, but also to the choice of the mineral phase taken as proxy for illite, e.g. In this context it is noteworthy that although hematite is strongly undersaturated in the kinetic simulations it does not show significant dissolution due to kinetic limitation; a fact that possibly also explains the discrepancy with respect to the equilibrium models, which consider the same mineral assemblage. This furthermore points towards a possible need of re-parameterization of the associated kinetic rate law. In addition to this, chloritization and/or dissolution of biotite as well as Na^+/K^+ ion exchange in clay minerals are processes not covered during modeling and may explain the mismatch for dissolved K^+. Iron species are redox sensitive, but as redox reactions are only partially

incorporated into the selected database, this circumstance also leads to incomplete results. Another source of uncertainty with regard to iron species is associated with iron (hydr)oxide coatings that could potentially be mobilized during CO_2-exposure experiments. These are generally rather difficult to incorporate into geochemical models also because of being inherently difficult to identify and quantify within bulk rock samples. The systematic mismatches of dissolved Al^{3+} (and Si^{4+}) concentrations from the experiments and modeling is most likely related to the fluid sampling during the experiments. In order to take fluid and rock samples the autoclave reactors were opened, i.e. cooled and depressurized. This quenching may cause spontaneous precipitation, which probably affects (K-, Fe-, Si-) Al-species to a larger extent than others. Note that precipitates blocked the filters used for fluid sampling. Unfortunately, the quenching cannot be simulated with PHREEQC, as the system pressure was included via the CO_2 fugacity. Based on our data we cannot conclusively explain the mismatch between measured and modeled K^+, Fe^{2+}, Al^{3+} and Si^{4+} concentrations.

In the simulations considering kinetic rate laws reactions roughly reached equilibrium for most input minerals (SI≈±2) and most models after 24 months of CO_2 exposure. Only the kinetic model that suppresses any mineral precipitation is still far from equilibrium at the end of the simulation period (SI>>0 for the albite component of plagioclase, analcime, illite, K-feldspar and kaolinite), and the anorthite component of plagioclase and hematite are generally strongly undersaturated (SI<<0) in the kinetic models. It is noteworthy that only one kinetic model predicts mineral carbonation in the form of 0.70 g dolomite precipitation. The consideration of inert quartz during kinetic modeling was confirmed by the model in which chalcedony was incorporated as SiO_2 proxy based on very similar SI values for both chalcedony and quartz. Results of this model show relatively large mismatches with experimental brine data.

The set of kinetic simulations show that the model generally best matching with experimental brine data is the one completely suppressing mineral precipitation. This result is in line with experimental data evaluation of solid material, in which no new formed mineral phase was detected.

8.3 Concluding remarks

It is general consensus that mineralogical-geochemical reaction paths – also or even obtained from laboratory experiments using whole rock samples – are highly site specific and results from different sites are not fully comparable. Therefore, universal and absolute extrapolations of the acquired results from the Stuttgart Formation at Ketzin to other storage formations and rock types are rather little or can only point towards general geochemical trends.

At least in the time scale of up to 40 months and with assuming that the here presented whole rock experiments are representative of the Ketzin reservoir the initially most important geochemical process on the larger field scale is dissolution of minor amounts of minerals. Hence, one can argue that injected CO_2 generally promotes geochemical alteration of siliciclastic rocks by enhancing mineral dissolution rates in respective reservoir formations through shifting the thermodynamic equilibrium from the one that existed prior to CO_2 injection. With analogous increases in porosity (and permeability) due to mineral dissolution this assures an adequate injectivity and only insignificant to moderate increases in reservoir and wellhead pressures as a consequence of CO_2 injection. A well controllable pressure development both within the storage system and the injection well together with a fundamental understanding of the geochemical processes governing the fate and migration of the injected CO_2 within the reservoir are necessary prerequisites for safe and secure operation of CO_2 storage sites. Still it is noteworthy that in the long term it is very likely that mineral dissolution processes will recede and precipitation processes will prevail instead. Then mineral carbonates, such as siderite, e.g., should form.

The modeling of the CO_2-exposure experiments using Stuttgart Formation sandstone and in situ P-T conditions of the Ketzin pilot site predicts that the anorthite component of plagioclase and cement phases dissolve, while clay minerals should tendentially precipitate. Despite simulating a closed system in which respective models predict that thermodynamic equilibrium is not reached after 24 months, for the field scale and respective dynamic conditions this means that equilibration following CO_2 injection is a long-term process potentially taking thousands of years or more. Consequently, geochemical reactions are not only highly site-specific (see above), but also time-dependent, so that reactive transport simulations have to be applied as standard procedures to study how these reactions evolve over time. In general, these long-term simulations suggest that carbonate cements initially dissolve to potentially increase the porosity (and permeability), and that subsequent reactions are dominated by the dissolution of feldspar minerals and the precipitation of carbonate minerals and clays, thus potentially decreasing porosity (and permeability). But as long as the validation of such long-term models is not possible – and it is noteworthy at this point that also natural CO_2 analogues are difficult to interpret uniquely due to an often complex suite of reaction paths and changed boundary conditions – a numerical model can at best give reliable prognoses. This holds also true for the geochemical simulations of the Ketzin reservoir sandstone experiments and respective extrapolations to other storage sites.

The main overall result of this dissertation is that the mineralogical-geochemical effects of injected CO_2 on siliciclastic reservoirs are minor, and that the (chemical) integrity of the Ketzin storage system is not significantly affected by CO_2. Within a reasonable range and likelihood it is highly probable that these latter statements are transferable to comparable siliciclastic reservoir systems.

8.4 Outlook

Future work to continue the presented work should include more detailed and comprehensive kinetic modeling approaches. First of all the time scale of the kinetic simulations should be extended until equilibrium is reached to determine the final mineral assemblage. This would also shed light on the potential of mineral carbonation during the experiments and therefore within the Ketzin reservoir. Kinetic models could also be rerun with updated and more precise fluid data of the pristine Ketzin reservoir as available today, as well as with iteratively determined and pre-calculated synthetic brine composition that is in equilibrium with the mineral assemblage at the start of the experiments in order to exclude brine-rock equilibration reactions and therefore assuring the analysis of the effect of added CO_2 only. Furthermore, numerical investigations should be intensified in terms of comparing different databases, a thorough sensitivity and uncertainty analysis especially with regard to the reactive surface area of individual minerals. Also other approaches, such as more detailed and complex inverse modeling combined with calibration of kinetic parameters should be investigated.

For obtaining thermodynamic and kinetic baseline data generally applicable for the geological storage of CO_2 laboratory experiments using whole rock samples are not suited; at least when as complex lithologies as the Stuttgart Formation are investigated. For these purposes monomineralic experiments using well characterized separates of rock-forming minerals ordinarily occurring in (potential) CO_2 storage reservoirs are more adequate, e.g., in obtaining kinetic rates and rate parameters. In order to determine reliable and comprehensive data, respective experimental studies should cover broad P-T ranges, different brine salinities as well as brine compositions. Nonetheless, such monomineralic studies would have the apparent disadvantage of not covering complexly coupled geochemical processes typically occurring in reservoir systems.

References

AGEB, 2011. Jahresbericht 2011 der Arbeitsgemeinschaft Energiebilanzen e.V., Berlin and Cologne, Germany, 5 pp.

Angus, S., B. Armstrong and K.M. de Reuck, 1973: International Thermodynamic Tables of the Fluid State Volume 3. Carbon Dioxide. IUPAC Division of Physical Chemistry, Pergamon Press, London, pp. 266–359.

Bachu, S., Gunter, W.D., Perkins, E.H., 1994. Aquifer disposal of CO_2: hydrodynamic and mineral trapping, Energy Conversion and Management, 35(4), 269–279.

BGR, 2009. Energierohstoffe 2009 – Reserven, Ressourcen, Verfügbarkeit. Published by Federal Institute for Geosciences and Natural Resources (BGR), Hannover, Germany, 288 pp.

Celia, M.A., Bachu, S., Nordbotten, J.M., Gasda, S.E., Dahle, H.K., 2005. Quantitative estimation of CO_2 leakage from geological storage: Analytical models, numerical models and data needs. Proceedings of 7th International Conference on Greenhouse Gas Control Technologies (GHGT-7), 663–672.

Czernichowski-Lauriol, I., Sanjuan, B., Rochelle, C., Bateman, K., Pearce, J., Blackwell, P., 1996. Analysis of the geochemical aspects of the underground disposal of CO_2: scientific and engineering aspects. In: Deep Injection Disposal of Hazardous and Industrial Waste, J.A. Apps and C.F. Tsang (Eds), Academic Press, 565–583.

Czernichowski-Lauriol, I., Rochelle, C.A., Gaus, I., Azaroual, M., Pearce, J., Durst, P., 2006. Geochemical interactions between CO_2, pore-waters and reservoir rocks: lessons learned from laboratory experiments, field studies and computer simulations. In: Advances in the Geological Storage of Carbon Dioxide. NATO Science Series IV, 157–174.

De Lucia, M., Bauer, S., Beyer, C. Kühn, M., Nowak, T., Pudlo, D., Reitenbach, V., Stadler, S., 2012. Modelling CO_2-induced fluid-rock interactions in the Altensalzwedel gas reservoir. Part I: from experimental data to a reference geochemical model. Environmental Earth Sciences 67 (2), 563–572.

Fagerlund, F., Niemi, A., Bensabat, J., Shtivelman, V., 2013. Design of a two-well field test to determine in situ residual and dissolution trapping of CO_2 applied to the Heletz CO_2 injection site. International Journal of Greenhouse Gas Control, in press.

Fischer, S., Liebscher, A., Wandrey, M., 2010. CO_2-brine-rock interaction – First results of long-term exposure experiments at in situ P-T conditions of the Ketzin CO_2 reservoir. Chemie der Erde 70 (3), 155–164.

Fischer, S., Zemke, K., Liebscher, A., Wandrey, M., 2011. Petrophysical and petrochemical effects of long-term CO_2-exposure experiments on brine-saturated reservoir sandstone. Energy Procedia 4, 4487–4494.

Fischer, S., De Lucia, M., Liebscher, A. Kinetic modeling of laboratory CO_2-exposure experiments performed on whole rock reservoir samples. Submitted (A) to the proceedings of LE STUDIUM conference "Geochemical reactivity in CO_2 geological storage sites", Orléans, France.

Fischer, S., Liebscher, A., De Lucia, M., Hecht, L., 2013a. Reactivity of sandstone and siltstone samples from the Ketzin pilot CO_2 storage site – Laboratory experiments and reactive geochemical modeling. Accepted in Environmental Earth Sciences, Springer.

Fischer, S., Liebscher, A., Zemke, K., De Lucia, M. Does injected CO_2 affect (chemical) reservoir system integrity? – A comprehensive experimental approach. Submitted (B) to the proceedings of GHGT-11 conference, Kyoto, Japan, Energy Procedia, Elsevier.

Fischer, S., Liebscher, A., 2013b. Mineral solubilities in CO_2-saturated NaCl brine systems. Procedia Earth and Planetary Science, 7, 260–263.

Gaus, I., Azaroual, M., Czernichowski-Lauriol, I., 2005. Reactive transport modeling of the impact of CO_2 injection on the clayey cap rock at Sleipner (North Sea). Chemical Geology, 217, 319–337.

Gaus, I., 2010. Role and impact of CO_2-rock interactions during CO_2 storage in sedimentary rocks. International Journal of Greenhouse Gas Control, 4, 73–89.

Gunter, W.D., Perkins, E.H., McCann, T.J., 1993. Aquifer disposal of CO_2-rich gases: reaction design for added capacity. Energy Conversion and Management, 34, 941–948.

Gunter, W.D., Wiwchar, B., Perkins, E.H., 1997. Aquifer disposal of CO_2-rich greenhouse gases: Extension of the time scale of experiment for CO_2-sequestering reactions by geochemical modeling. Mineralogy and Petrology, 59, 121–140.

IEA, 2011: World Energy Outlook. International Energy Agency, Paris, France.

IEA, 2012a: World Energy Outlook. International Energy Agency, Paris, France.

IEA, 2012b: Key World Energy Statistics. International Energy Agency, Paris, France.

IEA, 2012c: CO_2 Emissions from Fuel Combustion. International Energy Agency, Paris, France.

IPCC, 2001a: Climate Change 2001 – Mitigation. A Report of Working Group III of the Intergovernmental Panel on Climate Change. B. Metz, O. Davidson, R. Swart, and J. Pan (eds.). The Third Assessment Report of the Intergovernmental Panel on Climate Change. Cambridge University Press, Cambridge, United Kingdom and New York, NY, USA, 753 pp.

IPCC, 2001b: Climate Change 2001 – The Scientific Basis. Contribution of Working Group I. J.T. Houghton,Y. Ding, D.J. Griggs, M. Noguer, P.J. van der Linden, X. Dai, K. Maskell, and C.A. Johnson (eds.).The Third Assessment Report of the Intergovernmental Panel on Climate Change. Cambridge University Press, Cambridge, United Kingdom and New York, NY, USA, 881 pp.

IPCC, 2005: IPCC Special Report on Carbon Dioxide Capture and Storage. Prepared by Working Group III of the Intergovernmental Panel on Climate Change. B. Metz, O. Davidson, H. de Coninck, M. Loos and L. Meyer (eds.). Cambridge University Press, Cambridge, United Kingdom and New York, NY, USA, 442 pp.

IPCC, 2007: Climate Change 2007 – The Physical Science Basis. Contribution of Working Group I to the Fourth Assessment Report of the Intergovernmental Panel on Climate Change. S. Solomon, D. Qin, M. Manning, M. Marquis, K. Averyt, M.M.B. Tignor, H. LeRoy Miller, Z. Chen (eds.). Cambridge University Press, Cambridge, United Kingdom and New York, NY, USA, 996 pp.

Karl, T.R., Trenberth, K.E., 2003. Modern Global Climate Change, Science, 302, 1719–1723.

Kaszuba, J.P., Janecky, D.R., Snow, M.G., 2005. Experimental evaluation of mixed fluid reactions between supercritical carbon dioxide and NaCl brine: Relevance to the integrity of a geologic carbon repository. Chemical Geology 217 (3–4), 277–293.

Kaya, Y., 1995. The role of CO_2 removal and disposal. Energy Conversion and Management, 36 (6–9), 375–380.

Kharaka, Y.K., Thordsen, J.J., Kakouros, E., Ambats, G., Herkelrath, W.N., Beers, S.R., Birkholzer, J.T., Apps, J.A., Spycher, N.F., Zheng, L., Trautz, R.C., Rauch, H.W., Gullickson, K.S., 2010. Changes in the chemistry of shallow groundwater related to the 2008 injection of CO_2 at the ZERT field site, Bozeman, Montana. Environ. Earth Sci. 60 (2), 273–284.

Kiehl, J.T., Trenberth, K.E., 1997. Earth's Annual Global Mean Energy Budget. Bull. Am. Meteorol. Soc. 78, 197–208.

Kumar, A., Noh, M.H., Sepehrnoori, K., Pope, G.A., Bryant, S.L., Lake, L.W., 2005. Simulating CO_2 storage in deep saline aquifers, Carbon Dioxide Capture for Storage in Deep Geologic Formations - Results from the CO_2 Capture Project, v.2: Geologic Storage of Carbon Dioxide with Monitoring and Verification, S.M. Benson, (ed.), Elsevier, London, 977–998.

Lindeberg, E., Wessel-Berg, D., 1997. Vertical convection in an aquifer column under a gas cap of CO_2. Energy Conversion and Management, 38(Suppl.), 229–234.

Marchetti, C., and Nakicenovic, N., 1979. The Dynamics of Energy Systems and the Logistic Substitution Model. RR-79-13. Laxenburg, Austria: International Institute for Applied Systems Analysis (IIASA).

Martens, S., Kempka, T., Liebscher, A., Lüth, S., Möller, F., Myrttinen, B., Norden, B., Schmidt-Hattenberger, C., Zimmer, M., Kühn, M., 2012. Europe's longest-operating on-shore CO_2 storage site at Ketzin, Germany: a progress report after three years of injection. Environmental Earth Sciences 67 (2), 323–334.

Martens, S., Liebscher, A., Möller, F., Henninges, J., Kempka, T., Lüth, S., Norden, B., Prevedel, B., Szizybalski, A., Zimmer, M., Kühn, M., 2013. CO_2 storage at the Ketzin pilot site, Germany: Fourth year of injection, monitoring, modelling and verification. Energy Procedia, in press.

Nordbotten, J.M., Celia, M.A., Bachu, S., 2005. Injection and storage of CO_2 in deep saline aquifers: Analytical solution for CO_2 plume evolution during injection. Transport in Porous Media, 58, 339–360.

Obdam, A., van der Meer, L.G.H., May, F., Kervevan, C., Bech, N., Wildenborg, A., 2003. Effective CO_2 storage capacity in aquifers, gas fields, oil fields and coal fields. Proceedings of the 6th International Conference on Greenhouse Gas Control Technologies (GHGT-6), J. Gale and Y. Kaya (eds.), 1–4 October 2002, Kyoto, Japan, Pergamon, v.I, 339–344.

Parkhurst, D.L., Appelo, C.A.J., 1999. User's guide to PHREEQC (version 2)-A computer 737 program for speciation, batch-reaction, one-dimensional transport, and inverse geochemical 738 calculations. U.S. Geological Survey Water-Resources Investigations Report 99–4259.

Parry, W.T., Forster, C.B., Evans, J.P., Beitler, B., Chan, M.A., 2007. Geochemistry of CO_2 sequestration in the Jurassic Navajo Sandstone, Colorado Plateau, Utah. Environmental Geosciences, 14, 91–109.

Pearce, J.M., Holloway, S., Wacker, H., Nelis, M.K., Rochelle, C., Bateman, K., 1996. Natural occurrences as analogues for the geological disposal of carbon dioxide. Energy Conversion and Management, 37(6–8), 1123–1128.

Rochelle, C.A., Czernichowski-Lauriol, I., Milodowski, A.E., 2004. The impact of chemical reactions on CO_2 storage in geological formations: a brief review. In: Geological Storage of Carbon Dioxide, S.J. Baines and R.H. Worden (eds.), Special Publication of the Geological Society of London No. 233, 87–106.

Streit, J., Siggins, A., Evans, B., 2005. Predicting and monitoring geomechanical effects of CO_2 injection, Carbon Dioxide Capture for Storage in Deep Geologic Formations – Results from the CO_2 Capture Project, v. 2: Geologic Storage of Carbon Dioxide with Monitoring and Verification, S.M. Benson (ed.), Elsevier Science, London, 751–766.

United Nations, 2011. World Population Prospects: The 2010 Revision - Highlights and Advance Tables. Working Paper No. ESA/P/WP.220. United Nations, New York, NY, USA.

Watson, M.N., Boreham C.J., Tingate, P.R., 2004. Carbon dioxide, and carbonate elements in the Otway Basin: implications for geological storage of carbon dioxide. The APPEA Journal, 44 (1), 703–720.

Acknowledgements

This dissertation would not exist without Dr. habil. Axel Liebscher. Not only have you had the foresight for the need of mineralogical-geochemical investigations in the context of the geological storage of CO_2 in general and at the Ketzin pilot site with the conceptual ideas of laboratory experiments and methods to be applied to analyze them, but most importantly you were the one to inspire me, to promote me and – last but not least – to discuss the data and problems with me in uncountable meetings. It is finally your support and supervision that made my work entirely enjoyable.

I thank Prof. Dr. Gerhard Franz for supporting my work through discussions and supervision, and also for accepting to be first reviewer. I highly acknowledge the pleasant atmosphere at the TU Berlin.

I highly acknowledge the GeoEn and CO_2MAN projects for granting financial support for this dissertation.

Big thanks go to my colleagues Dr. Marco De Lucia, Dr. Bernd Wiese, Rudi Naumann (all GFZ Potsdam), Dr. Maja Tesmer (formerly at GFZ Potsdam and currently at BGR Hannover) and Dr. Christian Ostertag-Henning (BGR Hannover). It was and still is a pleasure for me to work with you. I have been very inspired by your work and knowledge as well as by valuable discussions and meetings.

Despite the fact that a complete list cannot be given here, I want to thank the many colleagues from the GFZ Potsdam for their collaboration and input to my work, especially Kornelia Zemke, Maren Wandrey, Sabine Tonn, Andrea Gottsche, Heiko Baschek, Gabi Arnold, Ilona Schäpan, Oona Appelt, Reiner Schulz, Hans-Peter Nabein.

Very particular mention is preserved for my wife Kristina. Your love inspires me every day and gives me the support to approach and manage all the difficulties in life. And I am more than deeply grateful to you for making me the present of our little Anton! I am so proud of you two!

My family and friends are deeply thanked for always being there for me and supporting me. You give me the power to manage everyday life and work and to be who I am.